THEORETICAL INVESTIGATION AND DESIGN FOR X-RAY LASERS
AND THEIR LITHOGRAPHIC APPLICATION

A THESIS SUBMITTED TO
THE GRADUATE SCHOOL OF NATURAL AND APPLIED SCIENCES
OF
MIDDLE EAST TECHNICAL UNIVERSITY

BY

PINAR DEMİR

IN PARTIAL FULFILLMENT OF THE REQUIREMENTS
FOR
THE DEGREE OF DOCTOR OF PHILOSOPHY
IN
PHYSICS

JUNE 2008

Aproval of the thesis:

THEORETICAL INVESTIGATION AND DESIGN FOR X-RAY LASERS AND THEIR LITHOGRAPHIC APPLICATION

Submitted by **PINAR DEMİR** in partial fulfillment of the requirements for the degree of **Doctor of Philosophy in Physics Department, Middle East Technical University** by,

Prof. Dr.   _____
Dean, **Graduate School of Applied Sciences**

Prof. Dr. Sinan K. Bilikmen   _____
Head of Department, **Physics**

Prof. Dr. Sinan K. Bilikmen   _____
Supervisor, **Physics Department, METU**

Assist. Prof. Dr. Elif Kaçar   _____
Co-Supervisor, **Physics Department, Kocaeli University**

Examining Committee Members:

Prof. Dr. Arif Demir, Head of Jury   _____
Physics Department, Kocaeli University

Prof. Dr. Sinan K. Bilikmen, Supervisor   _____
Supervisor, Physics Department, METU

Assoc. Prof. Dr. Serhat Çakır   _____
Physics Department, METU

Assist. Prof. Dr. Şerafettin Yaltkaya   _____
Physics Department, Akdeniz University

Assist. Prof. Dr. Hilal Göktaş   _____
Physics Department, Çanakkale 18 Mart University

                                                                04.07.2008
                    Date: _____

I hereby declare that all information in this document has been obtained and presented in accordance with academic rules and ethical conduct. I also declare that, as required by these rules and conduct, I have fully cited and referenced all material and results that are not original to this work.

Name, Last Name:

Signature:

ABSTRACT

THEORETICAL INVESTIGATION AND DESIGN FOR X-RAY LASERS AND THEIR LITHOGRAPHIC APPLICATION

Demir, Pınar

Ph.D., Department of Physics

Supervisor: Prof. Dr. Sinan K. Bilikmen

Co-Supervisor: Dr. Elif Kaçar

June 2008, 116 pages

Grazing incidence pumping (GRIP) is a scheme to produce x-ray lasers and extreme ultraviolet lithography is a means of lithographic production which requires soft x-rays with a bandwidth of 2% centred at 13,5 nm. In this work firstly a grazing incidence pumping of Ni-like Mo and Ne-like Ti x-ray laser media were simulated by using EHYBRID and a post-processor code coupled to it. The required atomic data were obtained from the Cowan code. Besides, the timing issue needed for amplification purpose in a Ti:Sapphire laser system has been described theoretically. Afterwards, in order to produce soft x-ray lasers for extreme ultraviolet lithographic applications, emission of soft x-rays in the 2% bandwidth centred at 13.5 nm emitted from Sn XII and Sn XIII ions were simulated by using the EHYBRID code for a laser operating at 1064 nm with 1 J of pulse energy and 6 ns of pulse duration. The intensity range that has been investigated is between $1\text{-}5 \times 10^{12}$ W/cm^2. Ion fractions of tin ions and line intensities corresponding to different electron temperatures were calculated by using the collisional radiative code NeF.

Keywords: X-ray Lasers, Grazing Incidence Pumping, Extreme Ultraviolet Lithography

ÖZ

X-IŞINI LAZERLERİ VE TAŞ BASKI UYGULAMASININ KURAMSAL İNCELENMESİ VE TASARIMI

Demir, Pınar

Doktora, Fizik Bölümü

Tez Yöneticisi: Prof. Dr. Sinan K. Bilikmen

Ortak Tez Yöneticisi: Dr. Elif Kaçar

Haziran 2008, 116 sayfa

Geliş açılı pompalama (grazing incidence pumping), x-ışını lazeri üretmek için kullanılan yöntemlerden birisidir ve uç morötesi taş baskı (extreme ultraviolet lithography) ise, 13,5 nm merkezli ve %2 bant aralıklı yumuşak x-ışını kullanarak taş baskı yapılan bir yöntemdir. Bu çalışmada Ti:Safir lazeri tarafından oluşturulan nikel benzeri molibdenyum ve neon benzeri titanyum x-ışını ortamları, EHYBRID ve bundan elde edilen verileri kulanarak işlem yapan bir kodun çalıştırılması ile modellenmiştir. Gereken atomik veriler Cowan kodu çalıştırılarak elde edilmiştir. Bunun yanı sıra Ti:Safir lazer sisteminin yükseltilmesi için gerekli zamanlama mekanizması kuramsal olarak türetilmiştir. Sonrasında, Uç morötesi taş baskı için gereken yumuşak x-ışını üretmek için, Sn XII ve Sn XIII iyonlarının 13,5 nm merkezindeki %2'lik bant aralığında kalan ışınımı EHYBRID kullanarak, 1064 nm dalga boyunda, 1 J enerjili ve 6 ns atım süreli bir lazer için modellenmiştir. Modellemede kullanılan şiddet aralığı 1-5 x 10^{12} W/cm^2 dir. Farklı elektron sıcaklıkları için iyon oranları ile çizgi şiddetleri çarpışmalı ışımalı kod olan NeF kodu ile hesaplanmıştır.

Anahtar Kelimeler: Geliş Açılı Pompalama, Uç Morötesi Taş Baskı

Anneanneme

ACKNOWLEDGMENTS

TABLE OF CONTENTS

ix

LIST OF TABLES

LIST OF FIGURES

xvi

CHAPTER 1

INTRODUCTION

The term x-ray is used for radiation below 1 nm with energies higher than 1 keV. However due to the historical reasons, a somewhat different spectrum has been defined for soft x-rays. In order to create such a low wavelength laser, the active medium must have a vey high temperature to produce population inversion in the upper laser level. When an active medium is in such a high temperature, it also means that it is in plasma state [1]. The emission wavelength of such a plasma depends on the material that the plasma has been formed from. Part of the electromagnetic spectrum can be seen in Fig. 1.1.
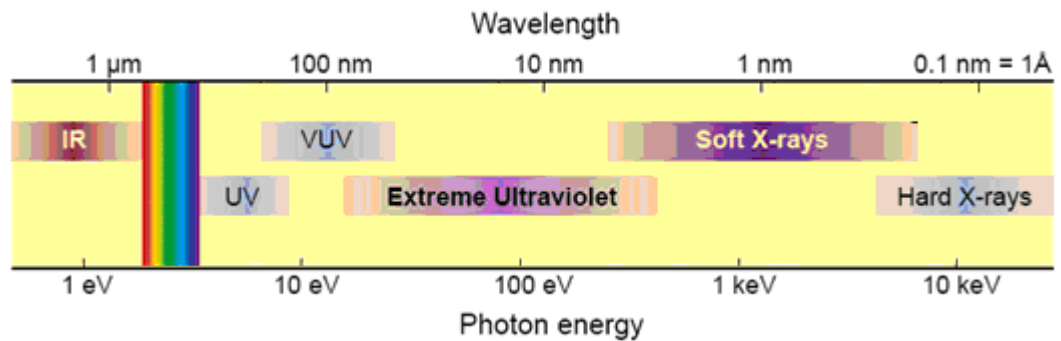
Fig. 1.1 NIR-hard x-ray part of the spectrum [2]. IR designates infrared, UV designates ultraviolet and VUV designates vacuum ultraviolet.

The thesis in concern is about the EHYBRID simulation results of the grazing incidence pumped neon-like titanium and nickel-like molybdenum soft x-ray emissions and the extreme ultraviolet emission of the tin plasma that is used for extreme ultraviolet lithographic application. The layout is as follows: Chapter 2 makes an introduction on the physics of x-ray lasers, chapter 3 is about the grazing incidence pumping scheme and the simulation results for neon-like titanium and nickel-like molybdenum, chapter 4 is about tin x-ray laser simulation results for extreme ultraviolet lithographic application and chapter 5 is the conclusion.

In chapter 2, firstly the radiative concepts for a plasma that is in thermodynamic equilibrium is described. Namely, the blackbody radiation, spectral intensity, spectral radiant energy flux and Kirchoff's law are described. Then, the bound-bound, bound-free and free-free electronic transitions that are responsible for the absorption and emission processes inside a plasma are described. The processes described are; spontaneous and stimulated emission, stimulated absorption, collisional excitation and de-excitation, radiative recombination, photoionization, collisional ionization, three-body recombination, bremsstrahlung and inverse bremsstrahlung. Afterwards line broadening mechanisms which are natural, Doppler, pressure and Stark broadenings and the concept of self-absorption or opacity are described. Finally the plasma models of x-ray lasers and the 1 D hydrodynamic code EHYBRID are described. The plasma models for an x-ray laser are local thermodynamic equilibrium, collisional radiative model and coronal equilibrium model. These models are described for a plasma of thin opacity.

Chapter 3 is about the grazing incidence pumping scheme of x-ray lasers. In this chapter firstly different x-ray laser schemes which differ in the way of producing population inversion are described. The pumping schemes described are the recombination x-ray lasers, electron collisional excitation x-ray lasers and the transient collisional x-ray lasers as a subgroup, optical field ionization, inner shell photoionization and resonant photoabsorption. Then the gain concept and the refraction inside the plasma are described. After giving a description of the pumping schemes of prepulse and grazing incidence pumping schemes, the neon-like titanium and nickel-like molybdenum x-ray lasers are given. From here, the simulation results of grazing incidence pumped neon-like titanium and nickel-like molybdenum by using the EHYBRID code are given.

As for chapter 4, it starts with an introduction on the optical lithographic systems and the optical lithographic systems that have been used in time for volume production. Then, an introduction to the extreme ultraviolet lithography is given after which the special optics that are being used and the calculation of the conversion efficiency in an extreme ultraviolet lithographic system is given. There exist two major problems in an extreme ultraviolet lithographic system, i.e. debris mitigation and increasing the conversion efficiency in order to provide the x-ray laser energy needed for volume production. Therefore firstly ways to limit the debris mitigation problem are described which are, the inclusion of an ambient gas, application of a magnetic field and repeller field configuration. Different target states that have been used in time in order to increase the conversion efficiency and decrease the amount of debris mitigation are given. Afterwards different types of materials that have been used are given so that their pros and cons are investigated in terms of their conversion efficiency and debris mitigation. Since tin emits in unresolved transition arrays, this concept is described prior to the simulation results. Finally, the EHYBRID simulation results of the tin ions that emit in the range in concern are given.

Finally in chapter 5, the simulation results of grazing incidence pumped neon-like titanium and nickel-like molybdenum given in chapter 3 and the simulation results of the tin x-ray laser for extreme ultraviolet lithographic application are analysed.

CHAPTER 2

CONCEPTUAL INTRODUCTION TO X-RAY LASER PHYSICS

2.1 Introduction

When high powered lasers irradiate a target with high intensities, bright x-rays are generated due to the radiative transitions inside the plasma. The first x-ray laser was put into practice in LLNL Novette laser facility in 1984 by irradiating a Se target with a kilo joule laser [3]. The transition that yielded the x-ray laser was among the neon-like selenium ions and the output laser wavelength observed was around 20 nm. Since then, x-ray lasers were produced by using transitions between many ions including neon-like titanium, nickel-like molybdenum, nickel-like tin and palladium-like xenon. As for the usage of x-ray lasers, indirectly driven inertial confinement fusion, lithography and microscopy can be named. Besides these, elementary research on the subject in concern with the aim of increasing the gain, efficiency, repetition rate and decreasing the output wavelength towards the water window region (2.3-4.4 nm) are still a research subject throughout the world.

The plasma that is produced for the generation of x-ray lasers is produced in a vacuum environment, the reasons of which will be made clear later on. The created plasma has a high density and high temperature. This also means that the plasma created has a pressure much higher than that of the vacuum environment that the plasma is formed in. Thus because of this difference in pressures, the plasma begins to expand through the vacuum [4]. During the time of laser pulse irradiation, the plasma expansion is an isothermal process. But after the irradiation has ceased, so does the energy deposition and thermal energy is converted into kinetic energy which is the case seen in adiabatic expansion. The electron temperature and density drops down rapidly with time. The plasma density and temperature in places nearer to the target surface drops down much faster in time than the parts that are further

from the target surface. In the parts that are further from the target surface, the temperature firstly increases with time and then drops down due to plasma expansion [5]. Electron density versus distance and electron temperature versus distance graph of a laser produced plasma can be seen in Figure 2.1. As can be seen from the graph, ablation region is a region of high density and low temperature. The interface between the ablation region and the coronal region is determined by the critical density surface. Soft x-rays are emitted from this critical density surface. Due to high thermal conductivity in the laser produced plasmas, electron temperature is almost constant in the region where the electron density is below the critical density. In the region where the electron density is above the critical density, the energy is transferred to the target via conduction and so temperature drops down to the value of the boiling point of the solid target at the ablation surface. Electron velocity on the other hand increases almost linearly as one goes from the critical density surface to lesser density regions [1].
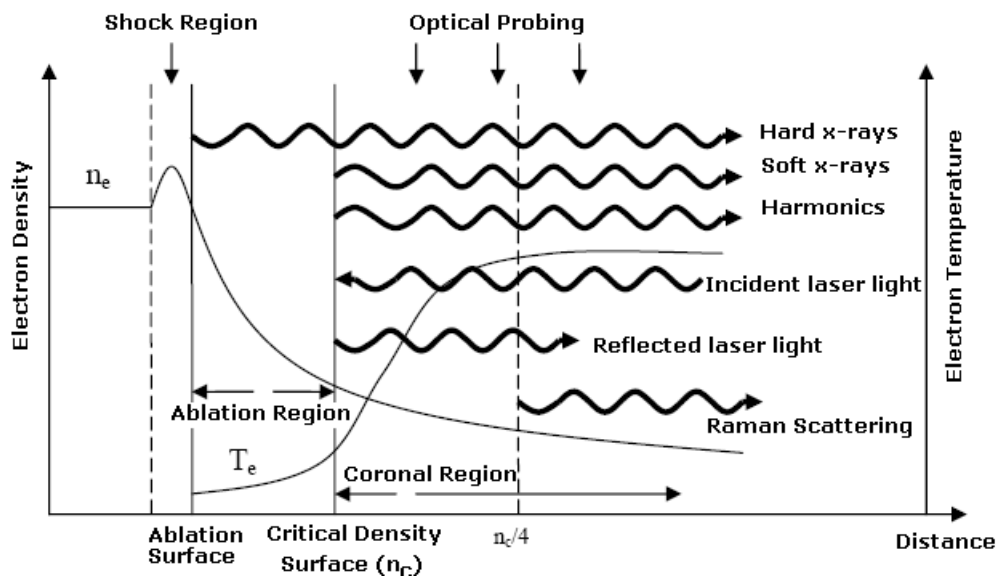
Figure 2.1 Electron density versus distance and electron temperature versus distance graph of a laser produced plasma.

5

The characteristics of a laser produced plasma (LPP) depend on the properties of the irradiating laser which are intensity, pulse duration, wavelength and the target properties which are geometry and the material and finally the vacuum environment i.e. whether the plasma is produced in a medium which includes an ambient gas or not. But since the plasma expands through the vacuum, the plasma parameters change from location to location [5].

There are various processes that determine the radiation intensity from a plasma [6]. The electrons are distributed among various energy levels and this distribution is determined by the collisions and radiative processes inside the plasma. Thus if we are concerned with a certain type of radiation, there is a probability of an electron to be in the upper state of the transition in concern. There exists three plasma models which describe this phenomenon; Local Thermal Equilibrium (LTE), Collisional Radiative Model (CR) and Coronal Equilibrium Model (CE). Each of them solves this distribution and the probability of the electron to be in the upper state in concern for a plasma with a different state than the others. Another thing that affects the radiation intensity from a plasma is the probabilities of atomic transitions. These are calculated by using atomic quantum theory. Finally, all the photons that are created from atomic transitions cannot escape from the plasma without being reabsorbed. This is the effect of opacity of the plasma to the radiation. The following sections will give details about some of these processes.

2.2 Radiation Concepts for a System in Thermal Equilibrium

If an infinite medium is in thermodynamic equilibrium and is in steady state, then the radiation field will also be in equilibrium. This thermal radiative equilibrium means that the number of photons emitted by the medium per unit time per unit volume in a given frequency interval $d\upsilon$ in a given solid angle $d\Omega$ is equal to the number of absorbed photons per unit time per unit volume in $d\upsilon$ and $d\Omega$. This radiation field that is in equilibrium is isotropic and is independent of the properties of the medium, i.e. it only depends on the temperature and the frequency. The spectral energy density which is the amount of energy radiated per unit volume with a frequency υ is equal to [7];

$$U_\upsilon = \frac{8\pi h\upsilon^3}{c^3} \frac{1}{\exp(h\upsilon/kT)-1}$$
(2.1)

where k is Boltzmann constant, h is Planck constant, c is speed of light and T is temperature. This equation is the blackbody radiation expression and is called the *Planck Function*. When plotted the peak of the Planck curve occurs at the photon energy;

$$h\upsilon = 2{,}82\,kT\,.\tag{2.2}$$

For $h\upsilon \ll kT$ i.e. at long wavelengths the Planck function reduces to the Rayleigh-Jeans law;

$$U_\upsilon = \frac{8\pi kT}{c^3}\upsilon^2\tag{2.3}$$

and for $h\upsilon \gg kT$ i.e. at short wavelengths, it reduces to the Wien's displacement law;

$$U_\upsilon = \frac{8\pi h\upsilon^3}{c^3}\exp(-h\upsilon/kT)\,.\tag{2.4}$$

The spectral intensity for radiative equilibrium is;

$$I_\upsilon = \frac{c}{4\pi}U_\upsilon = \frac{2h\upsilon^3}{c^2}\frac{1}{\exp(h\upsilon/kT)-1}\,.\tag{2.5}$$

If the spectral energy density is integrated over all frequencies, the result is;

$$U = \int_0^\infty U_\upsilon d\upsilon = \frac{4\sigma T^4}{c}\tag{2.6}$$

where σ is the Stefan-Boltzmann constant. It is worth to note that these relations are valid for a blackbody radiation in vacuum. If there exists a gas with refractive index n inside the cavity, the relations are modified as [8];

$$I_\upsilon = n^2\frac{2h\upsilon^3}{c^2}\frac{1}{\exp(h\upsilon/kT)-1}\tag{2.7}$$

and;

$$U_\upsilon = n^3\frac{8\pi h\upsilon^3}{c^3}\frac{1}{\exp(h\upsilon/kT)-1}\,.\tag{2.8}$$

But since usually $|n-1| \ll 1$ is the case, there is no such big difference in the addition of an ambient gas into the cavity.

Consider a unit area with the normal unit vector $\hat{n}$ as seen in Figure 2.2 [7] and that a light of intensity of I_υ with a frequency υ is incident on it.
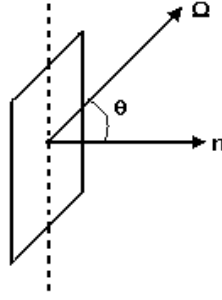
Figure 2.2 Unit area with normal in the direction of n [7]. Ω is the direction of motion of the photons and θ is the angle that it makes with the unit normal.

The spectral radiant energy flux through this area of an electromagnetic wave with a frequency υ is given by;

$$S_\upsilon = \int_{4\pi} I_\upsilon \cos\theta d\Omega .$$
(2.9)

If we consider a body which has a radiation field that is in equilibrium, the spectral radiant energy flux at any point inside this body would be zero since such a field would be isotropic. This also means that a plane surface inside this body has equal spectral radiant energy flux from left to right and right to left. This spectral radiant energy flux from left to right or right to left can be found by substituting equation (2.5) into (2.9) and integrating over the hemisphere;

$$S_\upsilon = \frac{c}{4}U_\upsilon = \frac{2\pi h\upsilon^3}{c^2}\frac{1}{\exp(h\upsilon/kT)-1} .$$
(2.10)

This equation is called the *Kirchoff's law* [7]. Note that a perfect black body is a body which absorbs all the radiation incident on it. The spectral radiant energy flux of such a body over all frequencies is equal to;

$$S = \int_0^\infty S_\upsilon d\upsilon = \sigma T^4 .$$

(2.11)

2.3 Electronic Transitions Inside the Plasma

2.3.1 Absorption and Emission of Radiation

Electronic transitions of the atoms or ions are a consequence of the emission and absorption processes inside the plasma. The absorption process results in

8

excitation of the atom or the ion and the emission process results in the de-excitation of the atom or the ion. But in order for the atom or the ion to emit photon, firstly it must be put into an excited state i.e. it must absorb energy from the surrounding.

There are two types of states for an electron which are the bound and free states [7]. In the bound state, the electron is attached to an ion or an atom so that it can only have discrete energy values. On the other hand if an electron is in free state, it is free from an atom or an ion and therefore it can have any energy value. From these considerations it can be said that the electronic transitions can be of three types i.e. bound-bound, bound-free and free-free.

In a bound-bound transition [7], the transition is from one discrete energy level to another. Thus the photons that cause the bound-bound transitions must have a well defined energy value $h\upsilon$ so that this energy corresponds to the energy between the two levels of the atom or the ion. The resultant spectra are line spectra due to either the absorption or emission processes. As for the bound-free transitions [7], they arise either from the photon absorption process or the electron capture process. Since both processes involve an electron that is in free state, the spectra are continuous. Finally in the free-free transitions [7], a free electron that is travelling in the electric field of an ion or atom can either emit a photon or it can absorb a photon. Free-free transitions involve the electrons in free state so that their spectra are continuous.

These electronic transitions are a consequence of radiative or collisional processes that take place inside the plasma. Summary of some of the bound-bound and free-free transitions can be seen in Table 2.1 [9]. In this table it is assumed that p and q are the excited states of the atom or the ion where p is a higher level than q. It is also assumed that when the atom or the ion is in the qth or p^{th} state, its ionization state is Z-1 where Z is the ground state of the ions or the atoms. When e which designates the electron is on the left hand side of the equation, it means that this transition is induced by the incidence of this electron and when it is on the right hand side it means that the electron is scattered. Above the arrows, either the rate constants or the probabilities of the transitions can be seen. Actually only the spontaneous emission has a probability, the rest is described in terms of rate coefficients. Here X(q,p) designates the collisional excitation rate coefficient from level q to p, X(p,q)

designates the collisional de-excitation rate coefficient from level p to q, $\alpha(q)$ designates the radiative recombination rate coefficient to level q, $S(q)$ designates the collisional ionization rate coefficient from level q and finally $\beta(q)$ designates the three-body recombination rate coefficient to level q. The rate coefficients give the probability of the reaction to take place inside the plasma. Thus as the probability has the units of s^{-1}, the rate coefficients has the units of $m^3 s^{-1}$.

Table 2.1 Summary of some of the bound-bound and bound-free transitions [9].

Spontaneous emission:	$p \xrightarrow{A(p,q)} q + h\upsilon$
Collisional excitation:	$q + e \xrightarrow{X(q,p)} p + e$
Collisional de-excitation:	$p + e \xrightarrow{X(p,q)} q + e$
Radiative recombination:	$Z + e \xrightarrow{\alpha(q)} q + h\upsilon$
Collisional ionization:	$q + e \xrightarrow{S(p)} Z + e + e$
Three-body recombination:	$Z + e + e \xrightarrow{\beta(q)} q + e$

The schematics of these transitions can also be seen in Figure 2.3 [9]. The dashed lines indicate a transition due to a radiative process whereas the solid lines indicate a transition due to a collisional process.
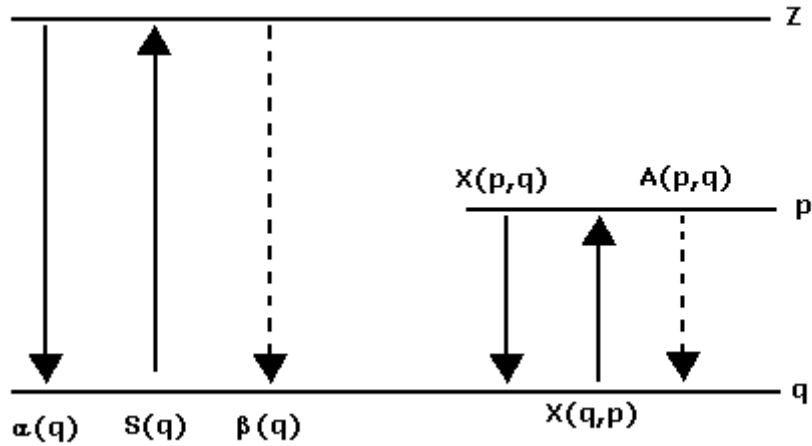
Figure 2.3 Schematics of the transitions given in Table 2.1 [9].

2.3.2 Bound-Bound Transitions

The Einstein Coefficients

There exist three purely radiative transitions between two bound levels which in turn determine the population of these two particular energy levels i.e. spontaneous emission, stimulated emission and absorption.

Consider two energy levels p and q where p is a higher state than q. In the spontaneous emission process, the atom or the ion is initially in an excited state which corresponds to the pth level in our case. Since when an atom or ion is in an excited state it tends to decay, the process at which this decay mechanism is in the form of an electromagnetic wave is called *spontaneous (radiative) emission* and the released wave will have the frequency;

$$\upsilon = (E_p - E_q)/h .$$ (2.12)

The rate of decay of these atoms or ions due to spontaneous emission is described by the equation [10];

$$\left(\frac{dN_p}{dt}\right)_{spont} = -A_{pq}N_p$$ (2.13)

where A_{pq} is the *spontaneous emission probability* or *the Einstein A coefficient* and N_p is the number of atoms or ions per unit volume at a given time that is in state p.

11

Assume again that initially the atom or the ion is in the excited state p. If an electromagnetic wave with frequency υ that is given by equation (2.12) is incident on the atom or the ion, there is a finite probability for the atom or the ion to undergo a transition from state p to q. This phenomenon is called *stimulated emission* and the rate of stimulated emission is described by the equation [10];

$$\left(\frac{dN_p}{dt}\right)_{stim} = -B_{pq}N_p \qquad (2.14)$$

where B_{pq} is the *stimulated emission probability*. The difference between the spontaneous emission and the stimulated emission is that in the spontaneous emission, the electromagnetic wave that is emitted by the atom or the ion does not have a phase relation with the one that is emitted from another atom or ion. But since in the stimulated emission process the radiation is due to the incidence of an electromagnetic wave, the emitted wave has the same phase relation with the one that is incident on the atom or the ion.

Finally in the absorption process, the atom or the ion is initially in the lower state q. As long as the qth level is the ground state level of the atom or the ion and unless an external stimuli is applied, it will remain in this state. But if an electromagnetic wave of frequency υ that is given by equation (2.12) is incident on it, the atom or the ion will undergo a transition from state q to p. This process is called *absorption process* and is described by [10];

$$\left(\frac{dN_q}{dt}\right)_{abs} = -B_{qp}N_q . \qquad (2.15)$$

Here N_q is the number of atoms or ions per unit volume at a given time that is in state q and B_{qp} is the *absorption probability*.

Relation between the Einstein Coefficients

In thermal equilibrium, the populations of the energy levels are described by the Boltzmann distribution. The Boltzmannian distribution between two energy levels is;

$$\frac{N_p}{N_q} = \frac{g_p}{g_q} \exp\left[-(E_p - E_q)/kT\right] = \frac{g_p}{g_q} \exp\left[-(h\upsilon)/kT\right] \qquad (2.16)$$

12

where g_p and g_q are the statistical weights or the number of degeneracies of the levels p and q respectively. These statistical weights are calculated from the equation;

$$g_i = 2J_i + 1 \qquad (2.17)$$

where J_i is the total angular momentum quantum number of the ith level [8].

When a system is in thermal equilibrium, the *principle of detailed balance* is valid for the system i.e. every atomic process is as frequent as its inverse [8]. Thus, the rate of total emission that is due to spontaneous and stimulated emission processes is equal to the rate of total absorption processes so that between levels p and q where p is a higher state than q [8];

$$\left[A_{pq} + B_{pq}U_\upsilon \right].N_p = B_{qp}U_\upsilon N_q \qquad (2.18)$$

from which the spectral energy density for frequency υ can be found as;

$$U_\upsilon = \frac{A_{pq}N_p}{B_{qp}N_q - B_{pq}N_p}. \qquad (2.19)$$

Substituting the relation between the number densities of levels p and q from the Boltzmann equation (2.16) gives;

$$U_\upsilon = \frac{A_{pq}}{B_{qp}\dfrac{g_p}{g_q}\exp\left[- (h\upsilon) / kT\right] - B_{pq}} \qquad (2.20)$$

and comparing this equation with the equation of blackbody radiation (2.1) would give us the relation between the Einstein coefficients as [8];

$$A_{pq} = \frac{8\pi h\upsilon^3}{c^3}B_{pq} \qquad (2.21a)$$

and;

$$\frac{B_{pq}}{B_{qp}} = \frac{g_q}{g_p}. \qquad (2.21b)$$

Rather than using the Einstein coefficients, the oscillator strength can be used [8];

$$B_{pq} = \frac{\pi e^2}{mh\upsilon}f_{pq} \qquad (2.22)$$

where f_{pq} is oscillator strength or the spectral line intensities can be used;

$$A_{pq} = \frac{64\pi^4}{3h\lambda^3 g_p}S_{qp} \qquad (2.23)$$

where S_{qp} is the spectral line intensity and λ is the wavelength and;

$$S_{pq} = S_{qp} \qquad (2.24)$$

13

is satisfied.

Collisional Excitation and Collisional De-excitation

In the collisional excitation process, an electron collides with an atom or an ion resulting in the excitation of this ion or the atom. In order for the excitation to take place, the energy of the colliding electron must be more than the excitation threshold [9]. The probability of this process is defined in terms of the collisional excitation cross-section [11];

$$X(q,p) = \int \sigma_{qp}(v)f(v)vdv \qquad (2.25)$$

where $\sigma_{qp}(v)$ is the collisional excitation cross-section due to electrons of velocity v and electron velocity distribution $f(v)$. For a Maxwellian velocity distribution this becomes [11];

$$X(q,p) = 1,6.10^{-5} \frac{f_{qp}G}{(kT_e)^{3/2}} \exp\left[-\frac{(E_p - E_q)}{kT_e}\right]. \qquad (2.26)$$

Here G is the Gaunt factor and f_{qp} is the oscillator strength of the transition from q to p. The collisional de-excitation coefficient is related to the excitation coefficient as [9];

$$X(p,q) = \frac{g(q)}{g(p)} \exp\left[-\frac{(E_q - E_p)}{kT_e}\right] X(q,p). \qquad (2.27)$$

2.3.3 Bound-Free Transitions

Radiative Recombination and Photoionization

If the bound-free transition is due to photon absorption process, an electron of the atom or the ion that is in a bound state acquires an amount of energy which exceeds the binding energy so that it is freed from the atom or the ion. This process is called *photoionization* or *photo-electric effect* and the excess energy is transformed into electron's kinetic energy. But if it is due to electron capture process, the process is called *radiative recombination* or *photorecombination* and a photon is released. The radiative recombination rate coefficient is given by [12];

$$\alpha(q) = \frac{8}{3\sqrt{3}} \frac{Z^2 n_e n_i}{m^2 c^3} \left(\frac{e^2}{4\pi\varepsilon_0}\right)^3 \left(\frac{m}{2\pi k T_e}\right)^{1/2}$$

$$\times \exp\left[-\frac{2Z^2 R_y}{q^3 k T_e}\right] \left(\frac{2GZ^2 R_y}{q^3 k T_e}\right)^{-1} \exp\left[\frac{Z^2 R_y}{q^2 k T_e}\right] .$$

(2.28)

Here n_e and n_i are the electron and ion densities respectively.

Collisional Ionization and Three-body Recombination

Ionization process can be assumed as a continuation of the excitation process, in that, the energy that the electron transfers this time to the ion or the atom during the collision is high enough to cause ionization. The collisional ionization rate coefficient for a Maxwellian velocity distribution can be written as [9];

$$S(q) = \frac{G}{Z^3} \left(\frac{Z^2 R_y}{\chi(q)}\right)^{7/4} f_{q,c} \exp\left[-\frac{\chi(q)}{k T_e}\right]$$

(2.29)

where $\chi(q)$ is the energy that is needed to transfer the electron from state q to continuum i.e. it is the ionization energy.

Three-body recombination is a process that is due to the collision of an ion or an atom that is in an excited state with a free electron, i.e. it is the inverse of the collisional ionization process. As a result of this collision, the excited atom or the ion returns to its ground state either by transferring the decay energy to the free electron or by emitting this energy as an electromagnetic radiation. Since in thermodynamic equilibrium the principle of detailed balance is valid, the relation between the collisional ionization and three-body recombination rate coefficients can be found as [9];

$$\beta(q) = \frac{N(Z-1, q)}{N(z, q).n_e} S(q) .$$

(2.30)

2.3.4 Free-Free Transitions

Bremsstrahlung and Inverse Bremsstrahlung

Free-free transition processes are bremsstrahlung and inverse-bremsstrahlung processes. As said before, a free electron that is travelling in the electric field of an ion or atom can emit or absorb a photon. If it emits, the process is called

Bremsstrahlung and if it absorbs the process is called *Inverse-Bremsstrahlung*. The bremsstrahlung emission coefficient is given by [12];

$$\varepsilon_\omega(T_e) = \frac{8}{3\sqrt{3}} \frac{GZ^2 n_e n_i}{m^2 c^3} \left(\frac{e^2}{4\pi\varepsilon_0}\right)^3 \left(\frac{m}{2\pi k T_e}\right)^{1/2} \exp\left[-\frac{h\upsilon}{kT_e}\right]. \tag{2.31}$$

It is worth to note that if the electron emits a photon, it does not necessarily mean that it looses all of its energy but it might still has enough energy to keep its free state.

The main mechanism that causes the transfer of the laser energy into the plasma is the inverse Bremsstrahlung absorption process [1]. The electrons inside the plasma begin to oscillate under the electric field of the laser and these oscillations cause the electrons to collide with the ions that are residing inside the plasma. As a result of these collisions, the electrons transfer their energies to the ions.

2.4 Spectral Line Broadenings

When an ion or atom absorbs or emits radiation in discrete quanta, a monochromatic radiation at frequency υ_0 is observed. However from the spectrometer that is used to observe this radiation, the output is seen as a spectral line with a spread in frequency around υ_0 having a line width of $\Delta\upsilon$ rather than a delta function. This width is defined at the full width at half maximum (FWHM) and decreases as the resolving power of the spectrometer increases which is defined as [11];

$$R = \frac{\upsilon}{\Delta\upsilon} = \frac{\lambda}{\Delta\lambda}. \tag{2.32}$$

Actually even if the resolving power is sufficiently high, the spectral lines observed still have a finite line width which may be due to a number of reasons. These line broadenings are a result of the environment of the radiating atoms or ions and the pressure and the temperature [13]. The collisional processes perturb the emitting atoms and ions inside the plasma which in turn determine the shape and width of the spectral lines emitted from the plasma. Some of the mechanisms that are responsible from the broadening of these spectral lines are natural, Doppler, pressure and Stark broadenings.

2.4.1 Natural Broadening

Natural broadening is the fundamental broadening i.e. it is the line width that is observed when an atom or ion is isolated, motionless and is shielded from electric and magnetic fields [11]. Thus it can be said that monochromaticity of a radiation is just an approximation.

When an atom or an ion is in an excited state, it either decays spontaneously or an interaction forces it to make a downward transition. In the case of an isolated atom, this downward transition can be due to spontaneous decay from which the natural lifetime of an atom or an ion can be found as [11];

$$\tau_{pq} = \frac{1}{A_{pq}}.$$
(2.33)

From the Heisenberg's uncertainty principle [14];

$$\tau \Delta E \geq \frac{h}{2\pi}.$$
(2.34)

Thus, the frequency spread due to natural line broadening can be found as [14];

$$\Delta \upsilon \geq \frac{A_{pq}}{2\pi}.$$
(2.35)

The line shape of natural broadening is Lorentzian. In comparison with the other broadening mechanisms, its effect is very small.

2.4.2 Doppler Broadening

For a plasma that is in vacuum environment, the expansion velocity of the plasma is high and one of the most contributing spectral broadening mechanisms is the Doppler broadening which is a result of the Doppler shift of the atoms and ions inside the plasma [5]. Doppler shift is a result of the movement of the particle that is radiating at wavelength λ towards or further from the observer. As a result of such a movement, the emitted line's wavelength is shifted. Since inside a plasma the radiating particles move randomly, Doppler broadening is inevitable.

2.4.3 Pressure Broadening

As the density of the plasma increases, the collisional processes become dominant and hence influence the output radiation from the plasma. In this case pressure broadening becomes the dominant broadening mechanism.

Actually there exist a variety of pressure broadenings. The most important of them is the Stark broadening which is described in detail below. The *resonance broadening* is the broadening that occurs due to the interaction between neutral atoms of the same kind when one of the states has an allowed transition to the ground state [11]. This type of broadening is proportional to the number density of the ground state atoms and oscillator strength [5]. When the interaction is between atoms of different kinds, the broadening observed is called *van der Waals broadening* [11].

2.4.4 Stark Broadening

In the case of high density and high temperature plasmas, the spectral line widths which are due to the transitions from the higher quantum numbers mostly undergo Stark broadening [8]. The reason for this is that in such a dense and high temperature plasma, the interaction of the radiating particles with their surroundings is very important.

Stark broadening on the other hand is a result of collisions inside the plasma which besides broadening, cause a shift in the peak wavelength [5]. The Stark broadening without the ionic contribution is [15];

$$\Delta\lambda_S = 2W\left(\frac{n_e}{10^{17}}\right) \tag{2.36}$$

where W is the electron impact parameter which attains different values for different temperatures. The line profile of Stark broadening is Lorentzian.

2.5 Opacity

Self-absorption mechanism or opacity or radiation trapping depends on the plasma properties which are density and temperature as well as the line parameters such as oscillator strength, level energies and level degeneracies. Mainly the resonance lines are affected from the self-absorption mechanism due

to their large oscillator strengths and high lower level populations. When the plasma plume expands through the vacuum, opacity is reduced due to the steep velocity and density gradients and the kinetic energies of the particles [5]. As for its effect on the calculation of the spectrum, it has two effects: First one is that the population densities of the energy levels are changed due to absorption and the second one is that the output intensity observed can no more be found by just summing the intensities from small volume elements in the direction of observation [6].

When a light beam passes through a medium, it is attenuated due to the absorption and scattering processes. This attenuation is the product of the attenuation coefficient or the total absorption coefficient μ_υ and the path length [7];

$$\tau_\upsilon = \int_0^x \mu_\upsilon dx \tag{2.37}$$

and is called the optical thickness or the optical depth of a layer x with respect to the light of frequency υ. This means that when a beam of parallel lights with initial intensity $I_{\upsilon 0}$ traverses a distance of length L inside a plasma starting from x=0, the beam intensity reduces to a value of [7];

$$I_\upsilon = I_{\upsilon 0} \exp\left[-\int_0^L \mu_\upsilon dx\right] = I_{\upsilon 0} \exp(-\tau) . \tag{2.38}$$

The total absorption coefficient μ_υ is the sum of the absorption coefficient $\kappa_{\upsilon a}$ and the scattering coefficient $\kappa_{\upsilon s}$ [7];

$$\mu_\upsilon = \kappa_{\upsilon a} + \kappa_{\upsilon s} \tag{2.39}$$

and the reciprocal of this coefficient gives the total mean free path where also the reciprocal of the absorption coefficient gives the absorption mean free path and the reciprocal of the scattering coefficient gives the scattering mean free path. These mean free paths in turn define the attenuation of light rays per unit length of the medium with respect to the process in concern.

2.6 Plasma Modelling of X-Ray Lasers

Modelling of x-ray lasers are used for the purpose of planning x-ray laser experiments and analyzing the results of these experiments. Emission from the plasma is calculated by taking into account the radiative and collisional mechanisms which populate and de-populate the energy levels. There are three types of emission models from a laser produced plasma; local thermodynamic equilibrium, coronal equilibrium and collisional radiative model. There exist fluid hydrodynamic codes which calculate the laser produced plasma parameters such as electron density and temperature and use then in modelling the emission from the plasma. EHYBRID [16], LASNEX [17], MEDUSA [18], and RADEX [19] are examples of fluid hydrodynamic codes. In order to calculate the total emission of the plasma, fluid hydrodynamic codes make use of co- or post-processor codes [20]. As an example to co- and post processor codes, RATION [21] and FLY [22] can be given. On the other hand, emission can also be calculated by directly modelling the emission models [23]. In calculating emission, these codes assume a single set of laser parameters i.e. electron density and temperature.

2.6.1 Modelling of the Emission from Laser Produced Plasma

Local Thermodynamic Equilibrium

Plasma that is formed by a pulsed laser system is a transient system. In such a system in order for LTE to take place, the electron-atom and electron-ion collisions must be fast and must dominate the radiative processes [5]. The difference between the complete thermodynamic equilibrium and LTE comes from the amount of blackbody radiation in the two systems. LTE roughly means that all the energy distributions except the radiation energy is the same as in a system of complete thermodynamic equilibrium [8].

In LTE model, particle collisions determine the distribution of electrons among various energy levels. But it is assumed that these collisions take place rapidly and that the distributions change instantaneously according to the changes inside the plasma that take place due to these collisions. From the principle of detailed balance, the result would be such that the energy levels of the

20

electrons would have the population densities as in a system of thermodynamic equilibrium.

In a system that is in thermodynamic equilibrium, the population densities are determined by using the equipartition theorem of the statistical mechanics which does not require any knowledge of the atomic cross-sections but depends only on the temperature, density and material composition. But inside a plasma, plasma temperature and density are local parameters so that they show variation both in space and time. Thus in a system that is in local thermodynamic equilibrium, population densities of the energy levels of the electrons are determined by using the local parameters of the plasma.

The energy level population distribution of the free electrons that have velocities between v and v+dv and that are in local thermodynamic equilibrium is determined by the Maxwell distribution;

$$dn_v = 4\pi n_e \left(\frac{m}{2\pi kT_e} \right)^{3/2} \exp\left[-\frac{mv^2}{2kT_e} \right] v^2 dv \qquad (2.40)$$

where m is the electron mass, n_e is the total density of free electrons, k is the Boltzmann constant and T_e is the electron temperature. If the electrons and ions have different temperatures, then they have different Maxwell distributions with temperature T_e for the electrons and T_p for the ions [8].

As for the population distribution of the energy levels of the two bound levels, they are determined by using the Boltzmann equation i.e. equation (2.16) and Saha equation;

$$n_e \frac{n_{Z+1}^p}{n_Z^q} = 2 \frac{g_{Z+1}^p}{g_Z^q} \left(\frac{2\pi mkT_e}{h^2} \right)^{3/2} \exp\left[-\frac{\chi_Z}{kT_e} \right] \qquad (2.41)$$

where n_Z^q is the number of particles in the Zth ionization stage with state q and χ_Z is the energy difference between the two energy levels in concern of the particle with state Z. Saha equation is actually an extension of the Boltzmann equation to ionized atoms so that the ratio of the number of particles in the Zth and the $(Z+1)^{th}$ state with states p and q respectively is found [8].

After finding the state of the electrons inside the plasma, the intensity of the radiation is found. This intensity is not only a matter of plasma transitions but also of opacity. If the plasma is optically thin then the intensity of radiation

21

emitted due to the transition from the pth energy level to the qth energy level is [6];

$$I_{pq} = \frac{1}{4\pi} \int n_p A_{pq} h\upsilon_{pq} ds \qquad (2.42)$$

where A_{pq} is the atomic transition probability from the pth level to the qth level, $h\upsilon_{pq}$ is the photon energy emitted and the integration is taken over the depth of the plasma that can be detected and the 4π factor is coming from the fact that this intensity obtained is the power per unit area per unit solid angle. The factor $n_p A_{pq}$ product is the radiative decay rate or the spontaneous emission rate of the transition from the pth level to the qth level.

As stated earlier, the continuum radiation is coming from the initially free electrons. Thus the total intensity at any particular frequency υ is the sum of free-free (bremsstrahlung) and the free-bound transitions (recombination radiation) at that particular frequency [6];

$$I(\upsilon)d\upsilon = \frac{1}{4\pi} \int n_e \sum_i \left[n(i)\gamma(i, T_e, \upsilon) + \sum_p n(i)\alpha(i, p, T_e, \upsilon) \right] .h\upsilon.ds.d\upsilon . \qquad (2.43)$$

Here, $\gamma(i, T_e, \upsilon)$ is the probability of a free electron with mean kinetic temperature T_e and that is in the field of an atom or ion that is specified by i, to produce a photon with frequency υ and $\alpha(i, p, T_e, \upsilon)$ is the probability of a free electron to make a free-bound transition to the pth energy level of the atom or ion that is specified by i and the integration is again taken over the depth of the plasma that can be detected. If the integration of equation (2.43) over all frequencies is taken, the total radiation emitted from the plasma can be found.

Electrons inside the plasma constitute the particles with the greatest velocity and so they are the ones that cause the most efficient collisional transitions. Thus in order to check whether the principle of detailed balance is satisfied or not, the collision rate of the electrons must be compared with the radiative decay rates from which the necessity condition of LTE can be given.

Consider that the atoms or ions undergo a transition from the qth state to the pth state due to a collision with an electron where the rate of the occurrence of these transitions are $n_e n_p X(T_e, p, q)$, and $X(T_e, p, q)$ is the de-excitation coefficient. Collisional de-excitation coefficient can be expressed in terms of the oscillator strength as [6];

22

$$X(T_e, p, q) = \frac{6,5.10^{-4}}{\chi_{qp} T_e^{1/2}} f_{pq} \exp\left[-\frac{\chi_{qp}}{kT_e}\right] cm^3 s^{-1} \qquad (2.44)$$

where χ_{qp} is the energy difference between the levels p (higher level) and q (lower level) i.e.;

$$\chi_{qp} = h\upsilon = E_q - E_p. \qquad (2.45)$$

In order for LTE to take place, the collisional de-excitation rate must be 10 times more than the radiative decay rate i.e. [6];

$$n_e n_p X(T_e, p, q) \geq 10 n_p A_{pq}. \qquad (2.46)$$

Collisional de-excitation coefficient can be expressed in terms of its inverse process as [6];

$$X(T_e, p, q) = \frac{g_q}{g_p} X(T_e, q, p). \exp\left[\frac{\chi_{pq}}{kT_e}\right]. \qquad (2.47)$$

By using equations (2.21a), (2.21b), (2.44) and (2.47) in equation (2.46), a more general criteria for the applicability of LTE model on the plasma can be found as [6];

$$n_e X(T_e, p, q) \geq 1,6.10^{12} T_e^{1/2} \chi_{pq}^3 \; cm^{-3}. \qquad (2.48)$$

Coronal Equilibrium Model

Principle of detailed balance in LTE model is between the collisional processes and their inverse collisional processes. On the other hand in coronal equilibrium model, the balance is between collisional ionization and radiative recombination and collisional excitation and spontaneous emission [6]. This stems from the fact that coronal equilibrium model is valid for sufficiently low density and high temperature plasmas. In such a plasma an excited atom or ion has sufficient time to emit radiation before it undergoes a transition due to a collisional process. The sufficiency condition therefore is that the electron density inside the plasma must be low enough to preserve the condition that the collisional transitions from an excited state must be slower than the radiative decay [24].

The formal description of the sufficiency condition for the coronal equilibrium can be given as follows: The collisional ionization and the three-body recombination occurring with equal rates in the LTE model means;

$$e + N_Z \Leftrightarrow N_{Z+1} + e + e. \qquad (2.49)$$

23

Since the ions can also combine radiatively with the electrons;

$$e + N_{Z+1} \rightarrow N_Z + h\upsilon .$$ (2.50)

If n_e is the ionization rate, then the three-body recombination is proportional to n_e^2 whereas radiative recombination is proportional to n_e. Thus for a sufficiently low n_e, the rate of radiative recombination is more than three-body recombination rate [6].

Steady State Coronal Equilibrium Model

The steady state approximation comes from the assumption that the change in the population densities of the levels that are due to the changes in the density and the temperature of the plasma is slow in comparison with the relaxation rate of the atomic processes. In the steady state coronal equilibrium model, the electrons inside the plasma have a Maxwellian velocity distribution. As for the energy of the particles inside the plasma, in order for the ion-ion collisions to be unimportant, the mean energy of the ions must be less than that of the electrons since otherwise they would have a comparable collision probability with that of the electrons.

As stated above, the density of the plasma is low so that the number of excited state ions is negligible in number in comparison with the ground state ions. Thus, if $S(T_e, Z, g)$ is the collisional ionization coefficient and $\alpha(T_e, Z, g)$ is the radiative recombination coefficient where g denotes the ground state then the balance between these two processes can be written as [6];

$$n_Z^g \, S(T_e, Z, g) = n_{Z+1}^g \, \alpha(T_e, Z+1, g)$$ (2.51)

so that the distribution of ions in the coronal model is independent of the electron density n_e. From this equation and the collisional excitation coefficient which is given in equation (2.26) and the radiative recombination equation which is given in equation (2.28), the steady state coronal model number density ratio of the ions with charges Z and Z+1 can be found as [6];

$$\frac{n_Z^g}{n_{Z+1}^g} = \frac{\alpha(T_e, Z, g)}{S(T_e, Z, g)} = 8{,}77.10^{-6} \, \frac{\chi_{Zg}^{\,11/4}}{kT_e} \exp\left[\frac{\chi_{Zg}}{kT_e}\right].$$ (2.52)

As for the population densities of the excited levels of the ions, they are determined by the principle of detailed balance between the collisional excitation rate and the spontaneous emission rate i.e. [6];

$$n_e n_Z^g \, X(Te, g, p) = n_Z^p \sum_{q<p} A_{pq} \,. \tag{2.53}$$

Thus, for the case of an optically thin plasma, the spectral line intensity emitted can be found by using the formula [6];

$$I_{pq} = \frac{1}{4\pi} \int ds \, n_e n_Z^g \, X(T_e, g, p) \frac{A_{pq}}{\sum\limits_{r<p} A_{pr}} \tag{2.54}$$

where the integration is over the length that is equal to the depth of the plasma as seen by the detector.

As stated before, the coronal equilibrium model is applicable for plasmas of low density and high temperature. The high temperature requirement here is that for a plasma with ionization of more than 1%, the temperature must be greater than $10^4 \, K^o$ [6]. As for the upper density limit of the plasma, the requirement for it can be found from the concept that the model will be inapplicable when the collisions begin to dominate the spontaneous emission process. Thus formally [6];

$$\sum_{r<p}^{g} A_{pr} \geq n_e X(T_e, p, q) \tag{2.55}$$

is the requirement for the coronal equilibrium model to be applicable. Conceptually, this equation must be satisfied for all excited levels p. But since as the principle quantum number increases the probability of spontaneous emission decreases, there exists an upper limit for the upper level principle number p. This upper limit of p must satisfy the criteria that there must be sufficiently high spontaneous emission transitions from this level and that these transitions must be strong enough to be detectable. The last criterion is that for the ions with $Z \leq 16$, the spontaneous emission transition energy must be close to the hydrogenlike energy value $13{,}6\left[\dfrac{Z+1}{p}\right]^2$ [6]. Thus the upper limit for p has been chosen as p=6. Taking into account these considerations, the electron density limit for the coronal equilibrium model to be applicable was found as;

$$n_e < 5{,}6.10^8 (Z+1)^6 \, T_e^{1/2} \, \exp\left[\frac{1{,}16.10^3 (Z+1)^2}{T_e}\right]. \tag{2.56}$$

The formal steady state condition can be found as follows: The rate of the last ion $Z=Z_s$ to be found is equal to the rate of ionization from the previous ion and the rate of recombination to give the previous ion so that [6];

$$\frac{dn_{Z_s}}{dt} = n_e \left[n_{Z_s-1} S(Z_s - 1) - n_{Z_s} \alpha(Z_s) \right] \qquad (2.57)$$

where

$$n_{Z_s-1} + n_{Z_s} = \text{cons}\tan t. \qquad (2.58)$$

Thus from these two equations n_{Z_s} can be found as;

$$n_{Z_s} = \frac{S(Z_s - 1)}{S(Z_s - 1) + \alpha(Z_s)} \left[n_{Z_s-1} + n_{Z_s} \right] \left[1 - \exp(-n_e \left[S(Z_s - 1) + \alpha(Z_s) \right] t) \right] \qquad (2.59)$$

so that the relaxation time criteria for the steady state model to be applicable can be found as [6];

$$\tau \geq \frac{1}{n_e \left[S(Z_s - 1) + \alpha(Z_s) \right]}. \qquad (2.60)$$

Time Dependent Coronal Equilibrium Model

In order to use a time dependent approximation to the coronal equilibrium model, plasma relaxation time must be smaller than the value given in equation (2.60). This time, differential equations which take into account the time change of the density and temperature of the plasma have to be used.

The first assumption for the time dependent approximation is that, the free electrons change their energies with elastic collisions fast enough so that the velocity distribution is Maxwellian. The second assumption is that the ionization and the radiative recombination take place within an atom or ion that is in ground state. For such a case, the rate of change of the population density of the ground state level of an ion with charge Z is [6];

$$\frac{dn_Z^g}{dt} = n_e \{ \left[n_{Z-1}^g S(T_e, Z-1, g) - n_Z^g S(T_e, Z, g) \right]$$
$$- \left[n_Z^g \alpha(T_e, Z, g) - n_{Z+1}^g \alpha(T_e, Z+1, g) \right] \} \qquad (2.61)$$

The third assumption is that the radiative decay is due to an inelastic collision that excites the ion to the pth state which decays afterwards. Thus the rate of change of the ion that is in the excited state p is given by [6];

$$\frac{dn_Z^p}{dt} = n_e X(T_e, Z, g, p) n_Z^g - n_Z^p \sum_{r<p} A_{pr}(Z). \qquad (2.62)$$

It is worth to note that as long as the atomic lifetime of the excited state level is much shorter than the relaxation process which is the case for low temperature

plasmas, the spectral line intensity emitted can be found by using equation (2.54).

Collisional Radiative Model

LTE model is valid for high density and coronal equilibrium model is valid for low density plasmas. As for the in-between case, collisional radiative model which was proposed by Bates et al. [25, 26] is used. Collisional radiative model is a model that was proposed to overcome the assumptions that restrict the plasma modelling in the coronal equilibrium model by including the secondary processes like three-body recombination. In terms of free electron velocity, it assumes that they obey the Maxwell distribution as in the coronal equilibrium model. Ionization in the plasma occurs due to electron collisions from bound levels which are this time partially balanced by three-body recombination [6];

$$N_Z^p + e \Leftrightarrow N_{Z+1}^g + e + e \qquad (2.63)$$

the electron collisions cause the transitions between two bound levels [6];

$$N_Z^p + e \Leftrightarrow N_Z^q + e \qquad (2.64)$$

and the emission of radiation is due to the spontaneous emission [6];

$$N_Z^p \rightarrow N_Z^q + h\upsilon \qquad (2.65)$$

and a free electron making a collisionless transition to a bound level of an ion [6];

$$N_{Z+1}^g + e \rightarrow N_Z^p + h\upsilon . \qquad (2.66)$$

Thus overall, the population densities of the bound levels are determined by the equation [6];

$$\begin{aligned}
\frac{dn_Z^p}{dt} = &-n_Z^p \{ n_e S(T_e, Z, p) + n_e \sum_{q \neq p} X(T_e, Z, p, q) + \sum_{q < p} A_{pq}(Z) \} \\
&+ n_e \sum_{q \neq p} X(T_e, Z, q, p) n_Z^q + \sum_{p < q} n_Z^q A_{qp}(Z) \\
&+ n_e n_{Z+1}^g \{ n_e \beta(T_e, Z+1, p) + \alpha(T_e, Z+1, p) \}
\end{aligned} \qquad (2.67)$$

where β designates the three-body recombination coefficient.

As the principle quantum number increases, the space between the two energy levels gets smaller. This in turn means that transitions due to the electron collisions which satisfy the relation (2.64) get dominant over the radiative transitions so that the radiative transitions can be neglected beyond a bound state level. In general it can be said that there is a boundary $p=p_{cr}$ which

determines whether the radiative or collisional processes are dominant inside the plasma, i.e. for $p<p_{cr}$ the decay process is mainly radiative and there is a balance like in the coronal equilibrium model and for $p>p_{cr}$, it is mainly collisional and the balance is called *excitation balance saturation*. Thus there is a means to determine this boundary which can be found by using the criterion;

$$n_e K(p_{cr}) = A(p_{cr}) \qquad (2.68)$$

which means that at the critical level, the total collisional decay equals to the total radiative decay. The total collisional decay can be given as [27];

$$K(p) = 6.10^{-14} p^4 \frac{\sqrt{T_e}}{Z^2 T_e + 2Z^4} (1 + \frac{1}{4}\varepsilon_p) \ln(\frac{2}{\varepsilon_p + 1.3}). \qquad (2.69)$$

Here;

$$\varepsilon_p = \frac{E_{ion} - E_{exc}}{kT_e} = \frac{\chi_{Zp}}{kT_e} \qquad (2.70)$$

where E_{ion} is the ionization energy of the ion and E_{exc} is the energy of the excited state with respect to the ground state. It is worth to note that the usage of a single electron temperature in the approximation means that the electron energy distribution is Maxwellian.

As for the excitation balance saturation in which the collisional decays dominate over the radiative ones, whether the collisional excitation or de-excitation are dominant in the plasma is determined by the parameter;

$$p_{hc} = Z\sqrt{\frac{R_y}{3kT_e}} \qquad (2.71)$$

where R_y is the Rydberg constant. In the case that $p<p_{hc}$ the plasma is cold and in the case that $p>p_{hc}$, it is hot.

In the case that the radiative transitions are negligible, Saha equation which is modified to the circumstances under concern can be used to find the population densities of these very high upper levels [6];

$$n_e \frac{n_{Z+1}^g}{n_Z^p} = 2 \frac{g_{Z+1}^g}{g_Z^p} \left[\frac{2\pi m k T_e}{h^2}\right]^{3/2} \exp\left[-\frac{\chi_{Zp}}{kT_e}\right]. \qquad (2.72)$$

Such a usage thus enables a simplification by using equation (2.72) instead of (267) for a p value that is exceeding a certain bound state level which depends on the plasma in concern.

It is worth to note that in the case of a steady state approximation, the factor $\dfrac{dn_Z^p}{dt}$ is set to zero. As for the quasi-steady state approximation, such an approximation can be made when the relaxation time of the ground state is longer than the relaxation time for the excited levels (i.e. the spontaneous emission lifetime), between the excited levels and the continuum of the free electrons. In such a case apart from the ground state which corresponds to p=1, $\dfrac{dn_Z^p}{dt} = 0$ and Saha equations are used.

2.7 EHYBRID

EHYBRID is a 1 dimensional hydrodynamic code which was written by using the FORTRAN language by G. J. Pert in the University of York, UK [16]. It was written for the purpose of modelling the interactions inside a laser produced plasma and the x-ray lasing output. The input data for the code is compromised of the atomic data that involves the transitions between levels of the lasing material and the material properties in concern and the pump laser parameters. The code describes many physical processes which include the laser energy deposition mechanism, hydrodynamical motion of the plasma formed as a result of this laser irradiation, electron thermal conduction and electron and ion thermalisation. The thermal conductivity of ions and electrons are modelled by using the Harm-Spitzer formula [28] which is valid for the case of electrons having mean free path smaller than the dimension of the temperature gradient. The code uses the collisional radiative model to simulate the time dependant ionization process [29] which also includes the escape factor calculations for the opacity effect. The escape factors can be changed from the input file (in terms of percentage). The atomic data and the population of excited ions is very important for the success of such a simulation since they both determine the quality of the simulation output.

The laser energy is absorbed by the inverse bremsstrahlung absorption mechanism. The inverse bremsstrahlung coefficient calculation includes the propagation of laser light towards the target surface and its backreflection from the critical surface. The coupled rate equations include collisional excitation and de-excitation, radiative decay, collisional ionization, three-body recombination and radiative recombination mechanisms [30]. For the principle of detailed

balance of three-body recombination, the ionization approximation of Golden et al. [31] is used. Apart from the radiative loss mechanisms, the other radiative mechanisms which are absorption and stimulated emission are not included in the code.

In order to simulate the plasma fluid, the code uses 98 Lagrangian cell matrices in the direction away from the target and the output of the code includes the calculated plasma parameters of each of these cells which include the electron temperature, electron density, gain and ionization in terms of the cell position and time. The target modelled is a planar target. Here, the fluid extends in the direction parallel to the laser irradiation direction with the lateral isothermal assumption and the transverse expansion of the plasma is assumed to be similar to the longitudinal one [16].

EHYBRID code solves the density profile in the direction that is normal to the target surface and assumes that along the line of focus length and across the line of focus width, the densities are of Gaussian shaped. Thus the code approximates three dimensional expansion of the plasma and because of this approximation, it is sometimes referred as 1.5 dimensional code. The density profile is calculated by using the continuity equation and Navier-Stokes equation which are for a one-dimensional case respectively [1];

$$\frac{\partial \rho}{\partial t} + \frac{\partial}{\partial x}(\rho v) = 0 \tag{2.73}$$

and;

$$\rho \frac{\partial v}{\partial t} + \rho v \frac{\partial v}{\partial x} = -\frac{\partial p}{\partial x}. \tag{2.74}$$

Here ρ is the plasma density, v is the plasma velocity, p is the pressure and x is the spatial dimension that is normal to the target surface. The continuity equation is the fluid equation of conservation of mass and the Navier-Stokes equation gives the momentum balance inside a fluid [1].

The plasma pressure is equal to;

$$p = n_i \left[kT_i + Z \times kT_e \right]. \tag{2.75}$$

For an isothermally expanding plasma, if the velocity in the direction of x satisfies the rarefaction solution i.e. [1];

30

$$v = c_s + \frac{x}{t} \tag{2.76}$$

where the speed of sound c_s is equal to [32];

$$c_s = \frac{[3kT_i + ZkT_e]}{Mm_i}, \tag{2.77}$$

by using the continuity equation, Navier-Stokes equation, the pressure value and the plasma velocity one can find [1];

$$n_i Mm_i \frac{c_s}{t} = -k[T_i + ZT_e]\frac{\partial n_i}{\partial x}. \tag{2.78}$$

From which the ion number density can be found as [1];

$$n_i = n_0 \exp\left(-\frac{Mm_i c_s}{k[T_i + ZT_e]}\frac{x}{t}\right) \tag{2.79}$$

where n_0 is the ion number density at x=0.

2.8 NeF

NeF solves the steady state rate equations for a given electron temperature and density for a collisional radiative model in order to determine the level populations. In the code, the intensity of emission is calculated by multiplying the emissivity with the escape factor τ;

$$I(\lambda) = N_p \frac{hc}{\lambda} A_{pq}\tau \tag{2.80}$$

where N_p is the population density of the pth level and A_{pq} is the transition probability of the spontaneous decay from level p to level q. In order to calculate the escape factor, the code makes use of the Holstein formula [33];

$$\tau = \frac{1}{\mu_0 D\sqrt{\pi \ln(\mu_0 D)}} \qquad \text{for } \mu_0 D \geq 2{,}5 \tag{2.81}$$

$$\tau = \exp\left[-\frac{\mu_0 D}{1{,}73}\right] \qquad \text{for } \mu_0 D < 2{,}5 \tag{2.82}$$

where D is the plasma length and μ_0 is the absorption coefficient. Here, the absorption coefficient was calculated by [34];

$$\mu_0 = \frac{A_{pq}\lambda^3}{8\pi c}\frac{\lambda}{\Delta\lambda}\left[\frac{g_p}{g_q}N_q - N_p\right] \tag{2.83}$$

where N_q is the population density of the qth level and g_p and g_q are the statistical weights of the pth and q^{th} levels respectively.

CHAPTER 3

GRAZING INCIDENCE PUMPING SIMULATIONS OF SOFT X-RAY LASERS FROM NEON-LIKE TITANIUM AND NICKEL-LIKE MOLYBDENUM WITH EHYBRID

3.1 Mechanisms that are used for Achieving Population Inversion

The classification of x-ray lasers are basically made according to their excitation mechanism. There exists various kinds of excitation mechanisms some which are recombination scheme, electron collisional excitation scheme, transient collisional excitation scheme, optical field ionization, inner shell photoionization and resonant photoabsorption.

3.1.1 Recombination Scheme

Recombination x-ray laser scheme was proposed by Gudzenko and Shelepin in 1965 [35]. In this scheme, the ions inside the plasma undergo recombination – which is mainly three-body recombination - due to the rapid expansion and so cooling of the plasma. This way, the electrons are placed to higher energy levels from which they cascade decay to a lower energy level due to collisional radiative relaxation. The decay to the ground state is slowed down at an energy level which has a longer lifetime than the upper lying levels, thus forming the population inversion [36]. The main problem concerning this scheme is the radiative recombination that causes the direct replacement of the electron to the lower laser level since in such a case, the population inversion is reduced and the lower laser level is filled up. In order to prevent such an outcome, the plasma must have a very low electron temperature. This requirement stems from the fact that the three-body recombination rate has a $T_e^{-9/2}$ dependence on the plasma electron temperature [36]. Also in order to have a high gain by keeping the temperature low, the plasma must also be of high density. In order

to achieve this high density low temperature plasma, the plasma is firstly heated by a laser pulse so that a high density is achieved and then rapidly cooled down after the irradiation has stopped [37].

The first lasing signal from a recombination x-ray laser was realized by Suckewer et al. in 1984 at Princeton University [38]. As said before, in order for the recombination to take place, the plasma has to be cooled down. But cooling of the plasma due to expansion brings the problem of rapid decrease in electron density and so a plasma that is long lasting cannot be achieved. Because of this, in this first demonstration they have applied a 9 T solenoidal magnetic field in order to confine the plasma so that the cooling mechanism would be due to the radiation losses. The laser that they have used was CO_2 laser with a 300 J of pulse energy and 75 ns of pulse duration at FWHM. The solid target that they have used was a carbon target and the lasing was obtained at 18,2 nm which results from the Balmer α-line transition between the n=3 and n=2 levels of C^{+5} ions in the recombining plasmas.

Hydrogen-like Ion Recombination Scheme

The research on the hydrogen-like ion recombination scheme began with the investigation of the population inversion of the C^{+5} ions [39, 40]. It was then proposed that the population inversion was achieved for Balmer α-line transition between levels n=3 and n=2.

In the case of shorter wavelengths recombination x-ray lasers, the rapid decrease in temperature due to adiabatic expansion becomes less effective in recombination process. The main reasons for recombination in such a case is the thermal conduction to colder regions of the plasma and radiation cooling.

As an example of hydrogen-like scheme, the recombination scheme for a hydrogen-like carbon VI (C^{+5}) ion can be seen in Figure 3.1 [41].
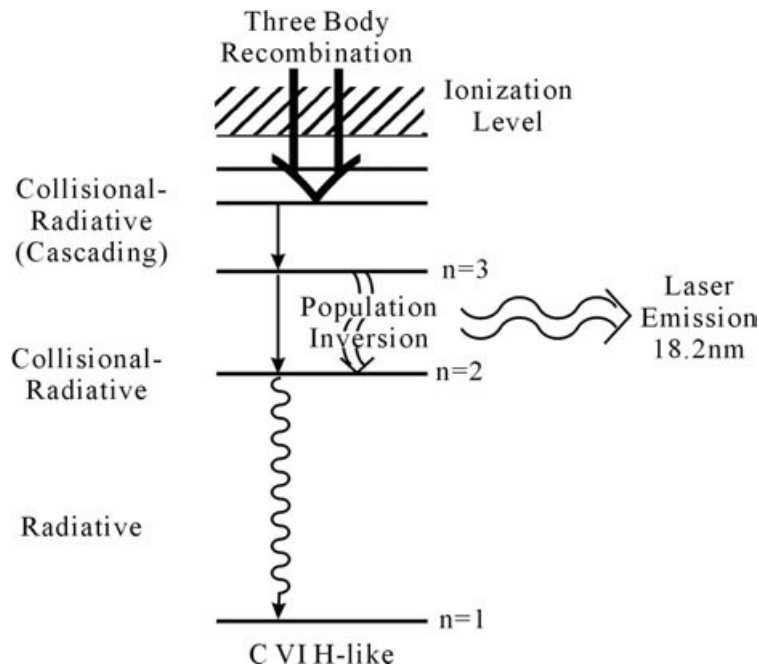
Figure 3.1 Recombination scheme for an H-like C VI ion. Lasing occurs from Balmer α-line [41].

Lithium-like Ion Recombination Scheme

The first demonstration of lithium-like population inversion due to the ion recombination scheme was performed by Jaegle et al. [42] in 1978. They have observed population inversion due to ion recombination of aluminium plasma. The transitions of the lithium-like ions were defined as 4f-3d and 5f-3d again by Jaegle et al. in 1987 [43]. Later on Jamelot et al. [44] have analysed this experiment and have made observations on the physical aspects of this experiment. Firstly they have observed that closed shell helium-like ions that are in ground state are vast in number for a big range of plasma density and temperature. Thus they have concluded that the main source of population inversion was the ground state helium-like ions inside the plasma which can produce lithium-like ions. They have also observed that these ground state helium-like ions emit an intense resonance line radiation so that this emission contributes to the plasma cooling process. Secondly they have observed that the 3d-2p radiative decay of the lithium-like ions is very fast so that the population of the 3d level is very low. Finally they have observed that the ionization potential of the lithium-like ions is lower than the energy of the lasing transition

35

so that in order to obtain a lithium-like ion recombination scheme, the plasma temperature is very low which in turn means that the pump energy needed is low.

3.1.2 Electron Collisional Excitation Scheme

In a plasma that is in equilibrium, ions with closed shells such as helium-like (2 electrons), neon-like (10 electrons), nickel-like (28 electrons) are more stable than the other ions so that they preserve their existence for a large plasma density and temperature range. In such a relatively stable plasma, the mechanism that creates the population inversion is the electron collisional excitation [41].

In the electron collisional excitation scheme, population inversion is achieved due to electron collisional excitation from the ground state of the closed shell ions to both the upper and lower laser levels [36]. This is achieved by heating the plasma with laser irradiation. The upper lasing level is metastable to the radiative decay to the ground state and the lower laser level is a level that decays very fastly to the ground state so that in order for this scheme to operate properly, the plasma must be optically thin to the transitions from the lower laser level [37]. Since the ionization energy needed to obtain a closed shell configuration is large, the electron collisional excitation scheme needs high pump energy [41]. The occurrence of the population inversion is due to the large radiative decay rate difference between the upper and lower laser levels. As can be seen, the electron collisional excitation scheme operates as long as the conditions for the generation of population inversion is supplied [37].

This population inversion scheme has been firstly proposed by Zkerikhin et al [45] in 1976 for 3p-3s transitions of neon-like ions. The theoretical aspect of this scheme was further explained by Vinogradov et al. [46]. The first demonstration of electron collisional excitation scheme was made in 1984 in the LLNL by Matthews et al. [3] from neon-like selenium ions for a wavelength range of 20,63 - 20,96 nm. The exploding foil technique which corresponds to the case of complete ablation of the target foil was used and the laser that was used for irradiation was an Nd:Glass laser having a kJ scale pulse energy. The electron collisional excitation scheme for the nickel-like ions on the other hand was firstly proposed by Maxon et al. in 1985 [47]. The first saturated

36

amplification for the nickel-like scheme was shown by Zhang et al. in 1997 [48, 49]. They have showed x-ray lasing for nickel-like samarium at 7,3 nm and nickel-like silver at 14 nm. The pump laser was an Nd:Glass laser operating at 1,05 μm at a pulse duration of 75 ps. The spot size was 100 microns and the intensity of irradiation was 4.10^{13} W/cm^2.

Transient Collisional Excitation Scheme

Transient collisional excitation scheme is a special case of the electron collisional excitation scheme at which the excitation rates from the ground state to the upper and lower levels have a great difference so that an extremely high and short-lived or transient population inversion occurs [36]. This is achieved by rapidly heating the plasma such that the rate at which the plasma is heated is higher than the relaxation rate of the excited states. This rapid transient heating generates a higher population inversion than the case seen in electron collisional excitation scheme. The reason for this is attributed to the fact that the rapid collisional excitation populates the upper laser level more than the other levels - before collisions take place and redistribute the populations again - due to its larger rate of excitation than the other levels. In this very short time period, gain that can be achieved from the plasma becomes very high which further drops down due to the redistribution of the population among the energy levels [37]. In order to achieve this in a transient collisional excitation scheme, a nanosecond scale prepulse and an ultrashort scale main pulse is used to irradiate a target material. In such a case, the prepulse forms a strongly nonequilibrium transient preplasma where a closed shell ionization stage is achieved. When the main pulse is used to irradiate such a plasma, population inversion is established since this main pulse excites the higher energy electrons from the ground state to the upper lasing level. This main pulse must be long enough to create population inversion and short enough not to cause further ionization in order for this scheme to work [41]. The transient nature of gain was attributed to the ionization balance inside the plasma which is due to the domination of the electron collisional excitation of ions over the ionization process due to the ultrashort pulse duration of the irradiating laser [50].

The advantages of a transient collisional excitation scheme have been given by Afanasev and Shlyaptsev as [41, 51];

(i) The achievability of the population inversion is independent of the electron density but as the electron density increases so does the population inversion.

(ii) The recombination processes in the formed plasma is small since the scheme works in a rapidly ionizing plasma so that gain coefficient is high.

(iii) The dimension of the plasma is not restricted.

(iv) The pump power requirement of the irradiating laser is small.

It is worth to note that travelling wave pumping increases the output intensity of the x-ray laser appreciably.

3.1.3 Optical Field Ionization

Burnett and Corkumm were the first to propose that optical field ionization can be used as a method in realizing x-ray lasers in 1989 [52]. In this method, population inversion is achieved by making use of the incident laser polarization. If the incident laser beam is linearly polarized, optical field ionization generates a cold plasma by promoting ionization and thus recombination processes would dominate. But if the incident laser beam has circular polarization, then a high temperature plasma would be created due to the suppression of ionization so that population inversion is achieved by electron collisional excitation [36]. The main disadvantage of optical field ionization is the usage of low density gas for plasma production since this results in low emission intensity. In order to solve this problem, interaction between the plasma and the laser light must be large but this in turn brings out the refraction due to ionization.

The first demonstration of electron collisional excitation due to the optical field ionization was done by Lemoff et al. in 1995 [53]. They have obtained lasing at 41,8 nm for a palladium-like xenon by using a Ti:Sapphire laser of 10 Hz repetition rate, 50 fs pulse duration and 50 mJ of pulse energy. As for the first saturated output, it was obtained for nickel-like krypton at 32,6 nm wavelength [54]. The first demonstration of recombination scheme due to optical field ionization on the other hand was firstly made by Nagata et al. in 1992 for the hydrogen-like lithium at 13,5 nm [55].

3.1.4 Inner Shell Photoionization

In this scheme, high energy photons are used for exciting the electrons to the upper laser level for population inversion. This type of population inversion was firstly suggested by Duguay and Rentzepis in 1967 [56]. At photon energies just above the threshold for inner shell ionization, the cross-section of the inner shell electrons is higher than that of the outer shell electrons. This is what makes the population inversion due to inner shell ionization possible. The high energy x-ray photons that pump the laser media are produced from the irradiation of high Z materials like gold with an intense laser pulse [37].

3.1.5 Resonant Photoabsorption

This scheme is also a scheme which involves excitation due to energetic photons [37]. In order to establish population inversion, this scheme requires that the wavelength of pump laser must coincide with the line that will be populated due to resonant photoabsorption from the highly populated state (like ground state) [37]. Although until now soft x-ray lasing due to resonant photoabsorption has not been demonstrated, it has been reported that amplification has taken place due to resonant photoabsorption of the 3d-2p resonance line for a neon-like argon soft x-ray laser at 45,1 nm [37].

3.2 Gain and Refraction

3.2.1 Gain from an X-ray Laser

As laser light traverses the active medium, the irradiance is amplified according to the equation [1];

$$\frac{dI(\upsilon)}{dz} = G(\upsilon)I(\upsilon) + E(\upsilon) \qquad (3.1)$$

where z is the distance which is traversed by the laser light in the active medium, $I(\upsilon)$ is the irradiance, $G(\upsilon)$ is the gain coefficient and $E(\upsilon)$ is the spontaneous emission rate. The spontaneous emission rate is equal to [1];

$$E(\upsilon) = n_p A_{pq} f(\upsilon) h\upsilon \frac{\Omega}{4\pi} \qquad (3.2)$$

where A_{pq} is the spontaneous emission transition probability from the upper level p to the lower level q, $f(\upsilon)$ is the normalized line shape function, n_p is the upper laser level population and Ω is the solid angle.

The gain coefficient is the product of the stimulated emission cross-section $\sigma(\upsilon)$ and the population inversion density Δn and for the energy levels that are in LTE, it can be written as [1];

$$G(\upsilon) = \sigma(\upsilon)\Delta n \cong \frac{A_{pq}\lambda^2}{8\pi} f(\upsilon)\left[n_p - n_q \frac{g_p}{g_q} \right] \tag{3.3}$$

where the population inversion density is equal to [37];

$$\Delta n = \left[n_p - n_q \frac{g_p}{g_q} \right]. \tag{3.4}$$

The line shape function is determined by the line broadening mechanisms that are seen in the system. When the broadening mechanisms are natural or collisional broadenings, the lineshape function is Lorentzian and is of the form [1];

$$f_L(\upsilon) = \frac{1}{\pi\Delta\upsilon_L} \frac{2}{1 + 4\upsilon^2/(\Delta\upsilon_L)^2} \tag{3.5}$$

where $\Delta\upsilon_L$ is the frequency at FWHM of the line profile in consideration. On the other hand when the broadening mechanism is Doppler broadening, the lineshape function is Gaussian and if the ion velocity distribution is Maxwellian it is of the form [1];

$$f_D(\upsilon) = \frac{2\sqrt{\ln 2}}{\sqrt{\pi}\Delta\upsilon_D} \exp\left[-4\ln 2 \frac{\upsilon^2}{(\Delta\upsilon_D)^2} \right]. \tag{3.6}$$

Here $\Delta\upsilon_D$ is the frequency at FWHM of the line profile in consideration and is equal to [1];

$$\Delta\upsilon_D = 2\sqrt{\ln 2} \frac{1}{\lambda}\left(\frac{m}{2kT_i} \right)^{1/2}. \tag{3.7}$$

The most efficient operation of any laser takes place when the gain from the active medium is saturated. Typical lasers make use of the optical cavity to achieve gain saturation by making use of the optical feedback mechanism. However for x-ray lasers an optical cavity cannot be used since the time needed for a feedback is more than the time that gain is acquired. The reason for this is

the difficulty in maintaining the active medium under the conditions needed for amplification. For example in a transient collisional excitation scheme, the population inversion is short-lived and so there is no time for any feedback mechanism. Because of this reason, soft x-ray lasers make use of single or double pass for amplified spontaneous emission [37].

3.2.2 Refraction

Refraction effects the population inversion and so the gain. When the plasma density increases, so does the gain. However this is valid up to a certain point. When the number of electrons inside the plasma becomes sufficiently high, the population inversion is destroyed. Also this increase in the electron density causes refraction i.e. x-ray beams bend through the outer parts of the gain medium due to the electron density gradients in the transverse direction. The real part of index of refraction inside a plasma is [37];

$$\eta = \sqrt{1 - \frac{n_e}{n_{ce}}} \; . \tag{3.8}$$

Here n_{ce} is the critical density which is equal to [37];

$$n_{ce} = \frac{4\pi^2 c^2 m_e \varepsilon_0}{e^2 \lambda^2} \; . \tag{3.9}$$

3.3 Pumping Schemes

The first pumping scheme used was the single pulse scheme. In this case, irradiation of the slab target is either lateral i.e. normally incident on the slab target, or longitudinal i.e. the direction of the beam is almost parallel to the target surface. Both of these pumping directions had their own problems when used for heating purpose since they both introduce limitations to the conversion of the energy into excitation [57]. The problem of heating due to laterally directed beam is that it deposits most of its energy into the critical density surface because it is a region of high density and so high absorption. As for the problem of longitudinal heating, it causes ionization and excitation of particles and so nonuniform heating of the active medium takes place [57]. Because of this, prepulse technique and grazing incidence pumping scheme have been proposed in order to increase the intensity of the x-ray laser output.

3.3.1 Prepulse Technique

In the prepulse technique, at least two pump laser pulses are used for irradiation. The first pulse – which is called the prepulse – creates the preformed plasma from which no x-ray lasing occurs. After a time delay, a second pulse which is called the main pulse is used to irradiate this preformed plasma resulting in x-ray lasing signal. The prepulse is directed laterally whereas the main pulse is directed longitudinally to the target and so is directed along the axis of the plasma column. The usage of multiple pump laser beams brought the opportunity to have an intense x-ray laser output.

When the prepulse method is used, the main laser absorption mechanism is again the inverse bremsstrahlung [1]. The prepulse is used to ablate the target material and form a uniform plasma, and the second pulse i.e. the main pulse is used to provide a heating to this uniform plasma such that the temperature difference would provide the energy difference needed for the atoms and ions to excite to the upper laser level. Its advantage is that when the main pulse interacts with the preplasma, the produced x-ray laser undergoes a reduced refraction than in the case of a single pulse method. Besides, the usage of laser pulses with shorter pulse duration cause the refraction to be reduced when directed onto a preplasma in comparison with the longer ones. Also the usage of shorter pulse durations results in a gain duration that is also short [1]. This excitation which is a result of collisional processes must be faster than the radiative and collisional relaxation time of the upper lasing level [58]. As for the time delay that is presented between the two pulses, it causes the plasma to cool down. In such a case when the main laser pulse begins irradiation, the active medium absorbs some of the energy of the laser prior to the irradiation of the critical density surface by the laser light and the laser energy that is wasted for expansion is reduced [59]. The time delay that is given between the two pulses must be optimized in order to have a plasma that is uniform, that is in the appropriate ionization stage and that has low density gradient so that, when the ultrashort laser pulse propagates through the plasma, population inversion achieved is optimized [50].

3.3.2 Grazing Incidence Pumping

When a target is irradiated in the normal direction - as is the main pulse in the prepulse scheme -, the amplification region absorbs only 10% of the laser energy since the electron density is low and so only a small fraction of the energy can be absorbed. This results in an insufficient heating of the plasma and therefore a large amount of laser energy is needed for pumping the plasma [60].

In grazing incidence pumping scheme, a prepulse that is used to create a preplasma is irradiated by an ultrashort main pulse after a delay time at a grazing incidence angle. As a result of this irradiation, the incident laser light is refracted back towards the gain region which in turn increases the energy deposition into the system (Figure 3.2). Also at a surface near to the critical density surface, some of the incident beam is deflected back towards the incident beam. This results in an increase in the deposited energy in this region [57].
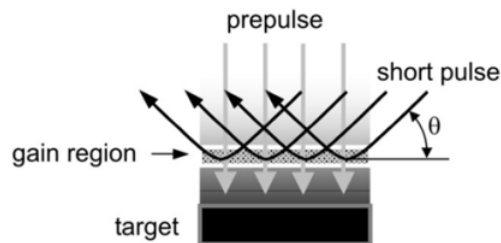
Figure 3.2 Grazing incidence pumping scheme [60].

Grazing incidence pumping is inherently a travelling wave pumping method. It makes use of the advantage of refraction of the pump beam by increasing the path length that is traversed by the pump beam in the gain region so that the energy absorbed is increased [61]. By using the grazing incidence pumping scheme, further reduction in the pump laser energy has been obtained than the prepulse transient collisional excitation scheme [62].

Absorption of laser energy by the plasma corona increases with a dependence of $1/\sin\theta$ where the angle θ is the grazing incidence angle. As light follows its path, refraction eventually turns the rays which in turn means that light passes through the gain region a second time. The turning point is the place where the density is maximum. Besides, irradiating with an angle means that no matter how the density gradients appear inside the plasma, refraction will make all light rays to pass through the same turning point [63].

The energy of the pump beam i.e. the main pulse, is deposited in a region of preselected electron density. This electron density is chosen such that the amplification of the x-rays are optimized. This optimization requires that the electron density and temperature are sufficiently high to produce population inversion due to transient collisional excitation and density gradients are sufficiently small so that the entire gain region can be used for amplifying the x-rays [60]. The electron density n_{e0} at which refraction occurs is the maximum electron density in the amplification region and it depends on only the grazing incidence angle and the electron density at the critical density surface [64];

$$\sin\theta = \sqrt{\frac{n_{e0}}{n_{ce}}} \; . \tag{3.10}$$

This in turn means that as the grazing incidence angle changes, the part of the plasma that is heated also changes. From this equation it can be said that if the grazing incidence is small, so is the maximum electron density and so is the gain [60]. But if it is large, the maximum electron density is also large meaning that the beam can penetrate deeper into the plasma and deposit its energy to a higher density region. However in such a case, the density gradients are also large so that amplification cannot be optimized. When the laser beam is refracted from this n_{e0} density surface, it passes through the gain region a second time so that its absorption in this region increases. Typically 20-50% of the laser energy is absorbed totally [60].

In order to optimize the x-ray laser output, two things are vital [60];
   (i)   X-ray refraction out of the gain medium must be minimized.
   (ii)   The difference between the speed of light and the pumping travelling wave speed must be smaller than the gain lifetime.

For a grazing incidence angle that is below 20°, this difference is very small and is approximately equal to [60];

$$\frac{L}{c}(1 - \cos\theta) \tag{3.11}$$

where L is the plasma column length. However for larger angles, it gets comparable to the gain lifetime.

3.4 Neon-like and Nickel-like X-ray Lasers

Neon-like closed shell has the principal quantum number n=2 and nickel-like closed shell has n=3 [65]. For both of these ions, collisional excitation pumping causes the lasing where for the neon-like, the dominant lasing is due to the $2p^53p \rightarrow 2p^53s$ transitions and for the nickel-like, the dominant lasing is due to the $3d^94d \rightarrow 3d^94p$ transitions. For both neon-like and nickel-like ions, the upper states are metastable to decay to the ground state since such a transition is electric dipole forbidden. Thus, the monopole excitation to the upper level is not balanced by radiative decay. As for the lower levels, the decays to the ground state are fast and direct by $2p^53s \rightarrow 2p^6$ and $3d^94p \rightarrow 3d^{10}$ resonance dipole transitions for the neon-like and nickel-like ions respectively [1]. The nickel-like ions have higher quantum efficiencies than the neon-like ones. Quantum efficiency is the ratio of the laser photon energy to the upper laser level energy which is pumped by collisional excitation. Due to this high quantum efficiency, the x-ray wavelengths that the nickel-like ions lase at are shorter than the neon-like ions [1]. The energy level diagrams of the neon-like and nickel-like ions can be seen in Figures 3.3 (a) and (b) respectively [1].

As long as the targets are chosen from the elements which can ionize at the electron temperature between 100 eV and 1 keV, neon-like and nickel-like x-ray lasers are very stable. The reason for this is that neon-like and nickel-like ions require a lot of ionization energy since they are closed shell ions that are in ground state. Also for this reason, they are found in large fractional amounts in the laser produced plasmas.
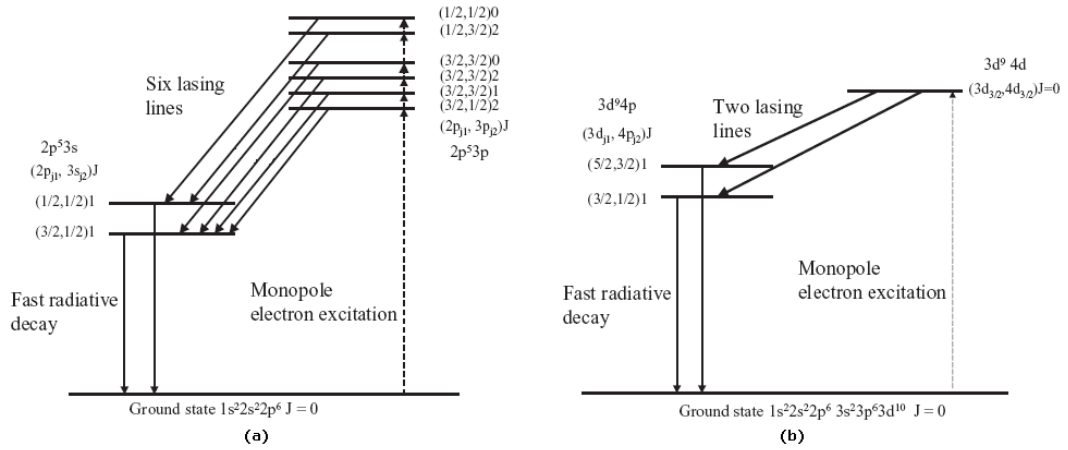
Figure 3.3 The energy level diagrams of (a) neon-like lasers. (b) nickel-like lasers [1].

3.4.1 Neon-like Titanium X-ray Lasers

Neon-like ground state configuration is the closed L shell configuration $1s^2 2s^2 2p^6$ [66]. Population inversion of the 3p level in the neon-like ions takes place due to the collisional excitation from the ground state, cascaded decay from the higher n states and due to the three-body radiative and dielectronic recombination from the fluorine-like ions [59]. 3s and 3d level electrons decay fastly to the ground state 2p by dipole transitions. As for the 3p level electrons, they are metastable to radiative decay to the ground state. Therefore lasing transition in the neon-like ions is due to the $3p \rightarrow 3s$ transitions among which the strongest ones can be given as $\left(\frac{1}{2}, \frac{1}{2}\right)_{J=0} \rightarrow \left(\frac{1}{2}, \frac{1}{2}\right)_{J=1}$, $\left(\frac{3}{2}, \frac{3}{2}\right)_{J=2} \rightarrow \left(\frac{3}{2}, \frac{1}{2}\right)_{J=1}$ and $\left(\frac{1}{2}, \frac{3}{2}\right)_{J=2} \rightarrow \left(\frac{1}{2}, \frac{1}{2}\right)_{J=1}$ transitions [59]. Here the numbers in the parentheses indicates the 2p and 3p j values respectively.

For the case of single pulse irradiation, the dominant $3p \rightarrow 3s$ transition is due to the $J = 2 \rightarrow J = 1$ transition [59]. As for the $J = 0 \rightarrow J = 1$ transition it is either very weak or not observed. In the single pulse irradiation case, the laser energy is deposited near the critical density surface. The plasma is hot and expands isothermally and as the laser irradiation continues, the ionization stage passes the neon-like stage. Because of this, the $J = 0 \rightarrow J = 1$ transitions can take place

46

at an early stage of the irradiation. At this early stage, the density gradients are steep and so the laser signal which is due to the $J = 0 \rightarrow J = 1$ transitions are refracted out of the active medium. On the other hand the $J = 2 \rightarrow J = 1$ transitions take place at a later time and at a lower density region so that the refraction that they are subjected to is less severe [59].

The same discussion is valid for the neon-like titanium x-ray lasers. The dominant transition of the neon-like titanium x-ray laser is due to the $3p \rightarrow 3s$ for the $J = 0 \rightarrow J = 1$ transition [62]. The resulting emission is at 32,6 nm. The upper laser level energy for neon-like titanium ions for this $J = 0 \rightarrow J = 1$ transition is 0,5 keV [58].

Experiments of Neon-like Titanium X-ray Laser

Boehly et al. [67] have made experiments by using two different laser systems. They have made use of a titanium slab target of thickness 125 micron for both laser systems. The first laser that they have used was a glass laser operating at 1,05 micron. The prepulse had a 1 J of energy and the main pulse was sent to the target after a delay of 7 ns. The main pulse had an energy of 200 J and pulse duration of 650 ps and it was focused such that its intensity was $1,7.10^{13}$ W/cm^2. As for the second one, it was a laser operating at 0,53 micron wavelength. Its energy was 550 J per pulse and the beam profile and the pulse duration were Gaussian and 600 ps respectively, resulting in a focused beam of similar intensity. The difference from the glass laser experiments was that they have irradiated simultaneously both sides of the target and a prepulse was also available. By using the glass laser for irradiation, they have stated that they have never observed lasing when the titanium slab was irradiated by a single pulse. They have observed this for three different single pulses; one which was Gaussian and of 600 ps pulse duration and the second and third which were square and of 1 ns and 2 ns pulse durations. As for the prepulse experiments, they have observed that the plasma is overly ionized from the neon-like stage. Indeed they have stated that resonant photoabsorption is taking place from the carbon-like and nitrogen-like titanium ions so that over-ionizing the plasma from the neon-like titanium stage is a requirement. They have proposed the resonant photopumping mechanism of the electrons from the ground state of neon-like titanium ions due to the carbon-like 3s-2p and nitrogen-like 3d-2p transitions.

In order to analyze the effect of prepulse in the system, they have performed simulations by using the 1D code LASNEX. From the simulation results they have stated that the irradiation of the solid slab target results in steep density gradients which is reduced by the usage of a prepulse. When a prepulse is applied to the system, these density gradients are smoothed so that x-rays can traverse a longer path in the gain medium than the single shot case before they are refracted to the outer parts of the plasma. Also they have stated that the usage of a prepulse results in a lower electron temperature which in turn means that the fraction of neon-like ions are more abundant than in a single shot case [67].

In the experiments that Zhang et al. [59] have performed, an Nd:Glass laser was used for irradiating a 1,8 cm long titanium target by the prepulse technique. The total intensity that they have used was 7 TW/cm^2 for which they have varied the prepulse intensity from 1% to 9% of the total intensity. The main pulse had a pulse duration of 650 ps and the prepulse had a pulse duration of 5 ns. As a result of the experiments they have observed a monochromatic lasing at 32,6 nm due to the $J = 0 \rightarrow J = 1$ transition and that when the prepulse intensity was 1% of the total intensity, they have observed that the x-ray laser output was more intense. Also they have made simulations by using the LASNEX code for main pulse energies of 50 and 150 J and for prepulse energies of 1% and 8% of the main pulse energy [59]. From the simulation results they have concluded that the plasma that is formed by a 1% energy prepulse is more uniform than the 8%. Also the density of the neon-like ions is more and the gain duration is longer than the 8% case.

Another prepulse experiment has been held by Nickels et al. [58] in 1996. In these experiments they have tried to produce neon-like titanium x-ray laser by using a 1053 nm Nd:Glass laser. The prepulse that they have sent had a pulse duration of 1,5 ns with an energy of 7 J and the main pulse had a pulse duration shorter than 0,7 ps with an energy of 4 J. The pulses were focused to a beam width of 30 microns. The length of the target was changed between 1 and 5 mm so that the effect of plasma column can be inquired. They have obtained lasing at 32,6 nm when the long pulse had an energy between 4 and 6 J and the long pulse had an energy of 1,5 J which was sent to the target after a delay of 1,5 ns [58]. Also when the plasma column was changed between 1 and 5 mm, they

have observed a nonlinear change of the output 32,6 nm emission with a maximum for the case of 5 mm. An important point is that they have observed that at the density surface of $n_e > (2-10).10^{20}$ cm^{-3} which is around $L \approx 1-3$ mm, the amplification of x-rays were stopped due to refraction.

The second emission of neon-like titanium that they have obtained was due to $3d \rightarrow 3p$, $J = 1 \rightarrow J = 1$ transition around 30 nm [58]. They have made the comment that this transition is emitted in a quasi steady state plasma and is due to the reabsorption of $3d^1P_1 - 2p^1S_0$ transition. It has been given different values for the wavelength of emission by different groups.

In order to measure the efficiency of the x-ray laser, they have made use of the ratio of gain length product to the input pump laser energy i.e. gL / E_p where E_p is in terms of kJ. In the experiments they have obtained a gL / E_p ratio of 1200 [58] which was 40 times more than the experimental results that were made by Boehly et al. [67]. The pulse duration that they have obtained was 20 ps for the 3p-3s transition and 15 ps for the 3d-3p transition. They have stated that the population inversion exists for the time <15 ps [58].

Nickels et al. [58] have made simulations concerning their experimental conditions by using the 1D hydrodynamic, nonlocal thermodynamic equilibrium code RADEX. They have observed from the simulation results that, the nanosecond prepulse creates a plasma of temperature $T_e \approx 120-180eV$ which is sufficient to ionize the plasma to the neon stage. As for the ps main pulse irradiation, it heats the plasma and deposits most of its energy near the critical density. The electron temperature near the critical density surface reaches to 2-3 keV at first but because of the ionization and the heat flux, it decreases to 0,4-0,6 keV. Later on due to the emitted radiation, ionization and expansion, plasma cools down.

As for a grazing incidence pumping experiment, the experiments that were held by Luther et al. [60] can be given. They have used a Ti:Sapphire laser with a central wavelength at 800 nm and 5 Hz repetition rate for irradiating the titanium target. The main pulse energy was 1 J and its pulse duration was 8 ps. They have used two prepulses for irradiation, both of which had a pulse duration of 120 ps; first had an energy of 10 mJ and the second had an energy of 0,35 J.

The delay between these two was 5 ns. The prepulses and the main pulse were focused to $4,1\,\text{mm} \times 30\,\mu\text{m}$.

They have used 4 mm long thick slabs in order to produce neon-like titanium x-ray lasers. During the experiments, they have obtained lasing at 32,6 nm due to the $3p \rightarrow 3s$ transition and 30,1 nm due to the $3d \rightarrow 3p$ transition. They have observed that if the delay between the second prepulse and the main pulse is 400 ps and 500 ps, the 36,2 nm emission is dominant. They have examined the output for the grazing incidence angles between 17°, 20° and 23° where the maximum emission intensity at this wavelength was observed for 20°. The 30,1 nm emission was also strong in the 20° and 23° however, the 32,6 nm was the dominant emission. As for the delay time, for a 20° of grazing incidence angle they have observed that the 32,6 nm emission is dominant at 620 ps [60].

On the other hand in 2006 Zhao et al. [62] have made simulations concerning the neon-like titanium grazing incidence pumped x-ray laser, for the emission of 32,6 nm by using a modified version of the one dimensional Lagrangian hydrodynamic code MED103 in order to diagnose the time evolution of the laser plasma interactions and gain coefficient. They have performed their simulations according to the experiments that were made by Alessi et al. [68].

The experiments of Alessi et al. were made by using an 800 nm central wavelength Ti:Sapphire laser with a 5 Hz repetition rate and Gaussian profile beam. They have used a slab target in their experiments and line focused the beam to $100\,\mu\text{m}$. They have firstly irradiated the slab target at normal incidence by two beams of 120 ps pulse duration which were separated by a time delay of 5 ns in order to form the preplasma. The intensity of the first and second prepulses were $2,37.10^{12}$ and $6,77.10^{10}$ W/cm² respectively. After a delay time, they have irradiated this time the slab target by a pulse of duration 8 ps which has an intensity of 1.10^{14} W/cm². The grazing incidence angles that they have applied were $17^{\circ}, 20^{\circ}$ and 23^{0}. As a result of these experiments they have concluded that the optimized delay time between the main pulse and main prepulse was 600 ps and the optimized grazing incidence angle was 20°. As for the simulation results from Zhao et al. [62], they state that they have obtained

the optimized angle of incidence as 20° also so that MED103 is a suitable tool for grazing incidence simulations.

Afterwards, in order to search for the minimum energy needed by the pump laser for saturated amplification and optimized delay time at a grazing incidence angle of 20° in the double pulse scheme, they have performed some simulations. They have chosen two prepulse durations, 300 ps and 1 ns with peak intensities 4.10^{11} and $2,5.10^{11}$ W/cm^2 respectively. The main pulse for the two cases was fixed which was 300 fs of duration and of 3.10^{14} W/cm^2 peak intensity. They have found that the simulations with the prepulse of 1 ns duration have resulted in bigger neon-like titanium density inside the plasma and so the gain obtained was more than the one for 300 ps prepulse. As for the optimum delay time, they have found that for the 300 ps prepulse the optimum delay time was 380 ps and for the 1 ns prepulse the optimum delay time was 700 ps. Since the simulation results for the 1 ns prepulse was better, they have tried to find the minimum main pulse energy needed for saturation. They have performed their simulations for a peak intensity range between 1.10^{14} and 4.10^{14} W/cm^2. As a result, they have found that this optimum intensity corresponding to the minimum pulse energy for a 300 fs main pulse is 3.10^{14} W/cm^2.

3.4.2 Nickel-like Molybdenum X-ray Lasers

The major x-ray lasing of the nickel-like molybdenum emission is at 18,9 nm [61]. This 18,9 nm emissions is a result of the $4d - 4p$ transition [69].

Nickel-like Molybdenum Experiments

Ozaki et al. [70] have made experiments by using the prepulse method for nickel-like molybdenum x-ray laser. They have used a hybrid Nd:Glass and Ti:Sapphire laser during the experiments. The prepulse had a pulse duration of 300 ps and the main pulse had 475 fs. The total pump energy was 150 mJ. The intensities of the prepulse and the main pulse were $1,5.10^{11}$ W/cm^2 and 3.10^{16} W/cm^2 respectively. The delay between the two pulses was adjustable between 1 and 10 ns. When the prepulse and the main pulse energies were 30 and 120 mJ respectively and when the delay introduced was 4 ns, they have observed that the dominant emission was at 18,9 nm with an energy of 27 nJ

per pulse. But considering the dimension of the lasing region which must be smaller than the spot size of the longitudinal pump beam, they have stated that the lower limit of the output is 3,8 mJ which is 1 order of magnitude smaller than the saturated regime.

Another prepulse experiment is the one that was made by Larotonda et al. in 2003 [69]. A Ti:Sapphire laser with a 5 Hz repetition rate was used in the experiments. The prepulse had an energy of 350 mJ with a pulse duration of 120 ps and the main pulse energy and pulse duration were 1 J and 8 ps respectively. The target was a slab molybdenum which was 4 mm wide and 2 mm thick. The prepulse and the main pulse were focused to $4,1\,mm \times 30\ \mu m$ resulting in a prepulse intensity of $2,4.10^{12}$ W/cm^2. The grazing incidence angles were chosen as 14°, 20° and 26°.

Under these experimental conditions, they have found that the most intense emission was at a grazing incidence angle of 20° when the delay time is optimized. The optimum delay for a grazing incidence angle of 20° was 500 ps. The refraction takes place at an electron density of 2.10^{20} cm^{-3} [69].

In the grazing incidence experiments that were performed by Keenan et al. [63], the main pulse and the prepulse durations were 1,5 ps and 200 ps respectively. They have made use of a Ti:Sapphire laser that is operating at 10 Hz to irradiate an 8 mm long slab target of molybdenum. The prepulse energy was 70 mJ at the target surface and the main pulse had an energy of 80 mJ with a grazing incidence angle of 14°. The delay between the two pulses was adjustable from 0 to 1000 ps. During the experiments they have tried to optimize the prepulse and the main pulse parameters such that the 18,9 nm emission would dominate the spectrum. As a result of an experiment under these conditions, they have obtained a near saturation regime.

Luther et al. [61] have used a Ti:Sapphire laser system operating at 800 nm wavelength with 5 Hz repetition rate and obtained a saturated output by using grazing incidence pumping scheme. The molybdenum target was of thickness 2 mm. They have obtained the best output when both the prepulse and the main pulse beams were focused to a FWHM width of 30 microns. The prepulse had a pulse duration of 120 ps and an energy of 320 mJ. As for the main pulse, it had

a pulse duration of 8,1 ps and an energy of 960 J. The grazing incidence angle was 14° and for this angle, they have found the optimum delay time as 700 ps. Also they have observed that strong lasing resulted for time delays between 500 and 1290 ps. As a result of this experiment, they have obtained a saturated x-ray lasing of nickel-like molybdenum at 18,9 nm and amplification of nickel-like molybdenum at 22,6 nm.

3.5 Ti:Sapphire Laser System

Ti:Sapphire laser systems rely on three things: Nonlinear optical Kerr effect for the generation of spectrally ultrabroad beams, control of dispersion and amplification of this ultrabroadband beam [71].

When a dielectric medium is irradiated at high intensities, the electric field is no more directly proportional to the polarization but includes a nonlinear term. The addition of this nonlinear term results in an instantaneous change of the refractive index of the dielectric material proportional with the intensity as a result of which, temporal delay due to the retardation of the most intense part of the beam takes place. This effect is called *optical Kerr effect* [71]. The retardation in the most intense part means that the plane wavefront acts like a focusing lens and the central part of the beam is retarded along the optical axis which is the axis of propagation. As a result, the leading part of the pulse is red shifted and the trailing part of the pulse is blue shifted. This is called *self-phase modulation* and it results in the broadening of the pulse [71]. Self-phase modulation itself does not cause to obtain an ultrashort pulse. In order to generate a shorter pulse, the red part of the beam is temporarily delayed and the blue part of the beam is temporarily advanced by using dispersion. *Dispersion* is the spectral dependence of the speed of light which is needed to shorten the spectrally broadened pulse [71].

In order to support the generation of ultrashort pulses, a feedback mechanism into the oscillator has to be introduced. If one works in the frequency domain, this can be achieved by phase-locking the longitudinal modes of the cavity. When the modulation frequency is equal to the frequency spacing of the modes an amplitude modulator is used to phase-lock these longitudinal modes. What this amplitude modulator does in the time domain is that, it synchronously opens and closes with the light propagating inside the cavity. This is called

mode-locking and if the opening and closing is driven by an external source it is called *active mode-locking* and if it is driven by the optical pulses inside the cavity it is called *passive mode-locking* [71]. In order to generate an ultrashort pulse, phase-locking of longitudinal modes as much as possible is needed since if the spectrum that is phase-locked is broad, then the pulse that is generated is short [71].

The passive mode-locked lasers make use of the saturable absorbers to achieve phase-locking. Some materials have the property that when the laser light intensity that they are being irradiated increases, the absorption coefficient decreases. Such materials are called *saturable absorbers* [72]. The Ti:Sapphire oscillator makes use of the passive mode-locking by means of self mode-locking [73]. It makes use of the nonlinear optical Kerr effect. When the intensity of the laser is sufficiently high, a Kerr lens is produced which in turn couples the spatial and temporal modes so that phase locking is achieved.

In a Kerr lens mode-locked laser oscillator, a small and constant amount of dispersion is needed [71]. When light passes through the Ti:Sapphire crystal, a group delay dispersion is introduced which results in the stretching of the pulse. This has to be compensated in order to achieve a small and constant dispersion value. For this reason, either prism pairs or dielectric mirrors are being used to compress the pulses. These dielectric mirrors or chirped mirrors are manufactured by layering a multiple number of the quarter-wave layer pairs onto each other. Such mirrors are produced such that they are optimized for a certain central wavelength. The penetration depth of a certain ray depends on the wavelength of the ray. As the wavelength increases, its penetration depth also increases.

The output of a Ti:Sapphire oscillator is in nJ scale. Although the pulse duration is of the order of femtoseconds, the average power is still very low. Because of this reason amplification of the beam to the mJ scales is needed. However the resulting beam would damage most of the optical materials since such a beam would have a peak intensity of the order of gigawatts per square centimetre [73]. In order to overcome this affect, the ultrashort pulses are first stretched and then amplified and then recompressed. This is called chirped pulse amplification and the stages of chirped pulse amplification can be seen in Figure 3.4 [73].
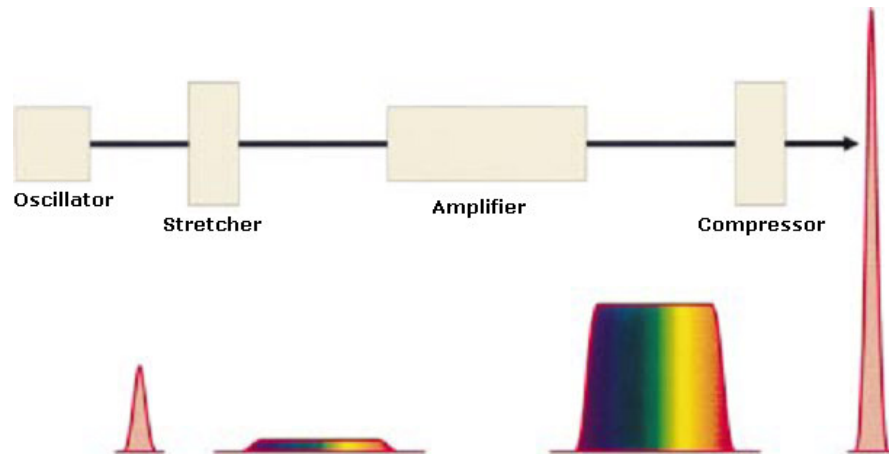
Figure 3.4 The stages of chirped pulse amplification [73].

In order to stretch and compress the pulses, the stretcher and compressor systems make use of the diffraction gratings. In the stretcher part, the pulse duration is stretched to the orders of picoseconds by making use of the spatial dispersion to introduce temporal dispersion. These stretched pulses are further sent to the amplifier stages. The amplifier stages are either of regenerative type or multi-pass type. Finally the amplified beams are compressed by using a pair of diffraction gratings.

The femtosecond laser oscillator in METU laboratory is a Femtosource Scientific oscillator and its layout can be seen in Figure 3.5 [74]. The optical pumping is supplied from a Coherent Verdi V5 laser, which is a diode pumped $Nd:YVO_4$ laser operating at the second harmonic 532 nm, continuous wave operation. The pumping power is 4 Watts.
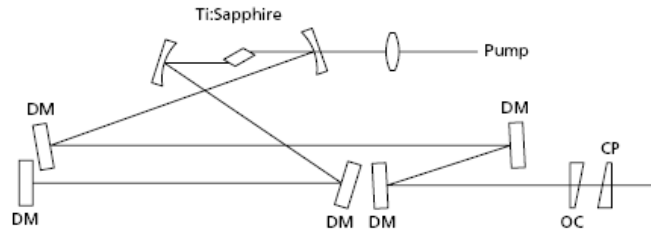
Figure 3.5 Femtosource Scientific Ti:Sapphire oscillator. DM designates that the mirror is a dielectric mirror, OC designates the output coupler and the CP designates the compensating plate [74].

The Ti:Sapphire oscillator is composed of two curved dielectric mirrors and plane dielectric mirrors in both the short and the long arm of the cavity. The output coupler is a wedge and the angular dispersion that it introduces is compensated by a compensating plate. The pulse duration and the spectrum output of the Ti:Sapphire oscillator can be seen in Figure 3.6. The repetition rate of the oscillator is 75 MHz and its output energy is in nJ scale.

After the oscillator, by using a beam splitter, a small part of the laser signal is converted into electric signal by using an EOT ET-2000 silicon photodiode and is sent to the pulse picker system for the reduction of 75 MHz to 10 Hz. This pulse picker system is composed of a Quantum Technology HVPM 9003 Pockels cell driver which also includes a divider and a delay unit and an HVP 590-DR-BM Pockels Cell which makes use of a KD*P crystal. The reduction of the pulses to 10 Hz is achieved by using the divider unit and by further taking into account the jitter of the cables and the machines and the optical path of the pulse, they are sent to the HVP 590 Pockels Cell for triggering purpose after an appropriate delay. After the pulse picker system, the pulse is sent to Dazzler for appropriate amplification and attenuation purposes so that the output beam remains Gaussian. After the dazzler, the pulses are stretched prior to amplification process. The stretcher is an Öffner triplet stretcher. It is composed of a gold coated, 800 nm blazed grating, a concave mirror of focal length 350 mm, a convex mirror of focal length -175 mm and a roof mirror. All the mirrors are gold coated in order to optimize the infrared reflection. Here, the pulses are stretched to 289 ps. The stretched, 10 Hz pulses are then further sent to the

56

crystal of the first amplifier stage. There exists two amplification stages, the first one is an 8 pass multi-pass amplifier and the second one is a 4 pass multi-amplifier system. In between these two amplifiers, the beam is passed from a Pockels Cell so that the unwanted prior and post pulses are suppressed. Finally, the amplified beam is compressed by using a pair of gold coated diffraction grating and a silver coated roof mirror system.
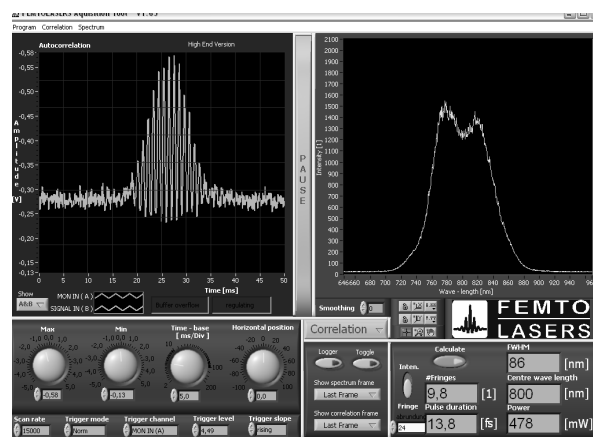
Figure 3.6 Autocorrelator results and the spectrum of the Ti:Sapphire oscillator. This output is obtained by using the Femtometer acquisition tool. The FWHM of the spectrum is seen as 86 nm. However, during the measurement absorption filters have been used so that this is a reduced value than the real one.

3.5.1 Timing for Amplification Purpose

After the oscillator, there is a timing concept such that prior to the time at which the pulse that was reduced to 10 Hz is sent to the crystal, the beam from the Nd:YAG laser must have already pass it so that amplification can be realized. Actually, since the first amplifier stage is an 8-pass amplifier, the time by which the beam makes all its 8 passes from the crystal must be smaller than the first $3,2\,\mu s$ that the beam coming from the Nd:YAG laser passes from the crystal. For this reason, delay times of the instruments must all be taken into account.

The layout of the timing system in the Ti:Sapphire laser can be seen in Figure 3.7. In order to make this system work properly, firstly the delays that are introduced by the system components must be defined. The photo diode used is an EOT ET-2000 silicon photodiode and let its jitter be denoted by t_{PD}. The amplifier is a Stanford Research Systems SR445A 4-Channel DC 350 MHz amplifier with a jitter of 2,7 ns per channel [75]. Besides, it makes use of 3 RG 59 cables to amplify the signal coming from the photodiode. Also each system component is connected with an RG 59 cable and the jitter that an RG 59 cable introduces is 4 ns/m. The delay time that is introduced by the Pockels Cell driver is seen in Figure 3.8 [76]. As for the Stanford Research Laboratories DG 535 delay generator and dazzler, the delay generator introduces at most an 85 ns of jitter when externally triggered [77] and the jitter of the dazzler depends on the period of oscillation of the triggerer. For a triggerer operating at 10 Hz, the delay is more than 100 ms where the 100 ms delay comes from the Dazzler generator which samples the rising edge with the next internal clock pulse and so the period of oscillation and the rest comes from the electronic circuits and so is very small in comparison with 100 ms [78]. Finally, CFR 400 Big Sky laser flashlamp has a jitter up to 10 μs and q-switch has a jitter of ±500 ns [79]. Keeping in mind these values, the delays that are introduced into the system components without taking into account the delays introduced by the Pockels Cell Driver and delay generator are;

$$t_{PCD} = t_0 + t_{PD} + t_1 + t_{Amp} + 3t_{Cab} + t_2 \tag{3.12}$$

$$t_{PCTrig\,2} = t_0 + t_{PD} + t_1 + t_{Amp} + 3t_{Cab} + t_2 + 213\,ns + t_3 \tag{3.13}$$

$$t_{PCTrig\,1} = t_0 + t_{PD} + t_1 + t_{Amp} + 3t_{Cab} + t_2 + 126,75\,ns + t_4 + 85\,ns + t_5 \tag{3.14}$$

$$t_{Daz} = t_0 + t_{PD} + t_1 + t_{Amp} + 3t_{Cab} + t_2 + 126,75\,ns + t_4 + 85\,ns + t_6 \tag{3.15}$$

$$\begin{aligned} t_{DazCry} &= t_0 + t_{PD} + t_1 + t_{Amp} + 3t_{Cab} + t_2 \\ &\quad + 126,75\,ns + t_4 + 85\,ns + t_6 + > 100\,ms + t_7 \end{aligned} \tag{3.16}$$

$$\begin{aligned} t_{FL} &= t_0 + t_{PD} + t_1 + t_{Amp} + 3t_{Cab} + t_2 + 126,75\,ns + t_4 \\ &\quad + 85ns + t_8 + < 10\,\mu s \end{aligned} \tag{3.17}$$

$$\begin{aligned} t_{QS} &= t_0 + t_{PD} + t_1 + t_{Amp} + 3t_{Cab} + t_2 \\ &\quad + 126,75\,ns + t_4 + 85ns + t_9 \pm 500\,ns \end{aligned}. \tag{3.18}$$

Here, t_{PD}, t_{Amp}, t_{PCD}, $t_{PCTrig1}$, $t_{PCTrig2}$, t_{Daz}, t_{DAZCry}, t_{FL} and t_{QS} are the photodiode, Stanford Amplifier, Pockels Cell Driver In, Pockels Cell Trig 1, Pockels Cell Trig 2, Dazzler In, Dazzler Crystal, CFR 400 flashlamp IN and CFR 400 q-switch IN delay times respectively. Besides, t_0 is the time that the light beam traverses the path from the beam splitter to the photodiode and;

$$t_{Cab} = t_1 = t_2 = t_3 = t_4 = t_5 = t_6 = t_7 = 4 \text{ ns} \tag{3.19}$$

and

$$t_8 = t_9 = 8 \text{ ns.} \tag{3.20}$$

Thus;

$$t_{PCD} = t_0 + t_{PD} + t_1 + t_{Amp} + 3t_{Cab} + t_2 = t_0 + t_{PD} + 28{,}1 \text{ ns} \tag{3.21}$$

$$\begin{aligned} t_{PCTrig\ 2} &= t_0 + t_{PD} + t_1 + t_{Amp} + 3t_{Cab} + t_2 \\ &\quad + 213 \text{ ns} + t_3 = t_0 + t_{PD} + 245{,}1 \text{ ns} \end{aligned} \tag{3.22}$$

$$\begin{aligned} t_{PCTrig\ 1} &= t_0 + t_{PD} + t_1 + t_{Amp} + 3t_{Cab} \\ &\quad + t_2 + 126{,}75 \text{ ns} + t_4 + 85 \text{ ns} + t_5 \\ &= t_0 + t_{PD} + 247{,}85 \text{ ns} \end{aligned} \tag{3.23}$$

$$\begin{aligned} t_{Daz} &= t_0 + t_{PD} + t_1 + t_{Amp} + 3t_{Cab} + t_2 + 126{,}75 \text{ ns} + t_4 + 85 \text{ ns} + t_6 \\ &= t_0 + t_{PD} + 247{,}85 \text{ ns} \end{aligned} \tag{3.24}$$

$$\begin{aligned} t_{DazCry} &= t_0 + t_{PD} + t_1 + t_{Amp} + 3t_{Cab} + t_2 \\ &\quad + 126{,}75 \text{ ns} + t_4 + 85 \text{ ns} + t_6 + > 100 \text{ ms} + t_7 \\ &= t_0 + t_{PD} + 251{,}85 \text{ ns} + > 100 \text{ ms} \end{aligned} \tag{3.25}$$

$$\begin{aligned} t_{FL} &= t_0 + t_{PD} + t_1 + t_{Amp} + 3t_{Cab} + t_2 + 126{,}75 \text{ ns} + t_4 + 85 \text{ ns} + t_8 + < 10 \text{ μs} \\ &= t_0 + t_{PD} + 251{,}85 \text{ ns} + < 10 \text{ μs} \end{aligned} \tag{3.26}$$

$$\begin{aligned} t_{QS} &= t_0 + t_{PD} + t_1 + t_{Amp} + 3t_{Cab} + t_2 + 126{,}75 \text{ ns} \\ &\quad + t_4 + 85 \text{ ns} + t_9 \pm 500 \text{ ns} \\ &= t_0 + t_{PD} + 251{,}85 \text{ ns} \pm 500 \text{ ns} \end{aligned} \tag{3.27}$$
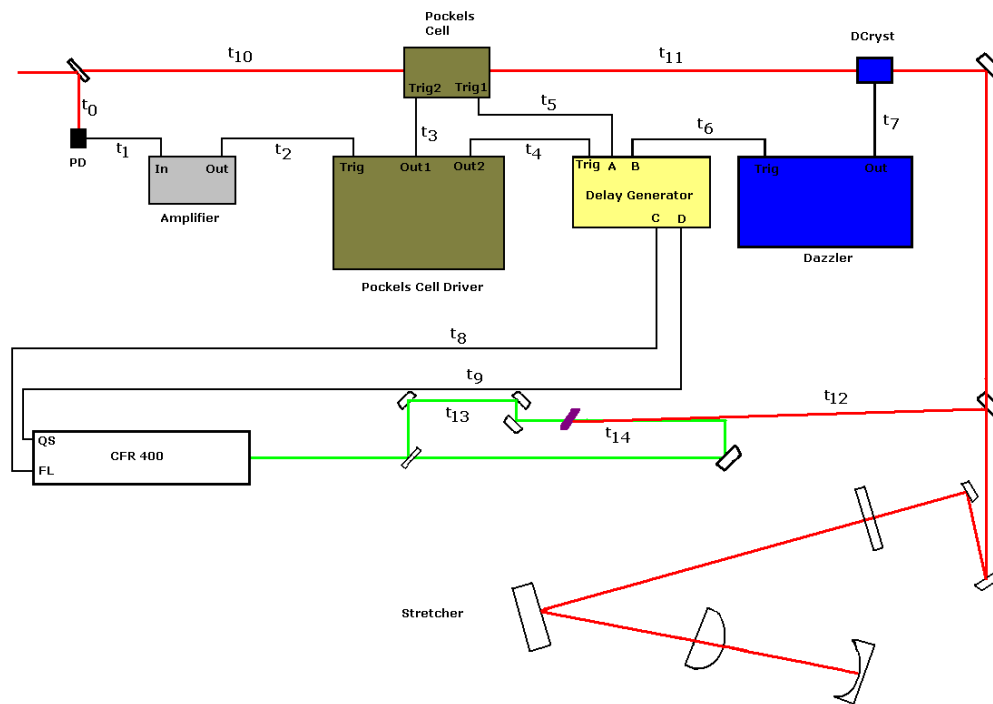
Figure 3.7 Timing issue in Ti:Sapphire system. Red lines designate the path that the laser light coming from the femtosecond oscillator traverses, black lines designate the electrical cables and green lines designate the path that laser light coming from the Nd:YAG laser traverses. As for PD, DCryst, FL and QS, they are the abbreviations of photodiode, Dazzler crystal, flashlamp and q-switch respectively.
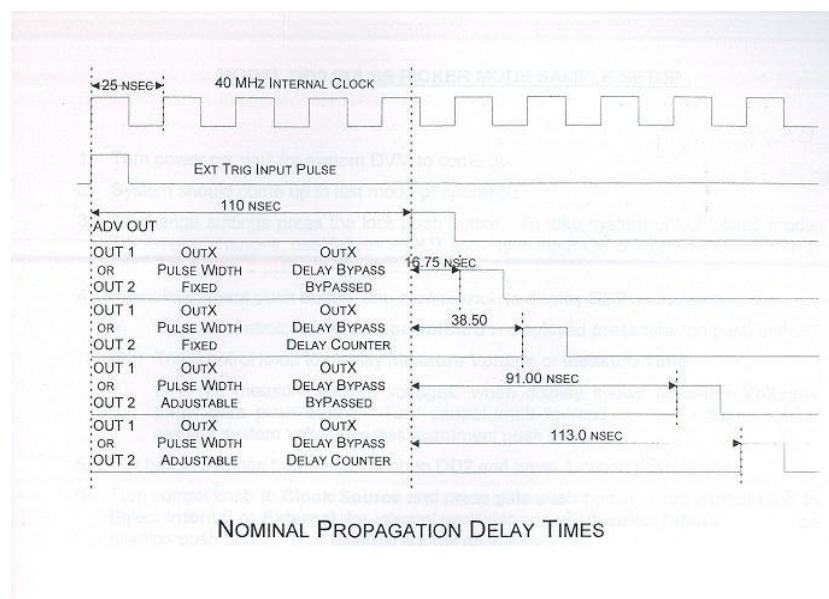
Figure 3.8 Pockels Cell delay times [76].

60

The first issue in here is to reduce the 75 MHz repetition rate to 10 Hz. When the frequency divider in the Pockels Cell driver divides the pulses coming from the oscillator to 7491000, it has been seen that the output is 10,000 which means that division to 10 Hz can be achieved with an accuracy up to 3 digits after the decimal point. As from the delay times that are obtained theoretically, it can be seen that the longest delay time comes from the dazzler and it is also a known fact that the electrical signal will traverse the same distance in a longer time than an optical one. An optical signal that is converted into an electrical one will trigger the dazzler at least in a time that is given in equation (3.25) which has a value higher than 100 ms. This in turn means that in order to electrically trigger the dazzler for the same signal, the optical path that must be traversed by the light must be a huge value. Since this is not practically possible, the system can be built if a pulse is used to trigger another pulse that is coming after the initial one. This is a valid discussion for all the electronical or electrooptical components.

When the division to 7491000 is done in the Pockels Cell driver, this particular pulse will not be able to pass through the Pockels Cell since the Pockels Cell will be triggered at a later time. For this reason the Pockels Cell must be triggered such that a pulse that is coming from the oscillator at a later time will pass through the crystal. Both for this reason and also for the fact that TRIG 2 of the Pockels Cell is coming from the delay generator, a delay must be applied to TRIG 1 by the Pockels Cell driver and also to the TRIG 2 by the delay generator. As for the dazzler, delay generator will be capable of triggering the crystal for the pulse that is coming after the triggering pulse so that an appropriate delay must also be applied to it by the delay generator. Finally the pulse that is coming from the dazzler crystal can be made to pass in the appropriate time from the Ti:Sapphire crystal by applying an appropriate delay from the delay generator to the flashlamp IN and q-switch IN of CFR 400 Big Sky laser. Due to problems with Pockels Cell, the system could not be totally built so that the discussions on timing for amplification purpose had to remain in theory. Besides this, grazing incidence angle experiments for neon-like titanium and nickel-like molybdenum whose simulation results are given in Section 3.6 could not be realized.

61

3.6 Simulations

3.6.1 Grazing Incidence Pumping Simulations of Nickel-like Molybdenum X-ray Laser

Grazing incidence pumping simulations of nickel-like molybdenum x-ray laser with an emission at 18,9 nm were performed by using a modified version of the code EHYBRID and a post-processor code coupled to it. The atomic data required by the simulations were calculated by using the COWAN code [80]. Preliminary work can be found in reference [81].

The laser wavelength of irradiation was chosen as 800 nm to simulate Ti:Sapphire laser. Molybdenum target which was irradiated in the simulations had a FWHM width of $15\,\mu m$ and length of 4 mm. The prepulse energy and pulse durations were chosen as 70 mJ and 200 ps respectively with a line focus of $4\,mm \times 15\,\mu m$ ($L \times W$). As for the main pulse, initially its energy was chosen as 80 mJ and its pulse duration was chosen as 1,2 ps with a line focus of $4\,mm \times 80\,\mu m$ ($L \times W$). The parameters of simulations were initially based on the experimental works of Keenan et al [82], from which they have observed a near saturation output. The reason for such a need is based on the lack of ray tracing codes which are used to deduce whether the gain that was simulated is really experimentally observed because of the refraction effect. The differences are in the slight changes of main pulse duration, line focus width and the initially chosen delay time.

The results of peak gain for 18,9 nm emission versus grazing incidence angles between $11^o - 30^o$ for a delay time of 300 ps can be seen in Figure 3.9. The peak gain is observed at 14° with a peak gain value of 66,2 cm^{-1}.
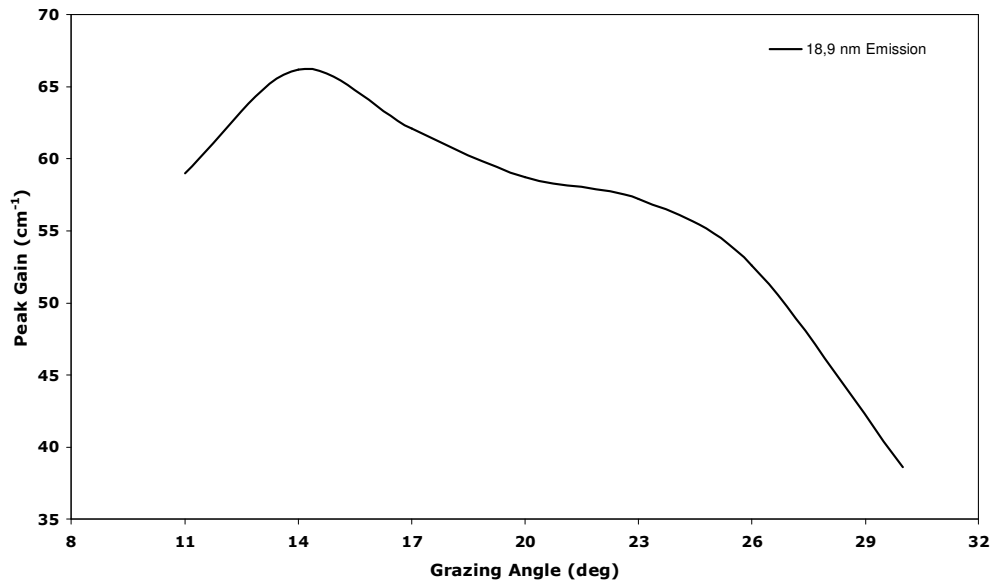
Figure 3.9. Peak Gain versus grazing incidence angle graph for 18.9 nm emission. Main pulse energy and duration are 80 mJ and 1.2 ps respectively and is separated from the prepulse of energy 70 mJ and duration of 200 ps by a delay of 300 ps. The delay between the two pulses is 300 ps.

As stated earlier, choosing a different grazing incidence angle also means that the electron density in the point of refraction changes. The critical density is equal to;

$$n_{ce} = 1,74.10^{21} \text{ cm}^{-3}.$$ (3.28)

After finding the peak gain value from a grazing incidence angle of 14°, the simulations were further performed to find the main pulse energy that would give the maximum peak gain value. The results of the simulations can be seen in Figure 3.10. From this graph it is seen that the peak gain value attains a saturation at an energy of 150 mJ with a peak gain value of 75,5 cm^{-1}.
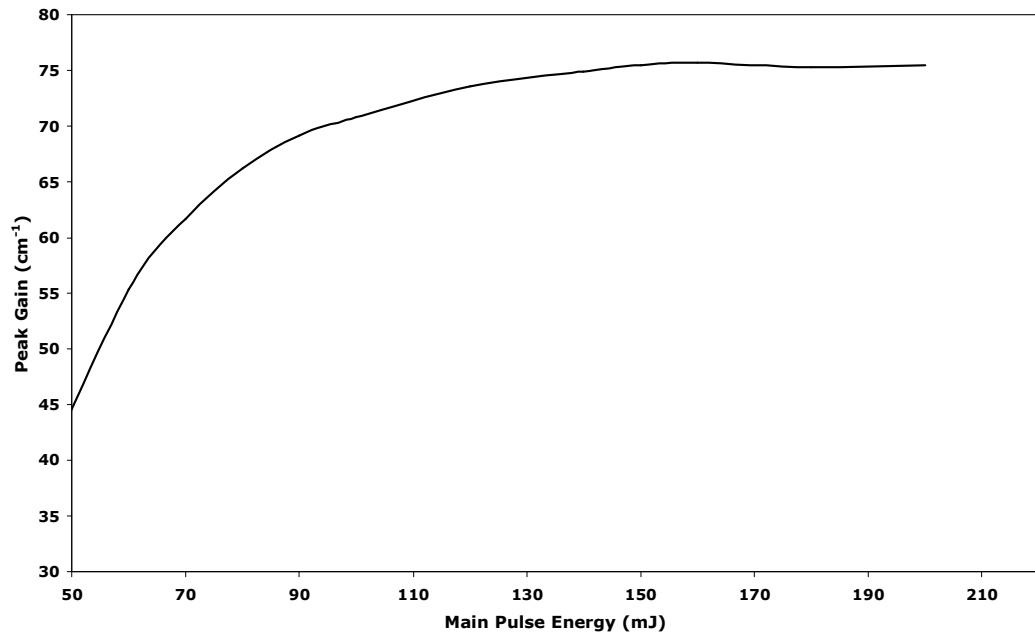
Figure 3.10 Peak gain versus main pulse energy graph for a prepulse energy of 70 mJ and duration of 200 ps and a grazing incidence angle of 14° with a delay of 300 ps. Main pulse has a pulse duration of 1,2 ps.

In order to find whether the prepulse energy is the energy that gives the maximum peak gain, peak gain values were obtained for prepulse energies between 20 – 100 mJ. The results of the EHYBRID simulations can be seen in Figure 3.11.
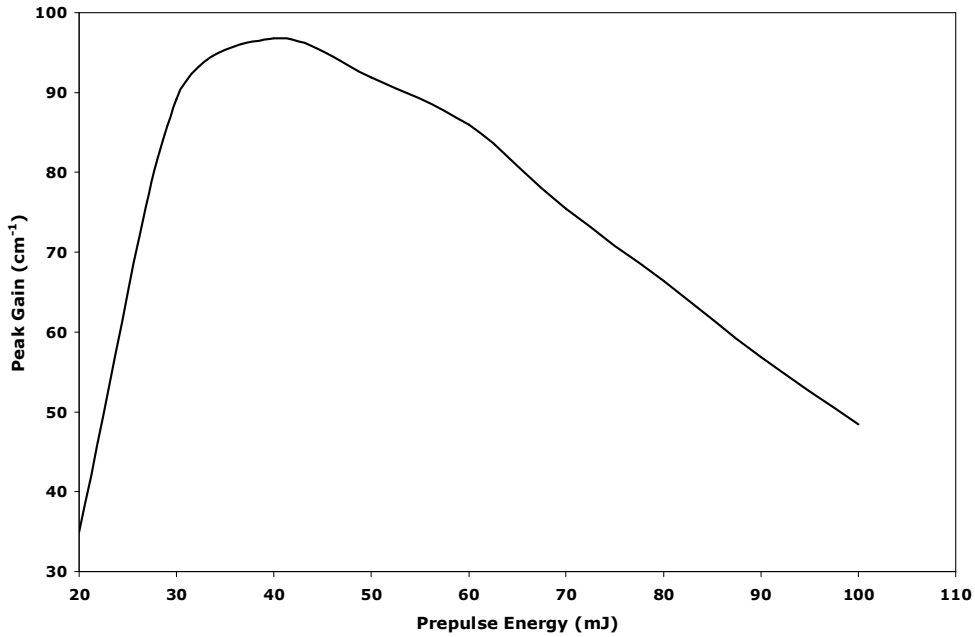
Figure 3.11 Peak gain versus prepulse energy for a main pulse energy of 150 mJ and pulse duration of 1,2 s and a grazing incidence angle of 14°. Prepulse has a pulse duration of 200 ps. The two pulses are separated by a delay time of 300 ps.

The graph shows that the peak gain is attained at a prepulse energy of 40 mJ with a value of 96,8 cm^{-1}. However if we look at the electron density versus prepulse energy graph that is shown in Figure 3.12, it can be seen that this value is actually coming from an electron density region of 3.10^{20} cm^{-3} which is too high to actually obtain such a big gain. Li et. al. [83] have obtained saturated amplification from Ni-like molybdenum coming from the region with electron density in the range $1-1,5.10^{20}$ cm^{-3}. Concerning this fact, we can say at first glance that the optimum prepulse energy is between 70 – 90 mJ. The electron density at 80 mJ is $1,27.10^{20}$ cm^{-3} and at 90 mJ is $1,26.10^{20}$ cm^{-3}. However, peak gain values are 66,4 and 56,9 cm^{-1} for 80 and 90 mJ respectively. Thus among 80 and 90 mJ prepulse energies, 80 mJ prepulse energy gives the optimum condition.

65
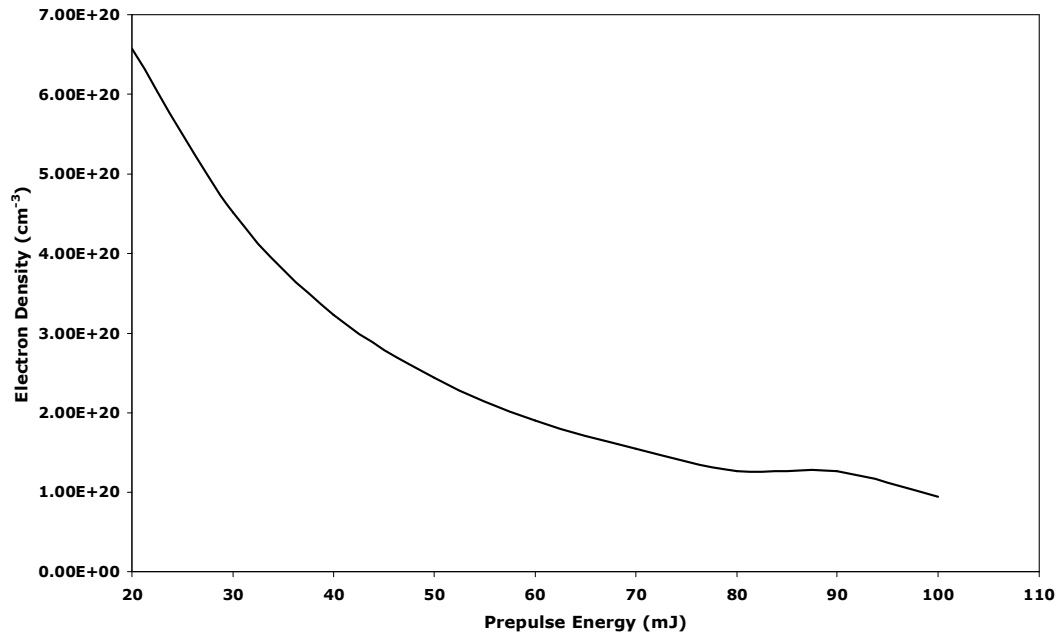
Figure 3.12 Electron density versus prepulse energy for a main pulse energy of 150 mJ and pulse duration of 1,2 ps and a grazing incidence angle of 14°. The pulse duration of the prepulse is 200 ps. The delay between the prepulse and the main pulse is 300 ps.

For 70 mJ of prepulse energy with a pulse duration of 200 ps, the optimum conditions have all been found from the simulations i.e. maximum peak gain value is attained when the main pulse with a pulse duration of 1,2 ps has an energy of 150 mJ and the grazing incidence angle is 14°. Electron density versus time, electron temperature versus time and ionization versus time graphs for a prepulse energy of 70 mJ and pulse duration of 200 ps, main pulse energy of 150 mJ and pulse duration of 1,2 ps and grazing incidence angle of 14° are seen in Figure 3.13, Figure 3.14 and Figure 3.15 respectively. The electron density at the peak gain time is $1,55.10^{20}$ cm^{-3}, electron temperature at the peak gain time is 568 eV and ionization at the peak gain time is 13,7.
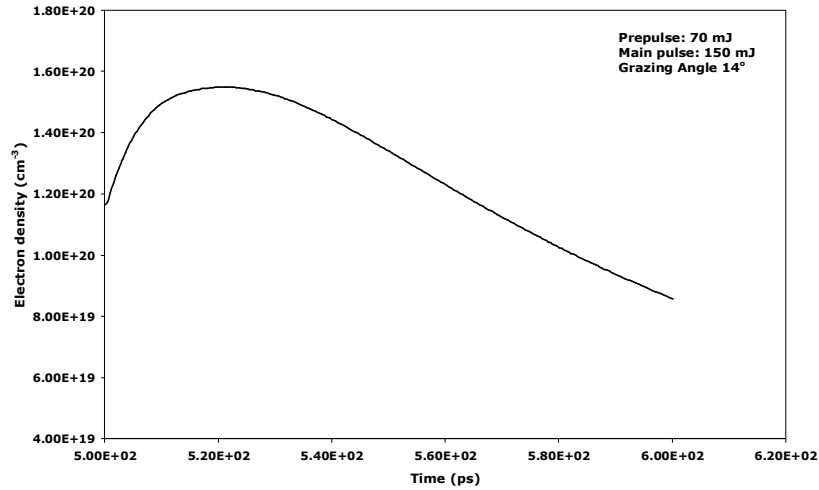
Figure 3.13 Electron density versus time graph for a prepulse energy of 70 mJ and pulse duration of 200 ps, main pulse energy of 150 mJ and pulse duration of 1,2 ps and grazing incidence angle of 14°. Electron density at the peak gain time is around $1,55.10^{20}$ cm^{-3}. The delay between the prepulse and the main pulse is 300 ps.
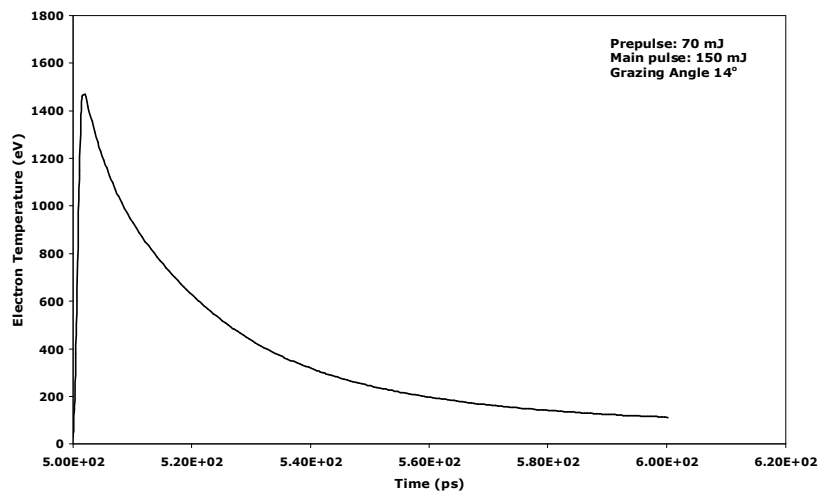
Figure 3.14 Electron temperature versus time graph for a prepulse energy of 70 mJ and pulse duration of 200 ps, main pulse energy of 150 mJ and pulse duration of 1,2 ps and grazing incidence angle of 14°. The delay time between the prepulse and the main pulse is 300 ps. Electron temperature corresponding to the peak time is around 568 eV.

67
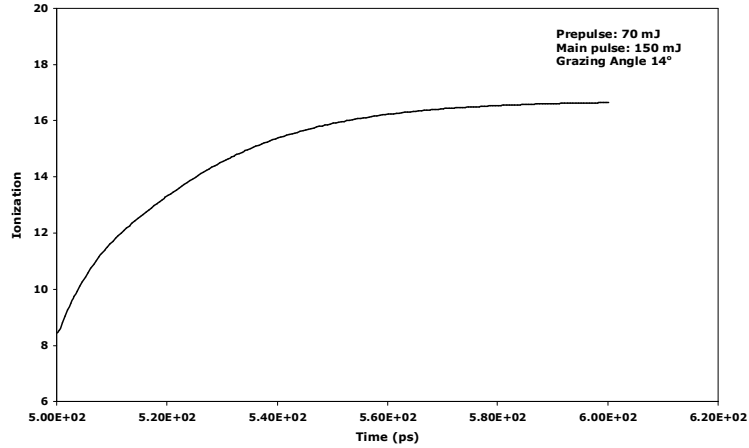
Figure 3.15 Ionization versus time graph for a prepulse energy of 70 mJ and pulse duration of 200 ps, main pulse energy of 150 mJ and pulse duration of 1,2 ps. The delay between the two pulses and the grazing incidence angle are 300 ps and 14° respectively. At the time of peak gain, ionization is 13,7.

As for the gain versus time graph of 70 mJ prepulse, 150 mJ main pulse with pulse durations of 200 ps and 1,2 ps respectively and 14° of grazing incidence angle, it can be seen in Figure 3.16. FWHM is 23 ps.
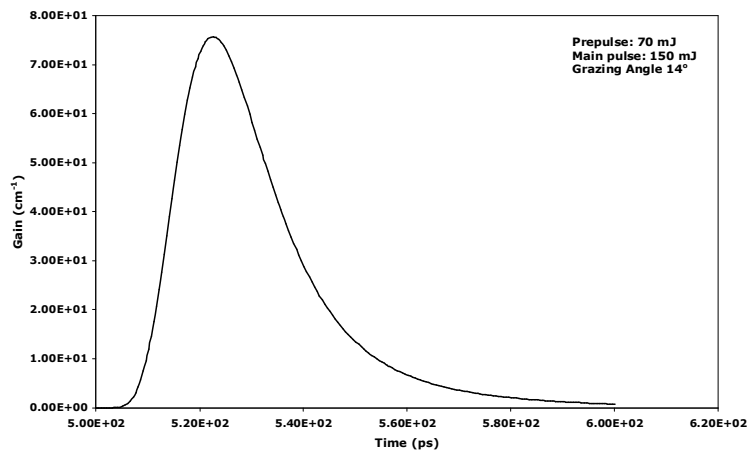
Figure 3.16 Gain versus time graph for a prepulse energy of 70 mJ and pulse duration of 200 ps, main pulse energy of 150 mJ and pulse duration of 1,2 ps and grazing incidence angle of 14°. The two pulses are separated by a delay time of 300 ps. Peak gain is 75,6 cm^{-1} and FWHM is 23 ps.

68

As for the 80 mJ prepulse energy case, simulations were performed to find the optimum peak gain versus grazing incidence angle. The results of the simulations can be seen in Figure 3.17.
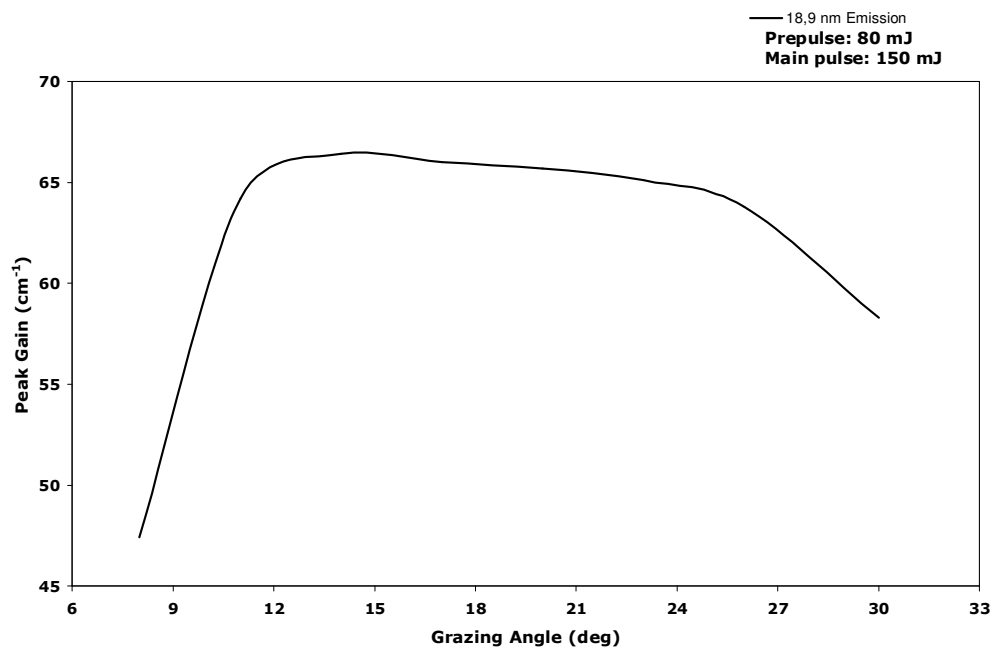
Figure 3.17 Peak gain versus grazing incidence angle for a prepulse energy of 80 mJ and pulse duration of 200 ps, main pulse energy of 150 mJ and pulse duration of 1,2 ps and delay time of 300 ps. Peak gain is obtained for a grazing incidence angle of 14° with a value of 66,4 cm^{-1}. Electron density is around $1,28.10^{20}$ cm^{-3}.

Figure 3.17 shows that although the peak gain values are close to each other in between $14° - 23°$, the peak gain is still obtained at the angle of $14°$ with a value of 66,4 cm^{-1}. Thus, further simulations were further performed to find the optimum main pulse energy. The results of these simulations can be seen in Figure 3.18.
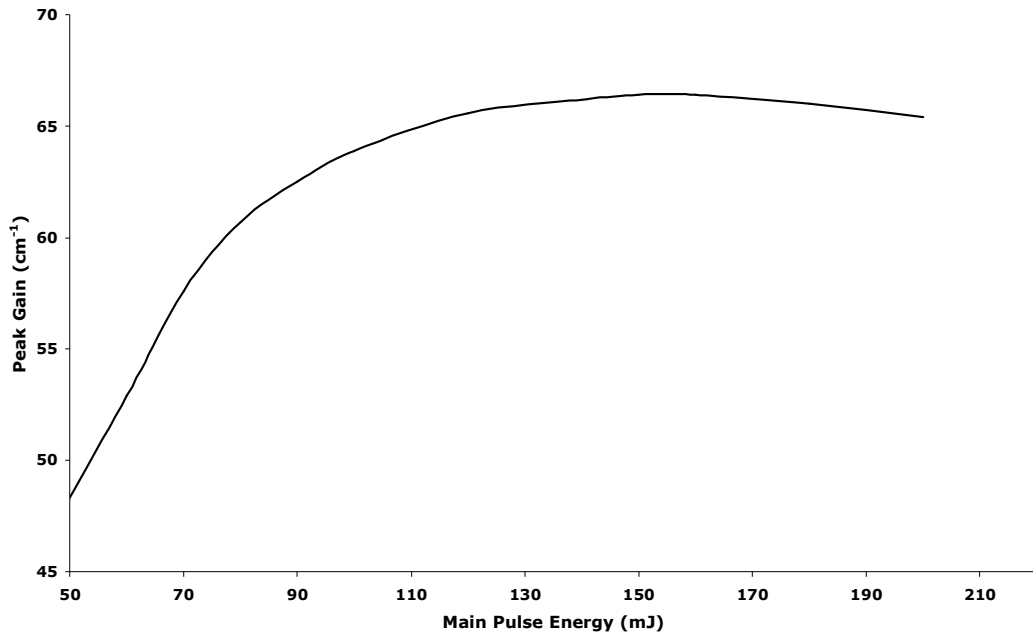
Figure 3.18 Peak gain versus main pulse energy for a prepulse energy of 80 mJ and duration of 200 ps for a grazing incidence angle of 14°. The main pulse has a pulse duration of 1,2 ps and the two pulses are separated by a delay time of 300 ps.

From this figure it is seen that saturation is obtained around 150 mJ for a prepulse energy of 80 mJ. Thus, both 70 and 80 mJ prepulse energies yield optimum results at a grazing incidence angle of 14° and main pulse energy of 150 mJ. To conclude, electron density versus time, electron temperature versus time and ionization versus time graphs of 80 mJ prepulse energy with a 150 mJ of main pulse energy and grazing incidence angle 14° can be seen in Figures 3.19, 3.20 and 3.21 respectively. The pulse durations are 20 ps for the prepulse and 1,2 ps for the main pulse.
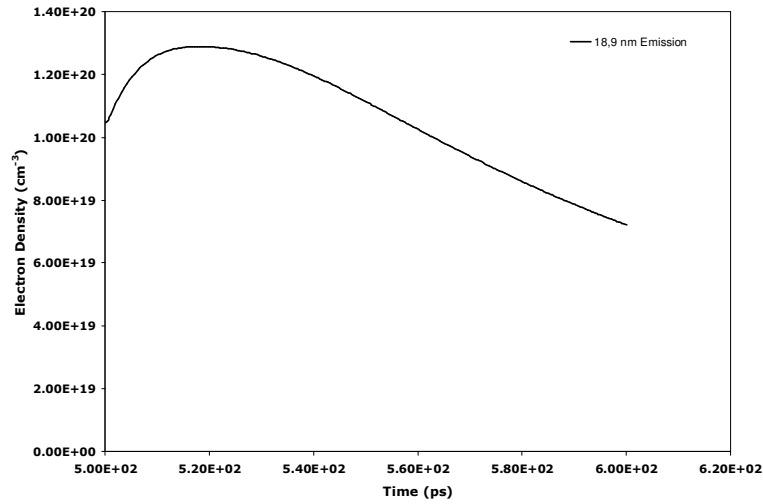
Figure 3. 19 Electron density versus time for a prepulse energy of 80 mJ with duration 200 ps and main pulse energy of 150 mJ with pulse duration 1,2 ps. The grazing incidence angle is 14° and the delay time is 300 ps. Peak gain is obtained at an electron density of $1,27.10^{20}$ cm^{-3}.
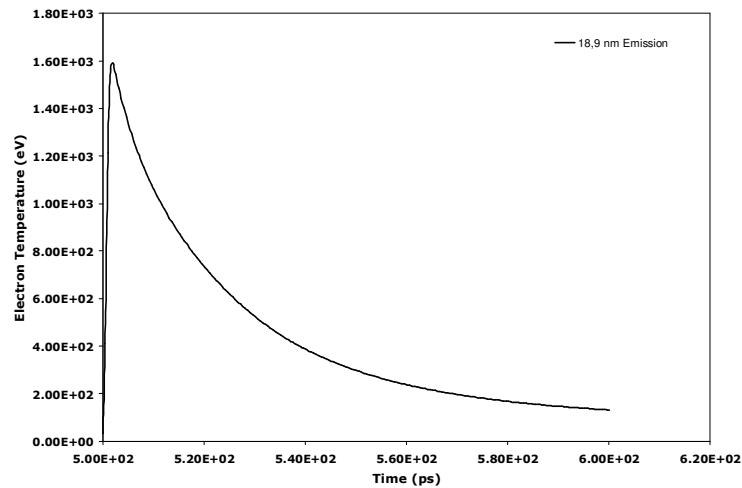
Figure 3.20 Electron temperature versus time graph. The prepulse energy is 80 mJ with duration 200 ps and main pulse energy is 150 mJ with pulse duration 1,2 ps. The two pulses are separated by a delay time of 300 ps and the grazing incidence angle is 14° . Electron temperature at the time of peak gain is 597 eV.

71
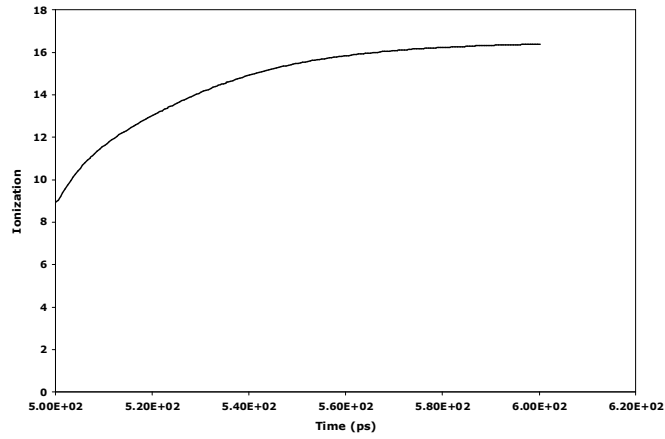
Figure 3.21 Ionization versus time graph. The prepulse energy and main pulse energies are 80 mJ and 150 mJ respectively with pulse durations of 200 ps and 1,2 ps. The pulses are separated by a delay time of 300 ps and the grazing incidence angle is 14°. Ionization at the time of peak gain is 13,6.

Finally, gain versus time graph can be seen in Figure 3.22. The FWHM is calculated as 29 ps.
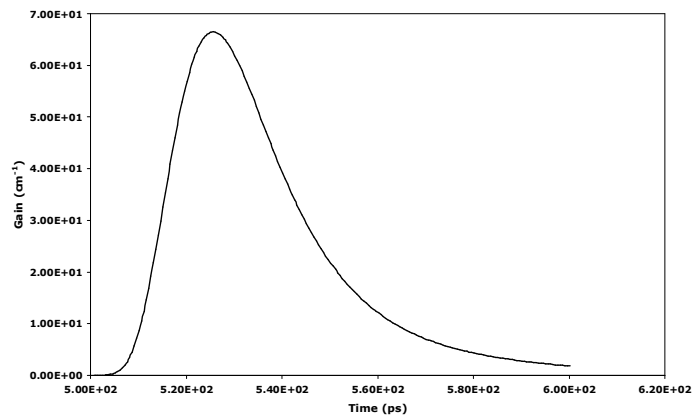
Figure 3.22 Gain versus time graph of the emission at 18,9 nm. The prepulse energy and main pulse energies are 80 mJ and 150 mJ respectively with pulse durations of 200 ps and 1,2 ps. Grazing incidence angle is 14° and the delay time is 300 ps. FWHM is 29 ps.

72

3.6.2 Grazing Incidence Pumping Simulations of Neon-like Titanium X-ray Laser

Simulations were performed by using a modified version of the code EHYBRID which makes use of the atomic data calculated by using the COWAN code [80] and a post-processor code coupled to it. Simulations are for the emission of neon-like titanium at 32,6 nm. Preliminary work can be found in reference [84].

Initially, the prepulse energy was set to 70 mJ with a pulse duration of 200 ps and main pulse energy was set to 80 mJ with a duration of 1,2 ps. The prepulse was focused to $4\,\text{mm} \times 15\,\mu\text{m}$ and the main pulse was focused to $4\,\text{mm} \times 30\,\mu\text{m}$ and initially they were separated by a delay time of 300 ps. Simulations were firstly performed to find the optimum grazing incidence angle under these pumping conditions. Figure 3.23 shows the result of these simulations.
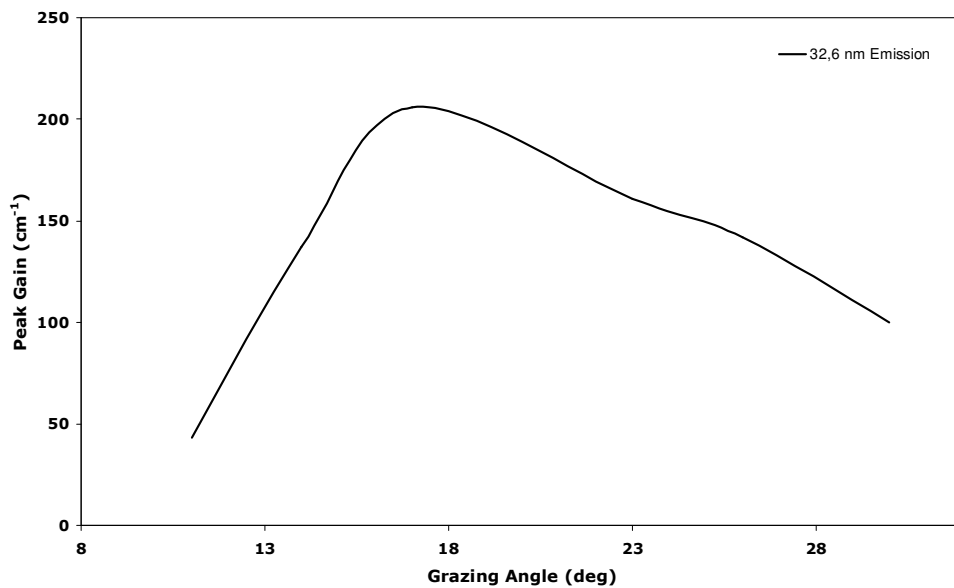
Figure 3.23 Peak gain versus grazing incidence angle graph for a prepulse energy of 70 mJ and main pulse energy of 80 mJ with pulse durations 200 ps and 1,2 ps respectively. The delay time is 300 ps.

73

Maximum emission is obtained at a grazing incidence angle of 17° with a peak gain value of 206 cm^{-1}. When the grazing incidence angle is 17°, deposition of the energy is into a region where the electron density is $1,49.10^{20}$ cm^{-3}. After finding the optimum grazing incidence angle, simulations were further performed to find the appropriate delay time. Figure 3.24 shows the simulation results.
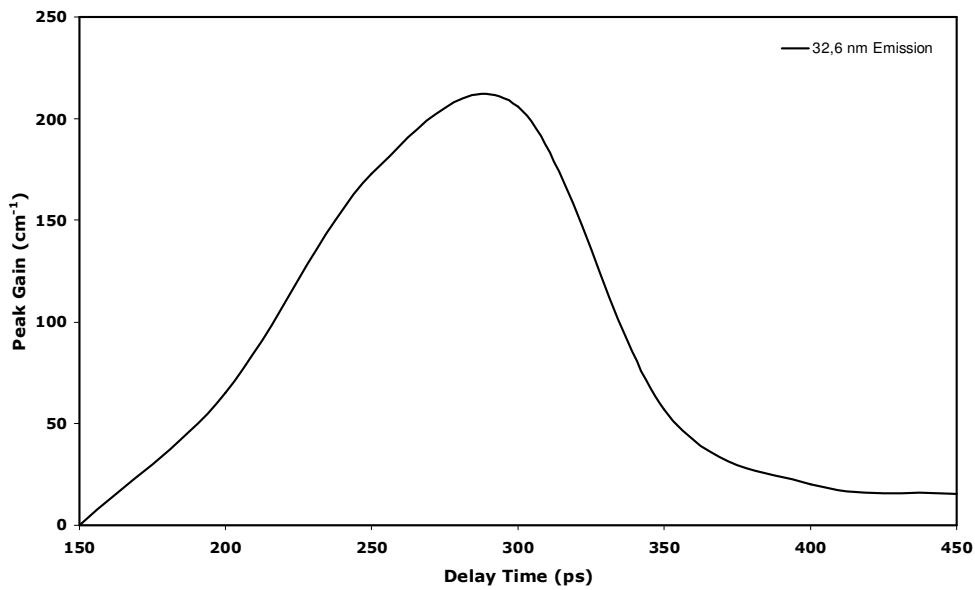
Figure 3.24 Peak gain versus delay time graph for a grazing incidence angle of 17° under the initial prepulse and main pulse conditions.

Maximum peak gain has been obtained for a delay time of 300 ps so that the maximum peak gain value is still 206 cm^{-1}. Afterwards, simulations were further performed to find the maximum peak gain as a function of prepulse energy, the results of which can be seen in Figure 3.25.
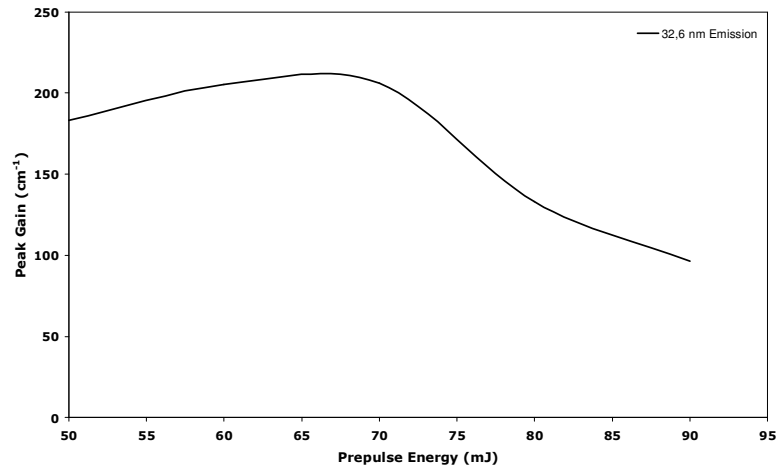
Figure 3.25 Variation of peak gain versus prepulse energy for a delay time of 300 ps and grazing incidence angle of 17°. Main pulse energy is 80 mJ and pulse duration is 1,2 ps. Pulse duration of the prepulse is 200 ps.

Figure 3.25 shows that the peak gain is maximized at a prepulse energy of 70 mJ. Finally Figure 3.26 shows the simulation results to find the maximum peak gain value under a change in the main pulse energy.
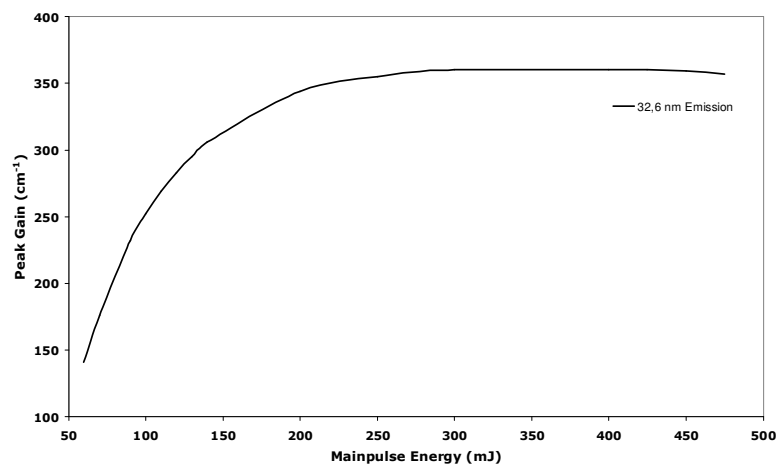
Figure 3.26 Peak gain versus main pulse energy graph for a grazing incidence angle of 17°, delay time of 300 ps and prepulse energy of 70 mJ. The pulse durations of the main pulse and the prepulse are 1,2 ps and 200 ps respectively.

As can be seen from the graph, this time the maximum peak gain value has changed and attains a value of 360 cm^{-1} around a main pulse energy of 300 mJ. Above 300 mJ, the maximum value remains constant so that a main pulse energy higher than 300 mJ is just a waste of energy. Electron temperature versus time, electron density versus time and ionization versus time graph for a prepulse energy of 70 mJ with duration 200 ps, main pulse energy of 300 mJ with duration 1,2 ps, a delay time of 300 ps and grazing incidence angle of 17° can be seen in Figures 3.27, 3.28 and 3.29 respectively.
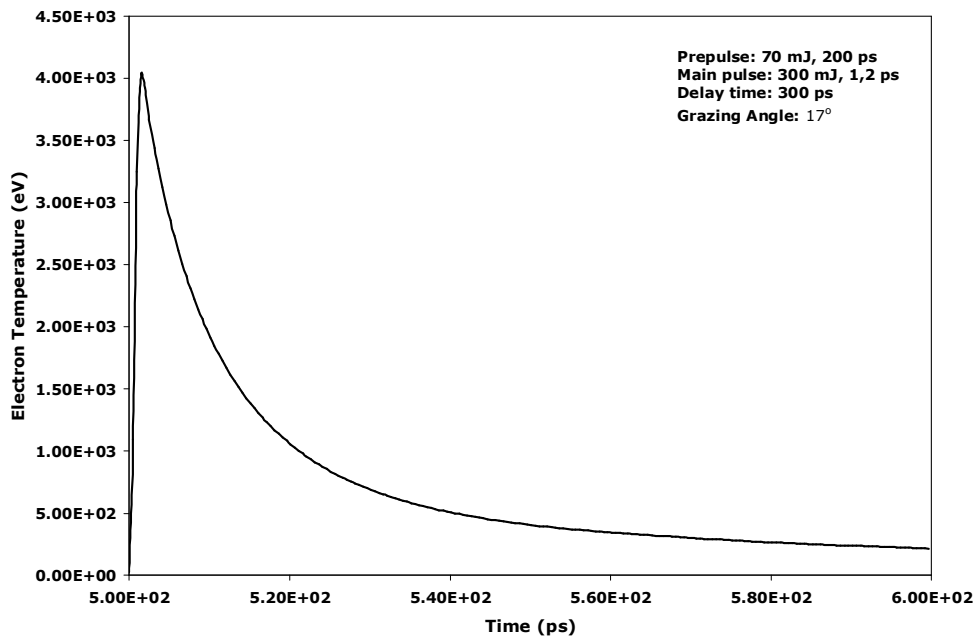
Figure 3.27 Electron temperature versus time graph.
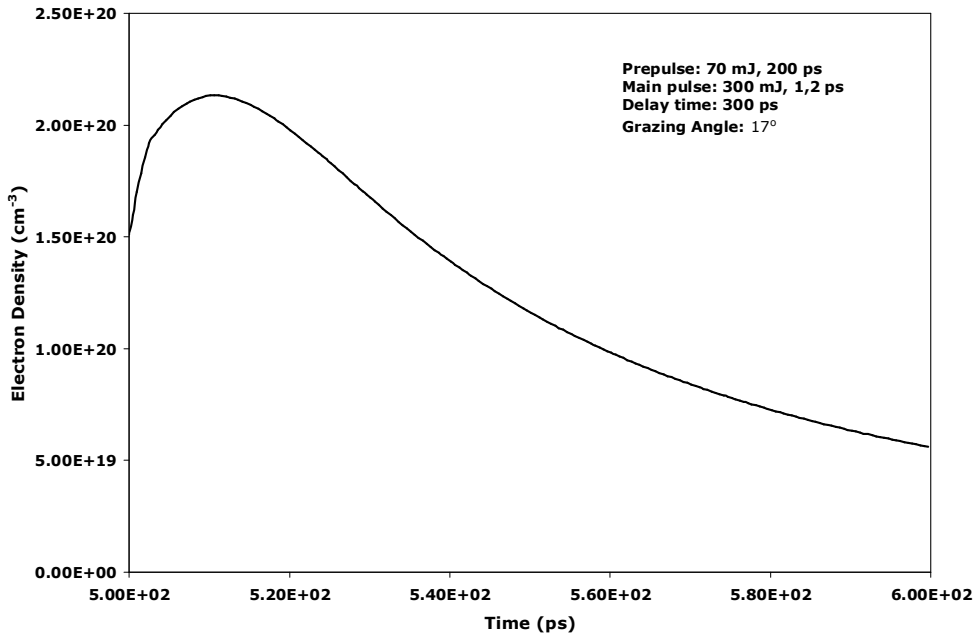
Figure 3.28 Electron density versus time graph.
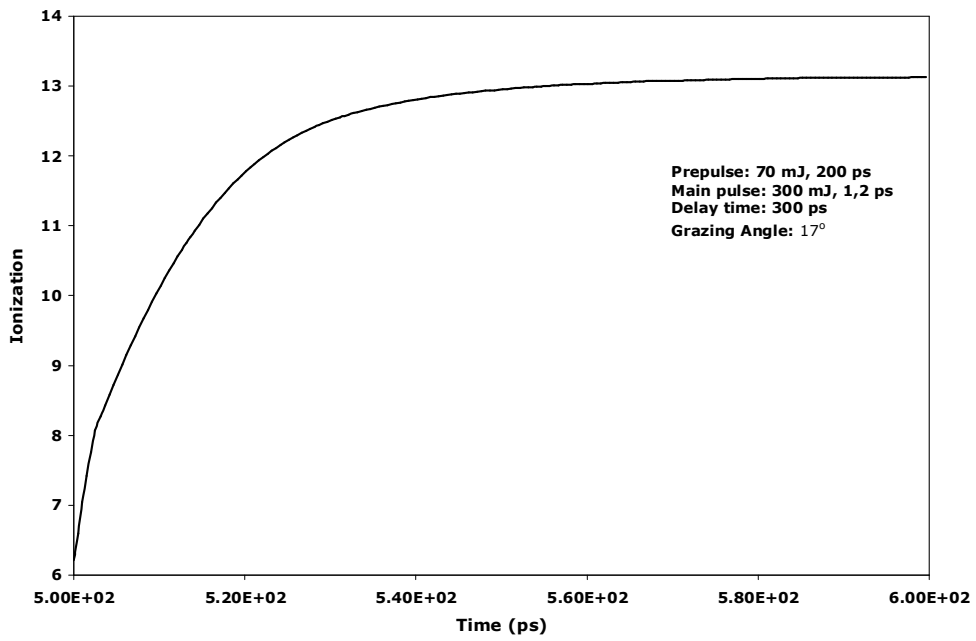
Figure 3.29 Ionization versus time graph.

From these figures we can find that at the time of peak gain electron temperature is 912 eV, electron density is $1{,}89{.}10^{20}$ cm^{-3} and ionization is 12. Figure 3.30 shows the gain versus time graph under these simulation conditions. FWHM value is 18 ps.
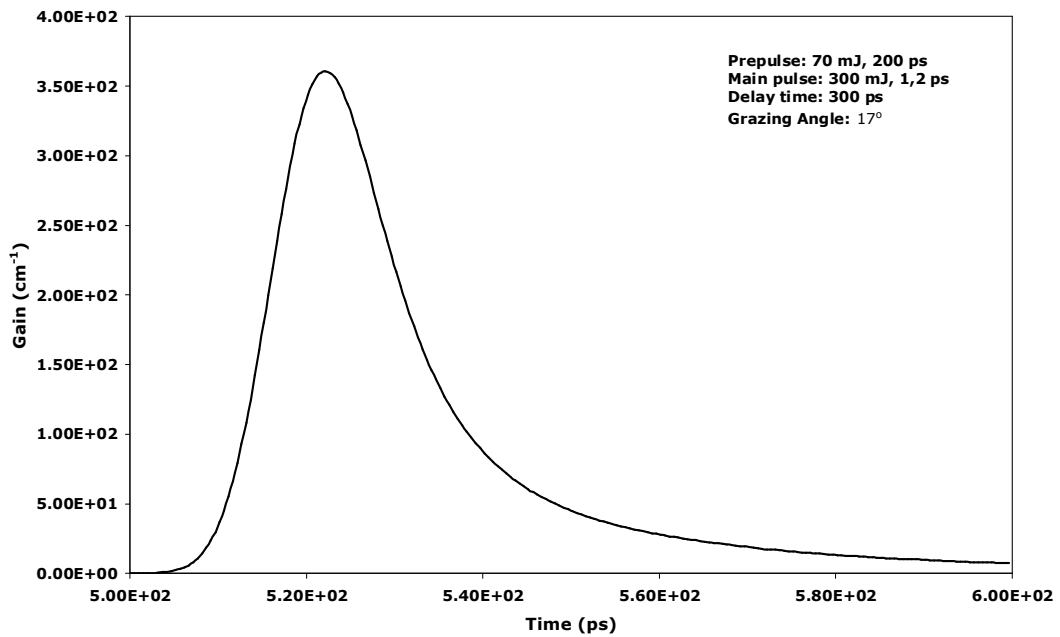
Figure 3.30 Gain versus time graph of the emission at 32,6 nm. FWHM is 18 ps.

CHAPTER 4

EUV LITHOGRAPHIC SIMULATIONS OF TIN PLASMA

4.1 Introduction

The number of transistors on a chip increases 40% every year [85]. Plotting this increase on a semi log graph gives almost a straight line that is known as Moore's law [86]. The need for such an increase comes basically from the computer industry since as the number of transistors on a computer chip increases, the processing time of the computer decreases. Because of this, microlithography techniques have been investigated in time in terms of their low cost of ownership and high productivity. As for the different kinds of microlithography techniques, optical lithography, immersion lithography, extreme ultraviolet lithography, electron beam lithography and ion beam lithography can be given. The systems that are being used in microlithography processing are more or less the same [87]. They all include an energy source, a mask or a mask set, a photoresist and procedures for pattern deficiency detection. In the electron beam lithography, an electron beam is used to illuminate the mask rather than a photon beam. Although the resolution achieved by using them is low and the depth of focus is high, processing with them is very slow and so they are not good for volume production purposes [88]. In ion beam lithography, accelerated hydrogen or helium beams which are focused with electrostatic field are used [89]. The drawback of ion lithography is that, it is very hard to produce wafers with close patterns. As for optical lithographic systems, they have been used and are still being used for volume production purposes. Immersion lithographic systems are systems in which the optical lithographic system (which actually is a dry system) is immersed in a fluid so that higher resolution is obtained in comparison with the dry case. Finally, the extreme ultraviolet lithography also has the same principle as the optical lithography.

Therefore by introducing the optical lithographic system, an understanding of the extreme ultraviolet lithographic system is also possible.

4.2 Optical Lithography

4.2.1 Optical Lithographic System Concepts in General

The layout of a typical optical lithographic system can be seen in Figure 4.1. The coherent light source of the system is used to illuminate the photo mask by the condenser system. Then the light that has passed through the openings of the mask is projected towards the wafer which is the image plane and so the image of the final pattern that is to be printed. Here photo mask is a mask that is composed of magnified patterns that are to be printed on the wafer. As for the wafer, it is covered by a photoresist material so that when the light is directed towards it, those parts of it that is illuminated undergo a chemical change. Afterwards the wafer is developed and baked so that the parts of the photoresist which are illuminated by the light are removed. Finally, those washed out parts are etched.
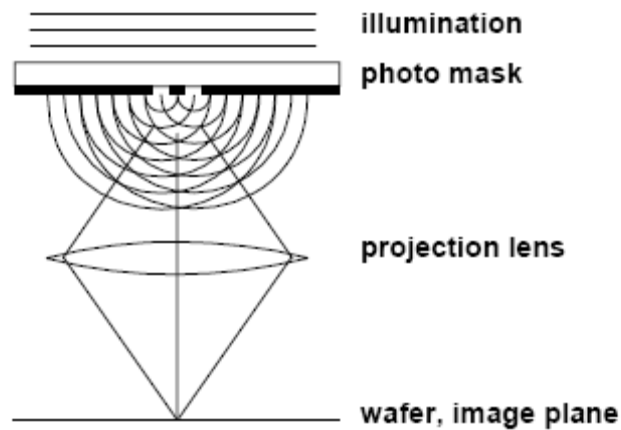
Figure 4.1 Typical optical lithographic system layout [90].

The openings of the photo mask act like individual light sources where the distance between the centres of the two openings of the photo mask (or *pitch*) is defined as say d. When the coherent light passes from them, constructive interference will occur and diffraction nodes will form at the points where the pathlength difference between the two light beams is an integer multiple of the wavelength of the laser for any light angle θ ;

$$\sin \theta = m \frac{\lambda}{d} \qquad m = 0, \pm 1, \pm 2, \ldots \tag{4.1}$$

The 0th order diffraction contains no spatial information since it traverses the path along the centre of the optical axis of the system. Thus the diffraction order should be at least 1 (i.e. $m = \pm 1$). "*Numerical Aperture*" of the projection system is defined as the maximum angle of diffraction. From Fig. 4.1 for the case of a single projection lens, this corresponds to the sine of the maximum angle that the light rays coming out of the photo mask openings can make to the end of the projection lens. Thus for the first order of diffraction with m=+1;

$$d \sin \theta = d.NA = \lambda . \tag{4.2}$$

Also it is worth to note that since numerical aperture is the sine of an angle, the maximum value that it can attain is 1.

The minimum feature size or the "*Resolution*" can be defined as the minimum feature size that can be printed within the quality limits;

$$R = \frac{d}{k_1} \tag{4.3}$$

so that the Rayleigh equation which defines the minimum feature size that can be printed can be found as;

$$R = k_1 \frac{\lambda}{NA} \tag{4.4}$$

where k_1 is called the Rayleigh factor, which is an empirical factor that depends on the resist properties, illumination properties of the condenser and the technique that is used for the mask resolution enhancement [91]. This resolution limit of optical lithography was defined by Wilczynski in IBM [88].

There is also another important concept in optical lithography, i.e. the "*Depth of Focus*". Depth of focus can be defined as the range of focus at which the profile of the printed pattern on the wafer does not change. This can be found by using the geometry seen in Figure 4.2.
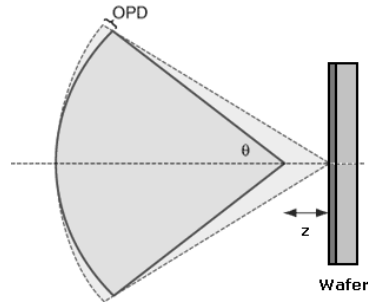
Figure 4.2 The 0th and 1st order diffracted lights that are out of focus by a distance z [92].

The effect of defocusing can be found by causing an error in the curvature of the wavefront of the light that is coming from the openings with respect to the desired wavefront. As expected, this error in the curvature will increase as one goes from the centre to the edge of the wavefront. The difference between these two wavefront curvatures at the edge are called "*Optical Path Difference*". OPD and can be found as;

$$OPD = z - z\cos\theta = z(1 - \cos\theta) = z\sqrt{1 - \sin^2\theta} \approx \frac{1}{2}z\sin^2\theta . \qquad (4.5)$$

The 0th and 1st order diffracted lights will be $\pi/2$ out of phase when the OPD is equal to the quarter of the wavelength i.e. $OPD = \lambda/4$. But in this case since there will be no interference between the 0th and 1st orders, there will not be any patterns formed. For this reason, the OPD of the system must be smaller than this amount, i.e.;

$$OPD = k_2 \frac{\lambda}{4}, \quad k_2 < 1 . \qquad (4.6)$$

This is called "*Rayleigh's Criteria*". The Depth of Focus can be found as;

$$DOP = 2z_{max} = k_2 \frac{\lambda}{\sin^2\theta} = k_2 \frac{\lambda}{NA^2} . \qquad (4.7)$$

Theoretically there is another important parameter for optical lithography, i.e. the pattern density. The pattern density is limited by the minimum pitch size that can be printed as;

$$p_{min} = k_{p,min} \frac{\lambda}{NA} = 0.5 \frac{\lambda}{NA} \qquad (4.8)$$

so that there is a $k_{p,min}=0.5$ limiting factor that determines the pitch periodicity on the printed pattern.

In order to minimize the printed feature sizes, the resolution R must be reduced by either reducing k_1 or λ or by increasing the numerical aperture NA. Increasing NA from some point does not seem feasible because as it increases, so does the aberrations and also it is hard to manufacture such great sized lenses. Apart from that, the depth of focus is inversely dependent on the square of NA which means that as NA increases, the depth of focus decreases. This is not a wanted situation since decreasing the depth of focus leads to rapid divergence of the focused beam and so a need for a better focusing ability.

The constants k_1 and k_2 depend on the resist material, process technology and image formation technique [87]. There is no theoretical limit coming from the pattern dimension (or resolution) and so that there is no limit for the reduction of k_1. Thus it is possible to reduce the resolution without reducing the pattern density on a chip. But as k_1 value reduces below 0.75, the image quality reduces noticeably [85]. For this reason in order to decrease k_1 without degrading the image quality, techniques called "*Resolution Enhancement Techniques*" (RET) like attenuated phase-shifted mask lithography, alternating phase-shifted mask lithography, off-axis illumination and optical proximity correction have been used [85, 90]. In the attenuated phase-shifted lithography, a small amount of light is allowed to pass through the parts of the photo mask that should normally be opaque. The photo masks are aligned so that when light illuminates the mask, the phase difference between the clear region and the opaque region becomes π and as a result, destructive interference takes place causing the edges of the shapes to be prominent. On the other hand in the optical proximity correction, the mask shapes are distorted in order to form better known shapes. This necessity comes from the fact that images are distorted from their original when k_1 value is low. These distortions may be in terms of line shortening, corner rounding etc. Thus, these distortions are compensated for example by line lengthening, biasing and so on. As for the alternating phase-shifted mask lithography and the off-axis illumination, they both make use of the fact that if the distance between the two neighbouring openings are equal to $\lambda/2$, firstly since the two light rays are out of phase there will not be any constructive interference at the central axis of the projection lens so that there will not be

depth of focus limitations. Secondly, the first constructive interference will occur at an angle that is closer to the central axis so that the resolution will be;

$$R = 0.25 \frac{\lambda}{NA} \qquad (4.9)$$

i.e. k_1 would acquire a smaller value. In the alternating phase-shifted mask lithography, the mask topography is changed whereas in the off-axis illumination lithography, the illumination angle is changed to achieve this result.

Up to now by using these processes, k_1 values as low as 0.5 and NA values as high as 0.8 have been achieved but the enhancement of this technology by reducing k_1 or by increasing NA does not seem to give more reduction in the resolution [93]. Thus further improvement in the lithography process requires a decrease in the laser wavelength that is being used.

While looking for a light source with a smaller wavelength, some points must be kept in mind [85]. Firstly, the light source must at the same time be able to give sufficient output power. Secondly, it is known that atmosphere attenuates light rays below 193 nm. For this reason below this wavelength limit, work on an environment that is free of oxygen and water is required. Thirdly as the wavelength changes, so does the system components. For example in order to make adequate lenses for this new wavelength range, new optical materials must be searched for. Finally, the development process of photoresist changes.

4.2.2 Lithographic Systems Used for Volume Production

The lithographic systems that are currently being used for mass production make use of excimer lasers with a wavelength of 248 nm or 193 nm. Table 4.1 below [94] shows the progress of optical lithography from 1993 to 2007. It can be seen from the table that NA has increased in time and exceeded 1.0 and k_1 factor has decreased in time. Thus, there is a need to decrease the wavelength of the source that is being used in the system in order to enhance the resolution.

Table 4.1 Progress of wavelength, lens NA, resolution, k_1 factor from 1993 to 2007 in the industry [94].

Year	Wavelength	Lens NA	Resolution	k_1 factor
1993	365 nm lamp	0,57	450 nm	0,70
1993	250 nm lamp	0,50	250 nm	0,51
1997	248 nm laser	0,60	200 nm	0,49
2004	193 nm laser	0,85	82 nm	0,37
2005	193 nm laser	0,92	65 nm	0,31
2007	193 nm laser	1,30	45 nm	0,30
2007	13.5 nm	0,25	25 nm	0,46

4.3 Extreme Ultraviolet Lithography

Extreme Ultraviolet Lithography is considered as a strong candidate to realize conventional optical lithography in the coming years. The reason for this is that the 13.5 nm wavelength would allow the printing of structures of sizes less than 100 nm [95] and by 2009, printable patterns of 32 nm half-pitch will be required by the computer industry.

There are various sources that are being used as a source for EUVL system like synchrotron radiation, discharge produced plasmas (DPP) and laser produced plasmas (LPP) among which DPP and LPP make use of the plasma medium to produce EUV light. In DPP, plasma is produced by applying electrical discharge to a gas like xenon whereas in LPP, plasma is produced by irradiating a target material with laser light. Synchrotron radiation is a very complex and a costly system so that it does not seem practical to use it as a source for EUVL. As for DPP, it has some disadvantages some of which can be given as follows [96]: Firstly there is a need for debris mitigation due to the production of debris between the electrodes and so debris mitigation filters have to be used. Besides, the peripheral is heated excessively so that spectral filters have to be used in the system. On the other hand LPP has advantages over DPP in terms of power scalability, spatial stability, dimensional flexibility, minimal heat load and large

solid angle of collection [95]. Also the conversion efficiency of the in-band radiation emission from a DPP is smaller in comparison with the LPP [97]. Thus among them, LPP seems to be the strongest candidate for realizing an EUVL system.

An EUVL system is compromised of a source, a collector system, illuminator optics, a mask, projection optics and a photoresist material. The collector system collects the radiation that is emitted from the plasma and the illuminator optics shapes and transfers this light to the mask. After that, the pattern on the mask is printed on the photoresist material by the projection optics. Typically, laser light source that is used to irradiate the target has a 1 J of laser energy with a 10 ns of pulse duration and a focal spot size of 100 μm [98], so that an Nd:YAG laser is a very suitable laser light source for this application.

4.3.1 EUVL Optics and Conversion Efficiency

All materials absorb light of wavelength below 100 nm. This means that below 100 nm laser light irradiation, lenses cannot be used since at that wavelength range the light cannot penetrate the lenses. As a result, only the mirrors and the Fresnel zone plates from which the transmitted waves undergo constructive interference at the focal point can be used in EUVL systems [99].

EUVL systems make use of Mo/Si or Mo/Be coated mirrors. Mo/Si coated mirrors have a peak reflectivity at around 13.5 nm while Mo/Be mirrors have at around 11.3 nm [91]. Although Mo/Be coated mirrors have a wider spectral bandwidth response than Mo/Si coated ones, there is no source found that can make use of this advantage up to now [100]. Also, Be is a hazardous material so that manufacturing of Mo/Si coated mirrors is much easier. Due to these considerations, mainly Mo/Si coated mirrors are preferred as system components in EUVL systems.

EUVL systems became realizable because of the development of these highly reflective coatings [101]. Besides, the wavelength requirement for the EUVL systems comes from the reflection wavelength of the Mo/Si coated mirrors. Thus the light which will be used for EUVL has to have an emission near 13.5 nm. It was shown that a different choice for the coatings other than 13.5 nm peak wavelength causes a loss in the light source [100]. Reflectivities of 70%

for normal incidence have been achieved for Mo/Si coated mirrors [102]. In reality, the Mo/Si mirror response under the central Bragg peak is in the 7.4% bandwidth centred at 13.5 nm [103] but for the focussing and aberration compensation purposes, multiple reflections are needed so that the output is in the 2% bandwidth centred at 13.5 nm. Thus while finding the conversion efficiency of the system, this situation has to be taken into account.

The output power has a relation with the input power of the laser as [97];

$$P_{EUV} = P_{laser} \times \eta \times \Omega \qquad (4.10)$$

where η is the conversion efficiency and Ω is the collectable solid angle in steradian. What is meant for the conversion efficiency in an EUVL source is the ratio of the power of the 2% bandwidth at 13.5 nm radiation in a collected solid angle -which is usually 2π sr- to the incident laser power. For EUVL by LPP, a 3% conversion efficiency in the 2% bandwidth centred at 13.5 nm is required. Also, in typical EUVL systems that are due to LPP, the repetition rate is 5-10 kHz. But if the conversion efficiency is increased, the repetition rate and the total incident power requirements are lowered which in turn reduces the initial cost and the maintenance expenses of the whole system [104].

By using a general approach to the problem, the conversion efficiency of an EUVL source can be calculated from the in-band emission energy of the plasma. For a spectral radiance L_λ [97];

$$E_{in-band} = \int_0^{\Delta t} \int_{-\Omega/2}^{\Omega/2} \int_{\lambda_0-\Delta\lambda/2}^{\lambda_0+\Delta\lambda/2} \int_0^{r_p} 2.r.L_\lambda.dr.d\lambda.d\Omega'dt' \qquad (4.11)$$

where r_P is the plasma radius, Ω is the collected solid angle and Δt is the duration of the in-band emission or the radiative cooling time.

If the plasma is stationary and homogeneous, the in-band emission energy of equation (4.11) reduces to [97];

$$E_{in-band} \approx L_\lambda.\Delta\lambda.\Omega.A_S.\Delta t \qquad (4.12)$$

where A_S is the target area that is used to produce the plasma. This approximation can be used for lasers with long pulse durations like the ones that are used as the EUV laser sources. Here it should be noted that $A_S = \pi r_P^2$ and in order to have a high conversion efficiency, the plasma radius must be smaller than the radius of the emission collection. From this equation, it is

possible to increase the in-band emission by increasing the duration of the in-band emission i.e. Δt. The laser light sources that are used to produce EUVL are pulsed sources and the plasma formed by using them cools down after which emission becomes impossible. This cooling process is due to the loss of energy due to the emission of radiation, heat conduction to the cooler parts of the plasma, loss of high velocity particles from the irradiated target source and plasma expansion.

The radiative cooling time of the plasma can be defined as the time by which half of the energy is radiated, i.e. [97];

$$\Delta t \approx \frac{E_{plasma} / 2}{P_{emission}} \tag{4.13}$$

which is equal to [97];

$$\Delta t \approx \frac{E_{ion}.n_i}{2.n_e.n_i.h\upsilon < \sigma_\upsilon > .G(\tau_0)} \tag{4.14}$$

where n_i and n_e are the ion and electron densities respectively, $< \sigma_\upsilon >$ is the collisional excitation rate coefficient and $G(\tau_0)$ is the photon escape factor. From this equation, the radiative cooling time is obtained of the order of nanosecond scales. This radiative cooling time is also approximated to be equal to the plasma existence time which comes from the inertial confinement works. If d_{plasma} is the shortest extension of the plasma, the plasma existence time can be found as [97];

$$\Delta t_{plasma} \approx \frac{d_{plasma}}{v_{ion}} \tag{4.15}$$

where M is the atomic mass of the target element, kT_i is the ion temperature and v_{ion} is the ion velocity which is equal to [97];

$$v_{ion} \cong 1,4.10^4 \sqrt{\frac{kT_i}{M}} . \tag{4.16}$$

The spectral radiance L_λ from any source is [97];

$$L_\lambda = S_\lambda(1 - \exp(-\tau(\lambda))) = \frac{\varepsilon_\lambda}{\kappa(\lambda)}(1 - \exp(-\tau(\lambda))) \tag{4.17}$$

where S_λ is the source function, ε_λ is the emission coefficient, $\kappa(\lambda)$ is the absorption coefficient and $\tau(\lambda)$ is the optical depth which can be found by using equation (2.42).

The spectral radiance varies with time since plasma cools down in time and it also varies with location since the ion and electron densities change from location to location. For an optically thick plasma, the optical depth is very high since the absorption is dominant. In this case, spectral radiance becomes almost equal to the source function and this case corresponds to the Planck's blackbody emission. On the other hand for an optically thin plasma ($\tau \ll 1$), the spectral radiance can be approximated to be equal to $S_\lambda \tau$ and is much smaller than the Planck's blackbody emission.

An efficient EUV output means that the output energy should approach the Planck limit since for a given wavelength, the blackbody radiation is optimum if the Planck's curve has a peak at that particular wavelength. In order to obtain such a result, a certain temperature must be satisfied which can be calculated by using the Wien's law of radiation. This Planck's limit corresponds to a plasma which is optically thick. But this in turn means that the photons that are released as a result of excitation are re-absorbed inside the plasma.

Optical thickness is not a sufficient condition for a high conversion efficiency. The conversion efficiency depends also strongly on the geometry of the plasma. For example if the plasma is optically thick and long in terms of extension in the direction of irradiation and short in the other directions, then the emitted light in these shorter extended directions will be wasted. For that reason, the produced plasma must be optically thick in all directions in order to obtain a high conversion efficiency.

This limiting case can be obtained if the excited state levels are in local thermal equilibrium, i.e. if the excited state level populations are of Maxwell-Boltzmann distribution. This in turn means that the collisional de-excitation rate is bigger than the spontaneous emission rate which brings out a lower electron density limit to the plasma [15];

$$n_e \geq 9,25.10^{17}.\left(\frac{h^3 \upsilon^3 k T_e}{R_y^2}\right)^{1/2} \tag{4.18}$$

where R_y is the Rydberg constant which is approximately equal to 13.6 eV. In an EUVL source, this corresponds roughly to en electron density of the order of 10^{20} cm^{-3}. But if the plasma is optically thick, this term must be multiplied by the escape factor $G(\tau)$ since due to the re-absorption of the released photons

inside the plasma, the spontaneous emission rate will decrease. For $\tau \gg 1$, i.e. for an optically thick plasma [97];

$$G(\tau) \approx \frac{(\pi \ln \tau)^{1/2}}{\tau} \tag{4.19}$$

and from $\ln \tau \approx 4$ [6];

$$n_e \geq 4,6.10^{16}.\left(\frac{h^3 \upsilon^3 kT_e}{R_y^2 \tau}\right)^{1/2} \tag{4.20}$$

must be satisfied.

4.3.2 Effects on the EUVL System Lifetime

The Mo/Si coatings on the mirrors are made by alternatingly depositing Mo and Si on the mirror surface. The reflectivity of these mirrors depends on the number of layers coated on the surface. When debris mitigate to the surface of these mirrors, this may result in the reduction of the number of layers or the layers may be damaged or the mirror is coated by the debris of the material which absorbs the radiation coming from the plasma [105]. As a result of these effects since the reflectivities are affected, so does the conversion efficiency of the EUVL output.

These debris are actually the ions, neutrals and the particulates from the source element or the particulates that come from the other surfaces inside the chamber and which are fast enough to reach the collector optics and damage them. The degree of damage changes from source to source. The debris mitigation is a major concern for the collector optics since they are the ones that are nearest to the plasma. As a result it can be said that the lifetime of an EUVL system depends on the reflectivity of mainly the first collimator mirror since it is the one that is directly exposed to the debris mitigation problem and so is the one that looses its reflectivity in time. In order to industrialize the EUV lithography, the collector mirrors should be able to function for 10^9 shots [106]. Besides the ones given above, the reasons for the reduction in the reflectivity of the mirrors can be due to the out-of-band radiation which cannot be reflected from the coatings that are used in the mirrors and which results in unwanted heating of the mirrors [107].

The particulates independent of its origin may contaminate, coat or scratch the mirrors depending on its physical state and kinetic energy. Ions with sufficient energy may ablate or sputter the coating layers on the mirrors. Depending on the material type, neutral particles may have different effects. For example if the neutral atom is an oxygen atom, oxidation may occur on the silicon coated upper surface of the mirrors.

Since xenon is an inert gas, the lithographic systems that make use of xenon as the source material is free from particulates [106]. However the conversion efficiency of xenon is low. On the other hand the conversion efficiency of tin plasma is the highest among the sources that have been used in time but also contamination of the optics is severe for the case of tin plasmas. Therefore ways to limit the debris mitigation problem have been investigated in time, which are the inclusion of ambient gases [108], application of magnetic fields [109], application of electrostatic repeller fields [110], mass-limited targets and minimizing the number of atoms in the target [107, 111]. Typically, collector mirrors are placed 15 to 20 cm from the plasma [106]. Thus, the distance between the plasma and the first collector optic is big enough to make use of the combinations of these schemes [105, 112].

Inclusion of an Ambient Gas

In laser produced plasmas, the average velocity of ions is more than that of the neutrals since besides the pressure gradient they are also affected from the space charge effect. However there exist neutrals which are more energetic than the others since they are a result of the recombination process of energetic ions. When an ambient gas is included into the chamber, it results in the deceleration, attenuation and thermalization of the particles inside the plasma and the formation of shock waves [112]. Thus the inclusion of an ambient gas effects the kinetic energies of the particles inside the plasma. As the pressure inside the chamber increases, the number of collisions between the plasma and the gas increases so that the particles constituting the plasma slow down. As a result of this slowing process, the energies of the excited ions approach the neutral atom's energies [106].

Most of the gases absorb radiation around 13,5 nm so that it is important to choose the appropriate gas as the ambient gas. For lithographic application

hydrogen, helium and argon are the gases that are preferred since they have much better transmission to 13,5 nm radiation than the other gases. The transmission of the in-band emission for argon is less than that of helium and hydrogen while hydrogen has the highest transmission rate among them. Also since hydrogen and helium are lighter gases than argon, they require a higher pressure than argon does in order to slow down the particulates or the ions and neutrals from tin [112]. But the insertion of an ambient gas leads to the formation of ambient plasma due to the collisional excitation and ionization processes taking place between the ambient gas and the plasma. Also the ambient gas can be ionized due to the absorption of the UV and EUV radiation from the plasma [106].

Harilal et al. [106] and Amoruso et al. [113] have reported that there exist three different pressure regimes. In vacuum or at low pressures there is no external viscous force so the plasma expands without any interruption. At an intermediate pressure value, the plasma and the gas interaction results in the splitting or sharpening of the plasma [114]. The reason for this is attributed to the division of the plasma to a part which interacts with the ambient gas and a part which expands freely as if it is in vacuum. The part that expands freely through the vacuum is a part which consists of particles that do not undergo collisions with the ambient gas and the part that is slowed down by the gas is the part that undergoes a lot of collisions and form a delayed part. On the other hand for very high pressure values, the expansion of the plasma is stopped by the ambient gas and the particles inside the plasma become thermalized.

Finally it has been reported that as the density of the gas inside the chamber is increased, so does the absorption of the emitted in-band EUV radiation by the ambient gas. Thus by just including an ambient gas into the chamber, it is not possible to protect the optics in the system [112].

Application of a Magnetic Field

When a magnetic field is applied to the plasma, it interacts with the charged particles. In order to reduce the debris mitigation problem, transverse magnetic field by using two permanent magnets is applied to the plasma. In order for the magnetic field to be uniform over the plasma, the target is placed at equal distances from the poles of the two magnets [112]. It has been suggested that

an applied magnetic field B to the laser produced plasma stops the plasma at a distance of $r \approx B^{-2/3}$ and so confines it. However for high Z ions like tin, the plasma expansion is slowed down rather than confinement [112]. Thus an applied magnetic field slows down the ions inside the plasma and besides reducing the debris mitigation problem, it also enhances the emission of radiation [115]. However the inclusion of a magnetic field introduces instabilities to the plasma [116].

Repeller Field Configuration

In the repeller field configuration (Figure 4.3 [107]), an electrostatic field between the multilayer mirrors and the radiation source (i.e. the plasma) is generated by using electrodes. This electrostatic field repels the charged particles but cannot block the passage of neutrals or particulates from the source side to the collimator side.
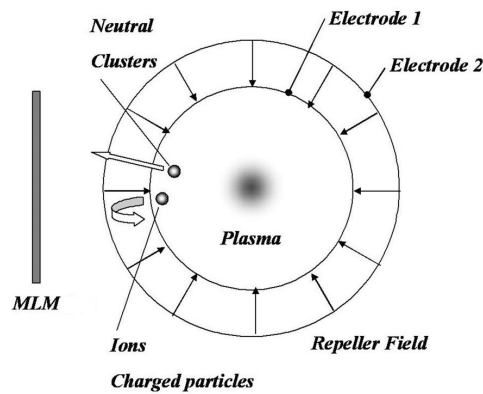
Figure 4.3 Repeller field configuration [107].

4.3.3 Different Target Configurations

In order to increase the conversion efficiency and decrease the debris mitigation problem, besides the solid state form, different targets with different physical states or concentration or form have been investigated in time. A solid target

93

with a different form is the thin tape targets (Figure 4.4a) [117]. This type of target approach enables a new surface of target to be applied to the irradiation until the tape is finished. The debris production is reduced in comparison with the solid targets since the shock waves produced travel through the tape rather than be reflected to the surface. However, still the debris production is a serious problem for its usage in the lithographic systems. Also another drawback is that, all the materials cannot be put into a tape form making it eligible for some certain types of materials.

Liquid targets are ejected from a nozzle in the form of a jet which freeze out to form a solid filament (Figure 4.4b) or further breaks up into a train of droplets (Figure 4.4c) [117, 118, 119]. They are regenerative targets so that they allow the operation of high repetition rate lasers without interruption. Because they are ejected from a nozzle, they can be ejected to a place that is far from the optics in the system causing much less contamination. Besides, the target material produced is small in size which also reduces the debris produced. But in order to use liquid droplet targets, the target must be ejected to an area which has a sufficient pressure to inhibit the evaporation rate.

The gas-puff targets (Figure 4.4d) for the development of soft x-ray radiation were firstly used in the Institute of Optoelectronics [120, 121, 122]. It is formed by injecting gas from a nozzle into the region where the laser is focused. This injection is done at a place that is very near to the laser focus and with a repetition rate that is equal to the repetition rate of the laser so that each time a small amount of gas is injected into the region in concern. Thus, gas-puff targets are regenerative targets. In the case of lasers with very high repetition rates - as is the case for the ones that are used for lithographic systems that are used for volume production -, the fact that nozzles cannot eject gaseous material with such high repetition rates made way to the usage of gaseous jets with continuous flow [123]. The resultant spectra of a gas-puff target have very high spectral resolution due to its characteristic features. The reason that gas targets began to be used stems from the fact that the optics are not contaminated when the gas expands through the vacuum at room temperature [124].
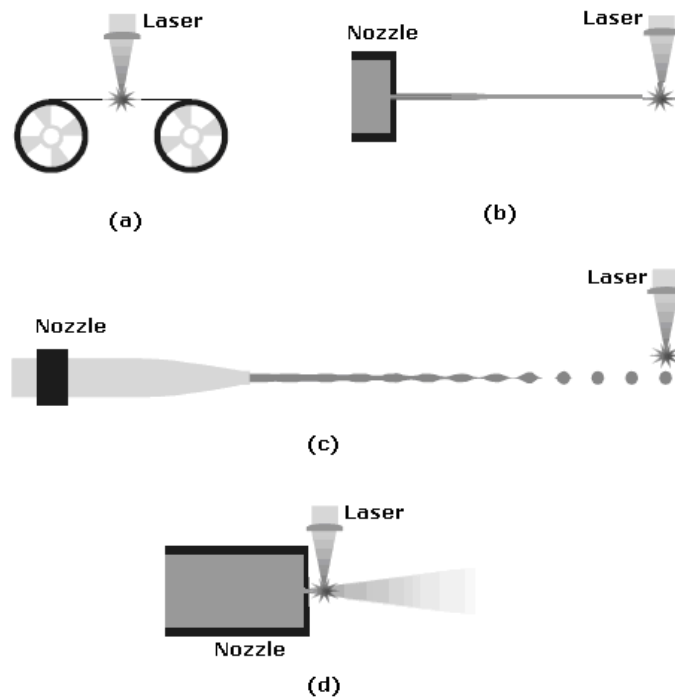
Figure 4.4 Usage of the targets with different physical states (a) Tape target (b) Liquid jet target (c) Liquid droplet target (d) Gas target [117].

In the limited mass target concept, the target's mass and so size is limited so that the number of atoms that emit radiation is just enough to provide the radiation for EUVL requirements, i.e. the purpose is to use minimum number of atoms which would result in a sufficient EUV radiation. By using such a configuration, it is aimed to minimize the number of neutral atoms and the solid particles that are teared off from the target material which propagate with high velocity towards the optics in the system so that debris mitigation problem is reduced. It has been observed that the bandwidth of emission broadens significantly when pure tin targets are used for irradiation [107]. On the other hand when the tin concentration is varied from 1% to 5%, the bandwidth is narrow about 6,5% bandwidth centred at 13,5 nm and there is no significant change about the spectrum bandwidth in this concentration interval.

From the numerical analysis that were done by Cummings et al. [125] it was seen that 1% concentration of tin is enough for a useful EUV output. Furthermore from the experiments that Hayden et al. [126] have made it was

shown that 15% concentration of tin gives the brightest emission in the 2% bandwidth of 13.5 nm and from the experiments that Harillal et al. [115] have done, it was shown that 0.5% of tin concentration is enough for a bright emission. But mass-limited target means that the material is dispersed in a liquid such as water or resorcinol formaldehyde (for example solving Tin in resorcinol formaldehyde results in SnO_2) which in turn causes debris mitigation problem [127].

Finally in the case of minimum mass targets, the target is a pure target such as tin, but the number of atoms of the target is minimized. What is meant from minimization is actually an optimization problem i.e. the number of atoms in the target has to be optimized to a case of minimized debris mitigation with maximized conversion efficiency [127].

4.3.4 Elements that are used as Targets for EUVL Application

The elements that are used for investigation for EUVL application are mainly oxygen, lithium, xenon and tin [128]. Oxygen and lithium are actually not that popular elements in this sense due to their chemical reactivity. But xenon and tin seems eligible for the EUV radiation and so they are the ones that are being investigated more. The advantage of xenon is that it is a noble gas. As for tin, it is a solid at ambient conditions and so it causes contamination of the optics that are used in the lithographic systems. But tin's efficiency in the Mo/Si response bandwidth makes it more suitable for its usage in the lithographic systems than xenon.

EUV emission from lithium comes from the Lyman-α line due to two times ionized lithium (Li^{2+}) so that the electron temperature needed for such an emission is approximately 100 eV [129, 130]. The lithium EUV spectra is a single line spectra centred at 13,5 nm with a width of 0.03 nm [100] so that there is no out-of-band emission. It has relatively few bound electrons and although the laser energy that is converted into the radiation is small, a significant amount of the radiation emitted is in the 13.5 nm band if the lithium is highly ionized [104]. Lithium also causes significant debris problem when used in solid form. For this reason, LiF or LiCl solutions that are dissolved in water resulting in different lithium concentrations have been used.

96

The oxygen emission for lithographic application comes from the five times ionized oxygen ions i.e. lithium-like oxygen ions and is due to the 4d-2p transitions [131]. The oxygen atoms in the water droplets are used for the production of radiation. The obtained spectrum is a narrow peak emission spectrum at around 13 nm [107]. Besides this, oxygen has an out-of-band emission at 15 nm due to the 2s-3p transitions [115].

As for xenon, the main in-band emission comes from the Xe^{10+} ions [132, 133]. Xenon's emission spectrum in the region of interest is in the form of unresolved transition arrays, concept of which will be described in section 4.3.5. The transitions that yield radiation between 13-14 nm are 4p-4d, 4d-4f and 4d-5p, where mostly the radiation between 13-14 nm comes from the 4d-5p transitions [134]. It has been reported by Fahy et al. [132] that according to the plasma modelling simulations the maximum concentration of Xe^{10+} ions that can be achieved in a laser produced plasma is 50%. However the conversion efficiency from the xenon plasma obtained thus far is around 1% which is low in comparison with the 3% conversion efficiency requirement for volume production. The emission spectra of xenon can be found in various literature [128, 132, 135, 136].

Finally for tin, the transitions in the 13-14 nm spectral range is ascribed to come from the 4d -4f 4p - 4d and 4d -5p transitions [136, 137, 138, 139, 140, 141]. Although for xenon there exists various simulation results in the literature, the works on tin is restricted to a few. As for the tin plasma emission in the EUV region it was shown theoretically that, the in-band UTA emission is coming from the Sn^{9+}-Sn^{12+} ions and that the lower charged ions (Sn^{6+}-Sn^{8+}) are responsible for the UTA emission above 15 nm [142]. On the other hand, White et al. [138] have reported that Sn^{7+}-Sn^{12+} ions are responsible for the emission in the region of interest. Since the subject on which ions emit more in the in-band spectral region is not as clear as in xenon, the subject in concern needs more investigation in order to increase the lithographic system efficiency as tin is the most promising target material due to its high conversion efficiency.

4.3.5 Unresolved Transition Arrays

O'Sullivan and Carrol [143, 144] have experimentally shown that the LPP spectra of lanthanides and the adjacent materials (i.e. $50 \leq Z \leq 70$) have

resonance emission structures and as the atomic number increases, they show a quasicontinuum. These structures are called *Unresolved Transition Arrays* (UTA) and they are known as the 4d-4f transitions of multiply charged ions which have half-filled N shells. They have also shown that the peak wavelength of these UTA are due to the $\Delta n = 0$ transitions (from n=4 to n=4) and it decreases as the atomic number of the element increases. Also for $\Delta n \neq 0$ transitions it has been observed that [142], the wavelength decreases as the difference approaches zero. But for $\Delta n = 0$ transitions, there exists a minimum transition wavelength value with respect to the ion charge. For Sn this is around 13 nm and for Xe it is around 11 nm, thus making Sn more suitable for lithographic application.

Unresolved transition arrays (UTA) are formed due to the total number of transitions between two electronic configurations [145]. The emission lines due to the transitions between these two particular electronic configurations merge as a result of the broadenings and so form an array of lines which are unresolvable. The transitions that are responsible for such a spectrum in the emission spectra of high Z (atomic number) materials are the bound-bound transitions between two electronic configurations and they stem from the fact that high Z materials have many bound electrons and a large number of closely packed atomic energy levels [104]. Thus, UTA (Unresolved Transition Arrays) are composed of thousands of line emissions that are so close to each other that they form a quasi-continuum. They are brighter than any line emission source so that they are eligible to be used in EUV lithography. Statistical methods are being used in order to characterize UTA (i.e. namely in terms of position, width and symmetry) since they are very complex [138, 146]. As the atomic number increases, the complexity of the UTA also increases and its profile becomes very sensitive to the target concentration [147].

4.4 EUV Simulations of Tin for Lithographic Application

Soft x-rays emitted from the Sn^{11+} and Sn^{12+} ions were simulated by using the 1D code EHYBRID [16]. The fractions of ions inside the plasma and the line intensities versus wavelength for different electron temperatures were simulated by using the collisinal radiative code NeF [23, 148]. The ion stages in the research in concern are the Sn^{11+}, Sn^{12+} and Sn^{13+} ions so that during the simulations, according to the validity criterion of McWhirter and Hearn [138, 149] collisional radiative codes have been used.

The atomic data were calculated by using the Cowan code. The number of transitions defined for Sn^{11+} and Sn^{12+} ions are 324 and 150 respectively. These transitions that were calculated are due to the 4d - 5p , 4d - 4f and 4p - 4d transitions. Prior works have shown that in order to obtain the spectra of tin ions, the energies have to be scaled [141]. In this work, this scaling factor of energies is 0,80.

In the EHYBRID simulations, the emission for the intensity values of 1.10^{12}, 3.10^{12} and 5.10^{12} W/cm^2 were investigated for a 1064 nm wavelength of irradiation. The pulse duration was chosen as 6 ns [150]. The slab thickness of the solid tin target in the simulations were chosen as 20 μm. A post-processor code coupled to EHYBRID was used to obtain the emitted line intensities. This code makes use of the simulated excited level population densities in the EHYBRID simulation. The simulation results for the intensity values given above can be seen in Figure 4.5, Figure 4.6 and Figure 4.7 for the Sn^{11+} ion and Figure 4.8, Figure 4.9 and Figure 4.10 for the Sn^{12+} ion. From the simulation results it can be seen that the greatest emission intensity is centered near to 13,5 nm for the Sn^{11+} ion and 13,4 nm for the Sn^{12+} ion. Prior simulation results from the works of White. et al. [138] have shown that the peak intensity for both ions is centred near 13,5 nm. The reason for this discrepancy may be due to the scaling factor that was used in our calculations. Also from the simulation results it can be seen that as the incident laser intensity is increased, the emission intensity is decreased. This is attributed to the effect of opacity since it is known that tin plasma is optically thick to the extreme ultraviolet emission around 13,5 nm [150].
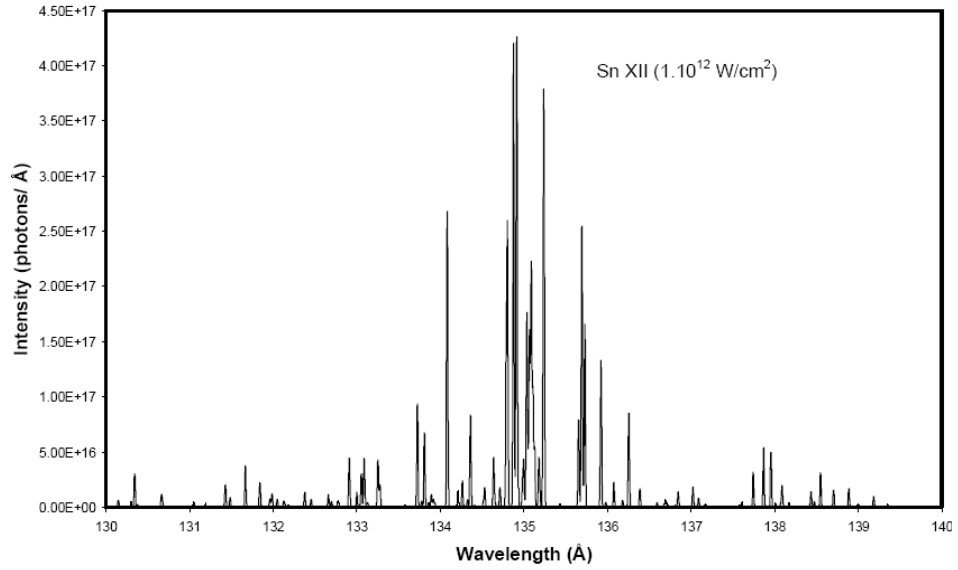
Figure 4.5 EHYBRID simulation result of the Sn^{11+} ion for a 1064 nm laser irradiation at 1.10^{12} W/cm^2 with a 6 ns pulse duration. The spot size is 145 µm [150].
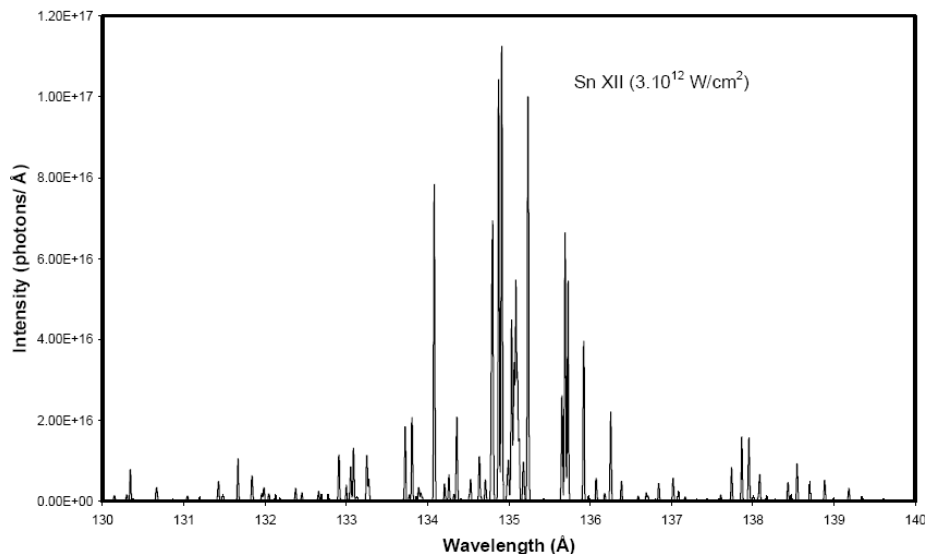
Figure 4.6 EHYBRID simulation result of the Sn^{11+} ion for a 1064 nm laser irradiation at 3. 10^{12} W/cm^2 with a 6 ns pulse duration. The spot size is 84 µm [150].
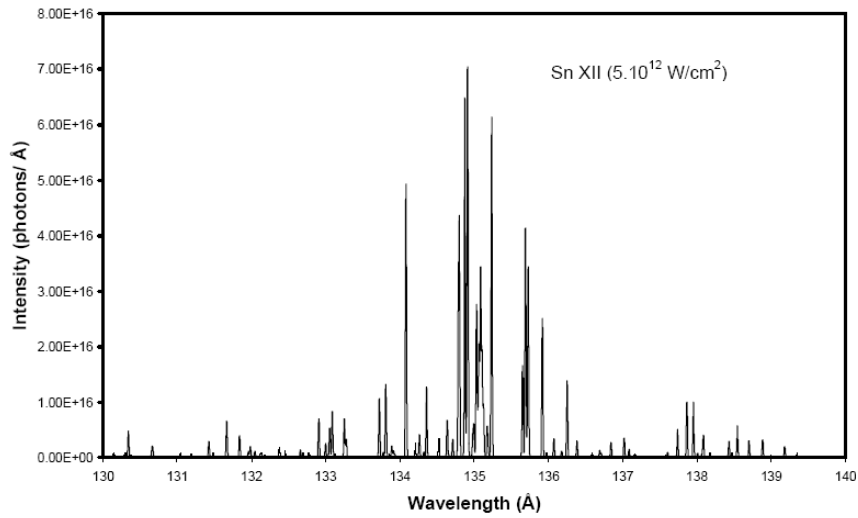
Figure 4.7 EHYBRID simulation result of the Sn^{11+} ion for a 1064 nm laser irradiation at 5. 10^{12} W/cm^2 with a 6 ns pulse duration. The spot size is 65 μm [150].
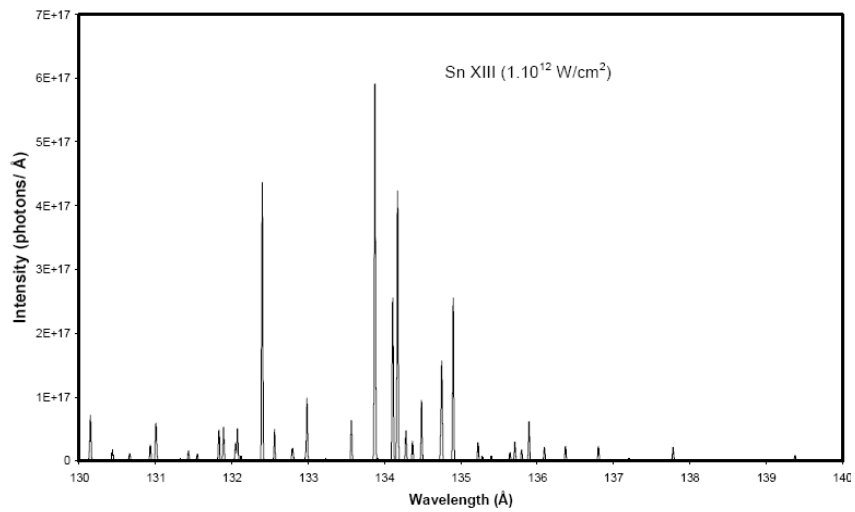
Figure 4.8 EHYBRID simulation result of the Sn^{12+} ion for a 1064 nm, 6ns laser irradiation at 1. 10^{12} W/cm^2. The spot size is 145 μm [150].
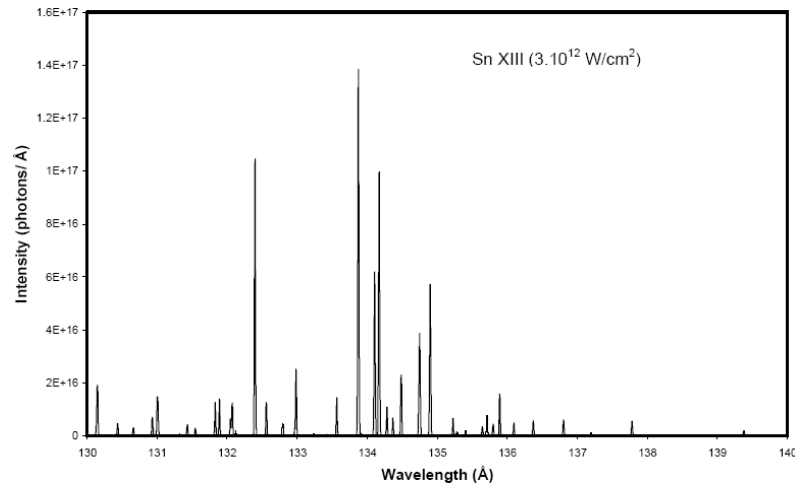
Figure 4.9 EHYBRID simulation result of the Sn^{12+} ion for a 1064 nm laser irradiation at 3.10^{12} W/cm^2 with a 6 ns pulse duration. The spot size is 84 μm [150].
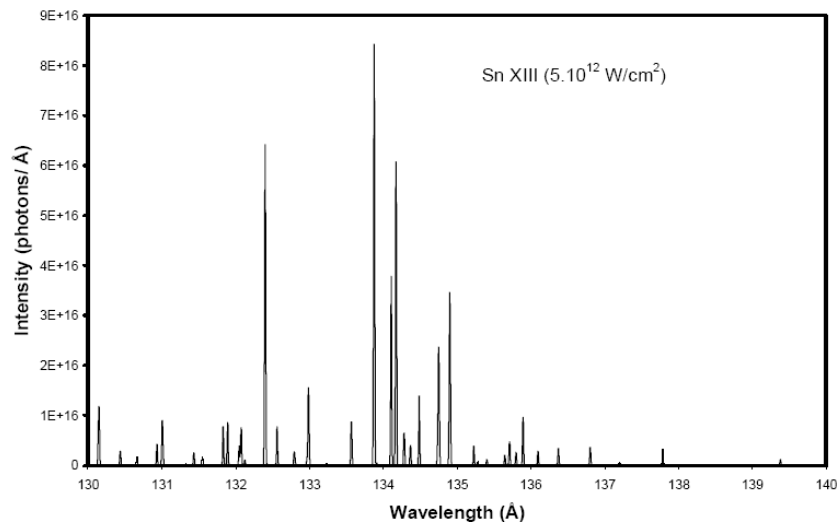
Figure 4.10 EHYBRID simulation result of the Sn^{12+} ion for a 1064 nm laser irradiation at 1.10^{12} W/cm^2 with a 6 ns pulse duration. The spot size is 65 μm [150].

EUV output depends on electron temperature inside the plasma since the populations of the ions and the excited level populations of these ions determine the output UTA emission. Because of this, the relation between the ionization fraction and the electron temperature and the relation between the output EUV

emission intensity and the electron temperature has been investigated. The code NeF was used for the purpose of determining the ion fractions of different ion stages under steady state condition. It can be seen from Figure 4.11 and Figure 4.12 that the Sn^{10+}, Sn^{11+} and Sn^{12+} ions have their greatest fractions at around 50-70 eV range. In Figure 4.13, the intensity versus wavelength simulations from the steady state NeF code can be seen. In this figure it can be seen that the peak intensity that is centred near the 13,5 nm was obtained for an electron temperature of 60 eV. From 40 to 60 eV, the total emission intensity increases and beyond this electron temperature, it decreases. From Fig. 4.11 and Fig. 4.12, at 60 eV the ion fraction is mostly composed of the Sn^{11+}, Sn^{12+} and Sn^{13+} ions. Also from these figures it is seen that in between the 50-70 eV electron temperature range, most of the ion fraction is due to the Sn^{10+}, Sn^{11+}, Sn^{12+} and Sn^{13+} ions. Thus, the main contribution to the emission near 13,5 nm comes from these ions according to our simulation results.
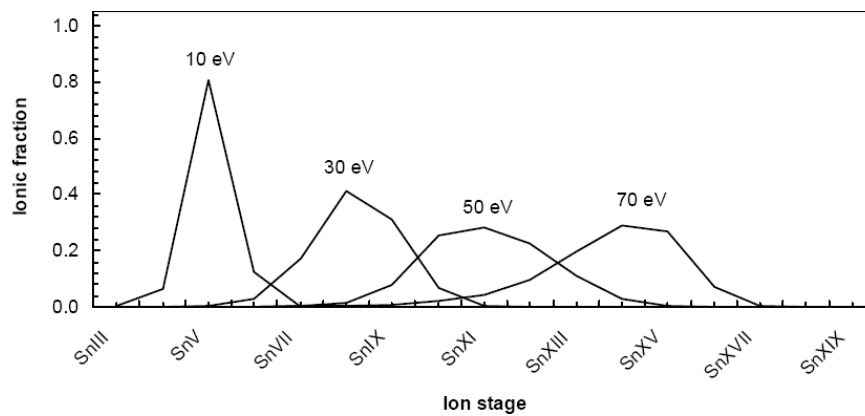
Figure 4.11 The ion fraction of the tin ions according to the electron temperature at electron density of $1x10^{20}$ cm^{-3} [150].
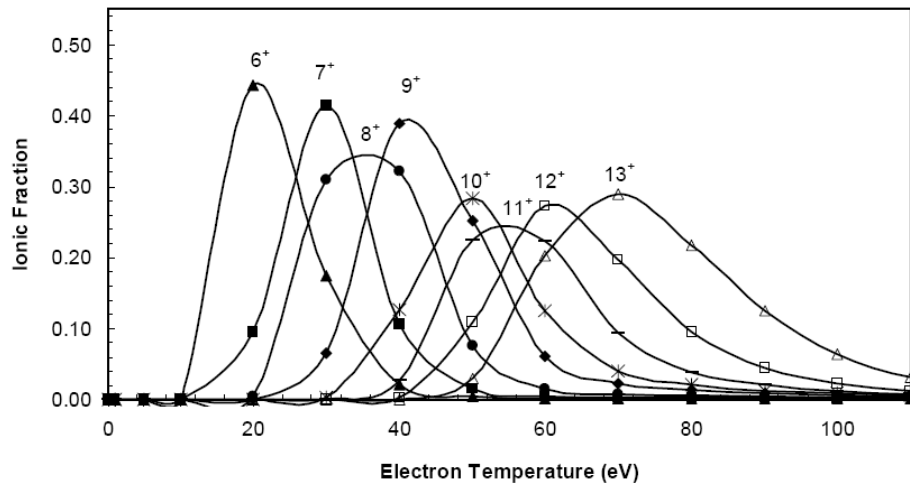
Figure 4.12 The ion fraction of the tin ions according to the electron temperature at an electron density of 1×10^{20} cm^{-3} [150].
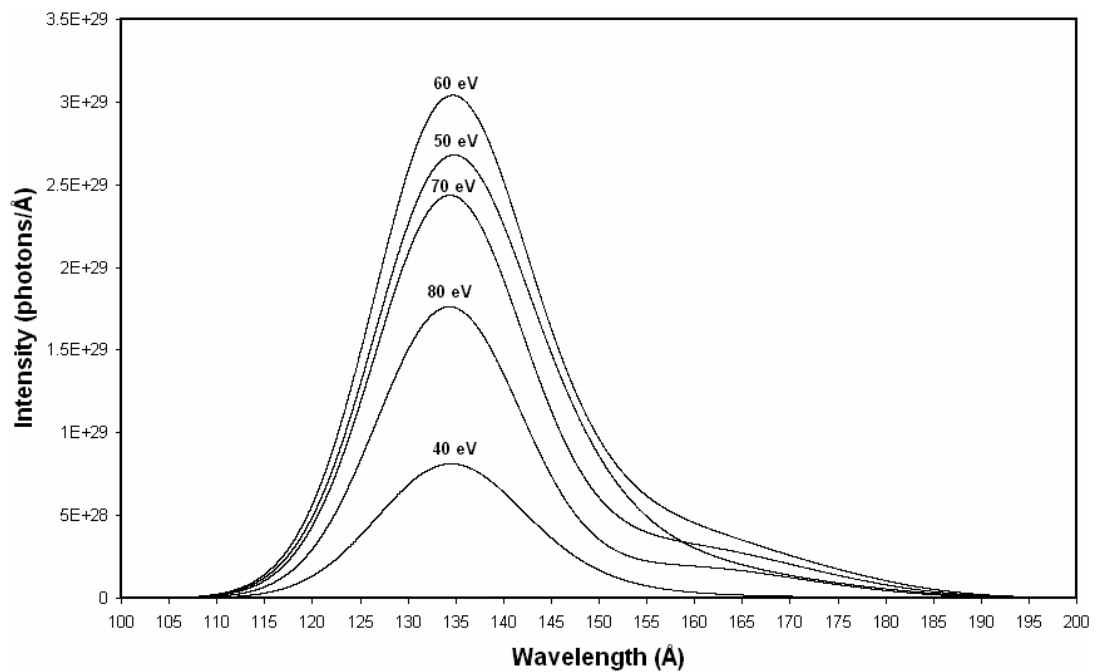
Figure 4.13 Intensity of the tin lines emitted from Sn^{11+}, Sn^{12+} and Sn^{13+} ions as a function of wavelength at an electron temperature changed between 40 and 80 eV at an electron density of 1×10^{20} cm^{-3} [150].

CHAPTER 5

CONCLUSIONS

Grazing incidence pumping simulations of neon-like titanium and nickel-like molybdenum have been made by using the 1 dimensional hydrodynamic code EHYBRID. In these simulations, atomic data of the transitions that yield emission at 18,9 nm for nickel-like molybdenum and 32,6 nm for neon-like titanium have been obtained by using the COWAN code.

In the nickel-like molybdenum simulations, the laser wavelength was chosen as 800 nm to simulate a Ti:Sappire laser system. The prepulse energy was initially chosen as 70 mJ with a pulse duration of 200 ps. Also, the main pulse energy and pulse duration were initially chosen as 80 mJ and 1,2 ps respectively. These initial parameters were based on the works of Keenan et. al [67]. The prepulse was focused to $4\,\mathrm{mm} \times 15\,\mathrm{\mu m}$ and the main pulse was focused to $4\,\mathrm{mm} \times 80\,\mathrm{\mu m}$. Firstly, the optimum grazing incidence angles for a delay time of 300 ps for 18,9 nm emission was searched for. This optimum value has been obtained as 14° under these conditions. Then, for a grazing incidence angle of 14° and delay time of 300 ps, the optimum main pulse energy was investigated and it has been found that under these conditions, the gain was saturated after an energy of 150 mJ. As for the prepulse energy it has been found that the most suitable energy was in between 70-80 mJ due to the electron density. FWHM values for a 70 mJ prepulse energy was found as 23 ps and for a 80 mJ prepulse energy as 29 ps.

In the neon-like titanium simulations, the prepulse which was directed longitudinally to the target initially had an energy of 70 mJ and a pulse duration of 200 ps. As for the main pulse, it is directed with a grazing incidence angle and its energy and pulse durations were initially chosen as 80 mJ and 1,2 ps respectively. The laser pulse wavelength was set to 800 nm, concerning a

Ti:Sapphire laser system and the prepulse was focused to $4\,mm \times 15\,\mu m$ while the main pulse was focused to $4\,mm \times 30\,\mu m$.

During the simulations firstly, the optimized grazing incidence angle for a delay time of 300 ps has been searched for and it has been found that the peak gain is obtained at an angle of 17°. Afterwards, for a grazing incidence angle of 17°, the optimized delay time has been searched for and it has been found that the biggest gain under these conditions is obtained for a delay time that is near to 300 ps. After finding the maximum gain for a grazing incidence angle of 17° and a delay time of approximately 300 ps, the prepulse that gives the maximum gain has been searched for and it has been found that it actually is 70 mJ. Finally in order to maximize the gain from neon-like titanium at 32,6 nm, main pulse has been searched for and it has been found that the maximum gain is obtained for a mainpulse of 300 mJ. Under these simulation conditions, FWHM of the gain was obtained as 18 ps.

The timing issue which is vital for the amplification of laser pulses in a Ti:Sapphire laser system has been theoretically derived. For this reason, firstly the delay times that are introduced by the electrical and electrooptical components have been theoretically calculated. The aim here is to set up a system such that, the initial repetition rate which is 75 MHz is reduced to 10 Hz and each of these pulses pass from the Ti:Sapphire crystal 8 times in the first $3,2\,\mu s$ of the irradiation of the crystal by a second harmonic Nd:YAG laser. The work here had to remain theoretical due to the Pockels Cell problem so that the times given are just an initial approximation. Also because of this, grazing incidence experiments of nickel-like molybdenum and neon-like titanium could not be performed.

The simulations of tin plasma emission at the 2% bandwidth centred at 13,5 nm for lithographic application have been made by using EHYBRID and steady state collisional radiative code NeF. The atomic data were obtained by using COWAN code. The transitions that these data were calculated are 4d - 5p , 4d - 4f and 4p - 4d which yielded 324 and 150 number of transitions for Sn^{11+} and Sn^{12+} ions respectively. The intensities of irradiation were chosen as 1.10^{12}, 3.10^{12} and 5.10^{12} W/cm^2 and the wavelength of irradiation was chosen as 1064 nm. The pulse duration was set to 6 ns. The time integrated emitted line intensities for

the ions Sn^{11+} and Sn^{12+} at these intensities were calculated by using a post-processor code coupled to EHYBRID. From these simulation results, it is seen that as the incident laser intensity is increased, the emission intensities decreased due to the opacity. However for both ions, the 2% neighbourhood of emission which is centred at 13,5 nm is high. Afterwards, the code NeF was used to simulate the ion fraction versus ionization stage and ion fraction versus electron temperature. Also, the intensity of tin lines from the emission of Sn^{11+}, Sn^{12+} and Sn^{13+} ions were simulated. It has been observed that the most intense emission in the 2% bandwidth of 13,5 nm is when the electron temperature is about 60 eV inside the plasma. At this electron temperature value, ionic fraction is actually composed of mostly from the Sn^{11+}, Sn^{12+} and Sn^{13+} ions. Thus according to these simulation results, these are the ions that are mainly responsible for the emission that is eligible for EUV lithographic application.

Hydrodynamic codes are very important in understanding the dynamics of the plasma that emits x-rays. The reason for this is that, they solve for the plasma parameters such as electron density and electron temperature from the fluid model and then substitute them into a plasma emission model such as collisional radiative model. From here, the total x-ray emission is calculated. However, the hydrodynamic codes that are used for modelling x-ray lasers are all 1-D to our knowledge. Simulation of x-ray lasers can further be extended by coding a 2-D hydrodynamic model since this would give a better insight about the dynamics of the plasma from which x-ray laser emission is seen.

REFERENCES

[1] G. J. Tallents, J. Phys. D: Appl. Phys. **36**, R259, 2003.

[2] http://www.coe.berkeley.edu/AST/srms/2007/Intro2007.pdf, May 2008.

[3] D. L. Matthews, P. L. Hagelstein, M. D. Rosen, M. J. Eckart, N. M. Ceglio, A. U. Hazi, H. Medecki, B. J. MacGowan, J. E. Trebes, B. L. Whitten, E. M. Campbell, C. W. Hatcher, A. M. Hawryluk, R. L. Kauffman, L. D. Pleasance, G. Rambach, J. H. Scofield, G. Stone G, T. A. Weave, Phys. Rev. Lett. **54**, 110, 1985.

[4] K. Garloff, M. van den Donker, J. van der Mullen, F. van Goor, R. Brummans J. Jonkers, Phys. Rev. E **66**, 036403, 2002.

[5] "S. S. Harilal, B. O'Shay, M. S. Tillack, M. V. Mathew, J. Appl. Phys. **98**, 013306, 2005.

[6] "Plasma Diagnostic Techniques", Edited by R. H. Huddlestone and S. L. Leonard, Chapter 5 "Spectral Intensities", R. W. P. McWhirter, 1965.

[7] "Physics of Shock Waves and High-Temperature Phenomena", Ya. B. Zeldovich, Yu. P. Raizer, , Edited by: W. D. Hayes, R. F. Probstein, Volume I, Academic Press, 1996.

[8] "Plasma Diagnostics", Edited by W. Lochte-Holtgreven, North-Holland Publishing Company, Amsterdam, 1968.

[9] "Plasma Spectroscopy", T. Fujimoto The International Series of Monographs on Physics Volume 123, Oxford University Press, 2004.

[10] "Principles of Lasers", O. Svelto, D. C. Hanna, Plenum Press, 3rd Edition, 1989.

[11] "Plasma Spectroscopy", G. V. Marr, Elsevier Publishing Company, 1968.

[12] "The Physics of Plasmas", T. J. M. Boyd, J. J. Sanderson, Cambridge University Press, 2003.

[13] "Plasma Diagnostic Techniques", Edited by R. H. Huddlestone and S. L. Leonard, Chapter 6 "Line Broadening", W. L. Wiese, 1965.

[14] "Modern Spectroscopy", M. Hollas, John Wiley and Sons, Ltd. 4th Edition, 2004.

[15] "Plasma spectroscopy", H. Griem, 2.nd edition Mc. Graw Hill, New York, 1964.

[16] G. J. Pert, J. Fluid Mech. **131**, 401, 1983.

[17] G. B. Zimmermann, Comm. Plasma Phys. Control. Fusion **11**, 51, 1975.

[18] J.P. Christiansen, D.E.T.F. Ashby, K.V. Roberts, Comput. Phys. Commun. **7**, 271, 1974.

[19] V.N. Shlyaptsev, A.V. Gerusov, A.V. Vinogradov, J.J. Rocca, O.D. Cortazar, F. Tomasel, S. Szapiro, in: S. Suckewer (Ed.), Ultrashort Wavelength Lasers II, SPIE Proc., vol. **2012**, pg. 99, 1993.

[20] R. W. Lee, et al. J.Q.S.R.T. **56**, 4, 535. Q2, 1996

[21] R.W. Lee, B.L. Whıtten, R.E. Strout II, J.Q.S.R.T. **32**, 91, 1984.

[22] P. Sondhauss, S.J. Rose, R.W. Lee, I. Al'miev, J.S. Wark, J.Q.S.R.T. **71**, 721, 2001.

[23] E. Hajiyev, A. Demir, Comp. Phys. Com. **164**, 86, 2004.

[24] "Plasmas and Laser Light", T. P. Hughes, John Wiley and Sons, New York, 1975.

[25] D. R. Bates, A. E. Kingston, R. W. P. McWhirter, Proc. Roy. Soc. **A267**, pg. 297, 1962.

[26] D. R. Bates, A. E. Kingston, R. W. P. McWhirter, Proc. Roy. Soc. **A270**, pg. 155, 1962.

[27] J. A. M. van der Mullen, Phys. Rep. **191**, 109, 1990.

[28] "Physics of Fully Ionized Gases", L. Spitzer, Interscience, New York, 1956.

[29] S.B. Healy, G. F. Cairns, C. L. S. Lewis, G. J. Pert, J. A. Plowes, IEEE J. of Selected Topics in Quant. Elect. **1**, 949, 1995.

[30] J. Kuba, R. F. Smith, D. Benredjem, C. Möller, L. Upcraft, R. King, A. Klisnick, L. Drska, G. J. Pert, J. C. Gauthier, J. Opt. Soc. Am. B **20**, 208, 2003.

[31] L. B. Golden, R. E. H. Clark, S. J. Goett, D. H. Sampson, Astrophys. J. Suppl. **45**, 603, 1981.

[32] "Introduction to Plasma Physics and Controlled Fusion", F. F. Chen, New York: Plenum, 1984.

[33] T. Holstein, Phys. Rev, **72**, 1212, 1947.

[34] S. Sasaki, S. Takamura, S. Watanabe, S. Masuzaki, T. Kato, K. Kadota, Rev. Sci. Instrum. **67**, 3521, 1996.

[35] L. I. Gudzenko, L.A. Shelepin, Dokl. Acad. Nauk SSSR **160**, 1296, 1965 (Sov. Phys. Doki. **10**, 147, 1965.

[36] K. A. Janulewicz, A. Lucianetti, G. Priebe, P. V. Nickles, X-Ray Spectrom. **33**, 262, 2004.

[37] J. J. Rocca, Rev. Sci. Inst. **70**, 3799, 1999.

[38] S. Suckewer, C. H. Skinner, H. Milchberg, C. Keane, D. Voorhees, Phys. Rev. Lett. **55**, 1753, 1985.

[39] F. E. Irons, N. J. Peacock, J. Phys. B: Atom Mol. Phys. **7**, 1109, 1974.

[40] R. J. Dewhurst, D. Jacoby, G. J. Pert, S. A. Ramsden, Phys. Rev. Lett. **37**, 1265, 1976.

[41] H. Daido, Rep. Prog. Phys. **65**, 1513, 2002.

[42] P. Jaegle, G. Jamelot, A. Carillon, C. Wehenkel, Jpn. J. Appl. Phys. **17**, 483, 1978.

[43] P. Jaegle, G. Jamelot, A. Carillon, A. Klisnick, A. Sureau, H. Guennou, JOSA B **4**, 563, 1987.

[44] G. Jamelot, A. Carillon, A. Klisnick, P. Jaegle, Appl. Phys. B **50**, 239, 1990.

[45] A. N. Zherikhin, K. N. Koshelev, V. S. Letokhov, Sov. J. Quantum Electron. **6**, 82, 1976.

[46] A V Vinogradov, I Sobelman, E. Yukov, Sov. J. Quantum Electron. **7**, 32, 1977.

[47] S. Maxon, P. Hagelstein, K. Reed J. Scofield, J. Appl. Phys. **57**, 971, 1985.

[48] J. Zhang, A. G. MacPhee, J. Lin, E. Wolfrum, R. Smith, C. Danson, M. H. Key, C. L. S. Lewis, D. Neely, J. Nilsen, G. J. Pert, G. J. Tallents, J. S. Wark, Science **276**, 1097, 1997.

[49] J. Zhang, A. G. MacPhee, J. Nilsen, T. W. Barbeen Jr, C. Danson, M. H. Key, C. L. S. Lewis, D. Neely, R. M. N. O'Rourke, G. J. Pert, R. Smith, G. J. Tallents, J. S. Wark, E. Wolfrum, Phys. Rev. Lett. **78**, 3856, 1977.

[50] J. Nilsen, J. H. Scofield, Phys. Scr. **49**, 588, 1994.

[51] Yu V. Afanas'ev, V. N. Shlyapsev, *Sov. J. Quantum Electron.* **19**, 1606, 1989.

[52] N. B. Burnett, P. J. Corkum, Opt. Soc. Am. B, **9**, 1195, 1989.

[53] B. E. Lemoff, C. Y. Yin, C. L. Gordon III, C. P. J. Barty, S. E. Harris Phys. Rev. Lett. **74**, 1574, 1995.

[54] **S.** Sebban, T. Mocek, D. Ros, L. Upcraft, P. H. Balcou, R. Haroutunian, G. Grillon, B. Rus, A. Klisnick, A. Carillon, G. Jamelot, C. Valentin, A. Rousse, J. P. Rousseau, L. Notebaert, M. Pittman, D. Hulin, Phys. Rev. Lett. **89**, 253901, 2002.

[55] Y. Nagata, K. Midorikawa, S. Kubodera, M. Obara, H. Tashiro, K. Tokoda, Phys. Rev. Lett. **71**, 3774, 1993.

[56] M. A. Duguay, P. M. Rentzepis, Appl. Phys. Lett. **10**, 350, 1967.

[57] J. Tümmler, K. A. Janulewicz, G. Priebe, P. V. Nickles, Phys. Rev. E **72**, 037401, 2005.

[58] P. V. Nickles, V. N. Shlyaptsev, M. Kalachnikov, M. Schnürer, I. Will, W. Sandner, Phys. Rev. Lett. **78**, 2748, 1997.

[59] J. Zhang, S. T. Chunyu, Y. L. You, Q. R. Zhang, S. J. Yang, W. Z. Huang, D. Y. Wu, X. Q. Zhuang, S. P. Liu, Y. Q. Cai, F. Y. Du, X. D. Yuan, X. F. Wei, Y. K. Zhao, H. S. Peng, J. Nilsen, Phys. Rev. A **53**, 3640, 1996.

[60] B. M. Luther, Y. Wang, M. A. Larotonda, D. Alessi*,* M. Berrill, J. J. Rocca*,* J. Dunn, R. Keenan, V. N. Shlyaptsev, IEEE Journ. Quant. Elect. **42**, 4, 2006.

[61] B. M. Luther, Y. Wang, M. A. Larotonda, D. Alessi, M. Berrill, M. C. Marconi, J. J. Rocca, V. N. Shlyaptsev, Opt. Lett. **30**, 165, 2005.

[62] J. Zhao, Q. L. Dong, F. Yan, J. Zhang, Phys. Rev. A **73**, 033816, 2006.

[63] R. Keenan, J. Dunn, V. N. Shlyaptsev, R. F. Smith, P. K. Patel, D. F. Price, Proc. SPIE, Vol. **5197**, pg. 213, 2003.

[64] "Propagation of Electromagnetic Waves in Plasma", V. L. Ginzburg, Addison–Wesley, 1964.

[65] G. J. Tallents, Y. Abou-Ali, A. Demir, Q. Dong, M. H. Edwards, P. Mistry, G. J. Pert, IEEE Journ. Sel. Top. Quant. Elect. **10**, 1373, 2004.

[66] J. Nilsen, J. H. Scofield, Physica Scripta. **49**, 588, 1994.

[67] T. Boehly, M. Russotto, R. S. Craxton, R. Epstein, B. Yaakobi, L.B. Da Silva, J. Nilsen, E. A. ChAndler, D. J. Fields, B. J. MacGowan, D. L. Matthews, J. H. Scofield, G. Shimkaveg, Phys. Rev. A **42**, 6962, 1990.

[68] D. Alessi, B. M. Luther, Y. Wang, M. A. Larotonda, M. Berrill, J. J. Rocca, Opt. Exp. **13**, 2093, 2005.

[69] M. A. Larotonda, B. M. Luther, Y. Wang, Y. Liu, D. Alessi, M. Berrill, A. Dummer, F. Brizuela, C. S. Menoni, M. C. Marconi, V. N. Shlyaptsev, J. Dunn, J. J. Rocca, IEEE Journ. Sel. Top. Quant. Elec. **10**, 1363, 2004.

[70] T. Ozaki, R. A. Ganeev, A. Ishizawa, T. Kanai, H. Kuroda, Phys. Rev. Let. **89**, 253902-1, 2002.

[71] G. Steinmeyer, D. H. Sutter, L. Gallmann, N. Matuschek, U. Keller, *Science* **286**, 1507, 1999.

[72] P. W. Smith, Proc. of IEEE, **58**, pg. 1342, 1970.

[73] G. D. Reid, K. Wynne, Encyclopedia of Analytical Chemistry, 13644, John Wiley & Sons Ltd, Chichester, 2000.

[74] http://wprod.bfioptilas.com/global_files/products/465_7_2002347588/Femtosource_SCI.pdf, May 2008.

[75] http://www.lambdaphoto.co.uk/pdfs/SR445Ac_intl.pdf, February 2008.

[76] "Instruction Manual for Pulse Picker System Consisting of DD2, HVP-590-DR, HVPS-9003 and QC-10J Pockels Cell", Quantum Technology Inc.

[77]http://www.teknetelectronics.com/DataSheet/STANFORDRE/STANF_dg5356 0344.pdf, February 2008.

[78] Dazzler Manual.

[79] CFR 400 Manual.

[80] "The Theory of Atomic Structure and Spectra", R. D. Cowan, University of California Press, Berkeley, 1981.

[81] E. Kacar, P. Demir, P. Demir, A. Demir, S. Yaltkaya, Proceedings of the 10th International Conference on X-Ray Lasers, Vol. **115**, pg. 347, 2006.

[82] R. Keenan, J. Dunn, P. K. Patel, D. F. Price, R. F. Smith, V. N. Shlyaptsev, Phys. Rev. Lett. 94, 103901, 2005.

[83] R. Li, T. Ozaki, T. Kanai, H. Kuroda, Phys. Rev. E 57, 7093, 1998.

[84] A. Demir, E. Akman, S. Bilikmen, P. Demir, S. İnce, E. Kacar, E. Yurdanur, S. Yaltkaya, Proceedings of the 10th International Conference on X-Ray Lasers, Vol. **115**, pg. 341, 2006.

[85] A. K. Wong, IEEE Micro, **23**, 12, 2003.

[86] G. E. Moore, Proc. SPIE, vol. **2438**, pg. 2, 1995.

[87] T. Ito, S. Okazaki, Nature, **406**, 1027, 2000.

[88] *G.* L. T. Chiu, J. M. Shaw, IBM J. Res. Develop. **41**, 3, 1997.

[89] E. J. Lerner, The Industrial Physicist, **5**, 18, 1999.

[90] L. W. Liebmann, Proceedings of the 2003 International Symposium on Physical Design, Monterey, CA, USA, pg. 110, 2003.

[91] R. H. Stulen and D. W. Sweeney, IEEE J. Quant. Electr. **35**, 694, 1999.

[92] "The Lithography Expert: The Rayleigh depth of focus", Chris A. Mack, KLA-Tencor, *Microlithography World* February, 2004, http://sst.pennnet.com/Articles/Article_Display.cfm?Section=ARCHI&Subsection =Display&ARTICLE_ID=199855&p=28, February 2008.

[93] M. Richardson, C. S. Koay, K. Takenoshita, C. Keyser, R. Bernath, S. George, S. Teerawattansook, Proc. SPIE. Vol. **5580**, pg. 434, 2005.

[94] S. P. Renwick, D. Williamson, K. Suzuki, K. Murakami, OPN **18**, 35, 2007.

[95] B. Marx, Laser Focus World **39**, 34, 2003.

[96] K. Kincade, Laser Focus World **39**, 55, 2003.

[97] R. Lebert, K. Bergmann, L. Juschkin, O. Rosier, W. Neff, Proc. SPIE, Vol. **4343** Emerging Lithographic Technologies V, Elizabeth A. Dobisz, Editor, pg. 215, 2001.

[98] J. Jonkers, Plasma Sources Sci. Technol. **15,** S8, 2006.

[99] T. Feigl, J. Heber, A. Gatto, N. Kaiser, Nuclear Instruments and Methods in Physics Research A **483**, 351, 2002.

[100] V. Banine R. Moors, J. Phys. D: Appl. Phys. **37**, 3207, 2004.

[101] R. H. Stulen, IEEE Journ. Selct. Top. Quant. Electr. **1**, 970, 1995.

[102] C. Montcalm, S. Bajt, P. B. Mirkarimi, E. Spiller, F. J. Weber, J. A. Folta, Proc. SPIE, vol. **3331**, pg. 42, 1998.

[103] D. G. Stearns, R. S. Rosen, S. P. Vernon, J. Vac. Sci. Technol. A **9**, 2662, 1991.

[104] J. J. MacFarlane, C. L. Rettig, P. Wang, I. E. Golovkin, P. R. Woodruff, Proc. of SPIE, **5751**, pg. 588, 2005.

[105] K. Takenoshita, C. S. Koay, S. Teerawattansook, M. Richardson, V. Bakshi, Emerging Lithographic Technologies IX. Edited by Mackay, R. Scott. Proc. of SPIE, Volume **5751**, pg. 563, 2005.

[106] S. S. Harilal, B. O'Shay, Y. Tao, M. S. Tillack, J. App. Phys. **99**, 083303, 2006.

[107] M. Richardson, C. S. Koay, K. Takenoshita, C. Keyser, M. Al-Rabban, J. Vac. Sci. Technol. B **22**, 785, 2004.

[108] F. Flora, L. Mezi, C. E. Zheng, F. Bonfigli, Europhys.Lett. **56**, 676, 2001.

[109] S. S. Harilal, B. O'Shay, M. S. Tillack, J. Appl. Phys. **98**, 036102, 2005.

[110] K. Takenoshita, C. S. Koay, S. Teerawattansook, M. Richardson, V. Bakshi, Proc. SPIE, Vol. **5751**, pg. 563, 2005.

[111] H. Tanaka, K. Akinaga, A. Takahashi, T. Okada, Appl.Phys. A **79**, 1493, 2004.

[112] S. S. Harilal, B. O'Shay, Y. Tao, M. S. Tillack, Appl. Phys. B **86**, 547, 2007.

[113] S. Amoruso, B. Toftmann, J. Schou, R. Velotta, X. Wang, Thin Solid Films **453–454**, 562, 2004.

[114] S. S. Harilal, C. V. Bindhu, M. S. Tillack, F. Najmabadi, A. C. Gaeris, J. Phys. D **35**, 2935, 2002.

[115] S. S. Harilal, M. S. Tillack, Y. Tao, B. O'Shay, R. Paguio, A. Nikroo, Opt. Lett. **31**, 1549, 2006.

[116] S. S. Harilal, M. S. Tillack, B. O'Shay, C. V. Bindhu, F. Najmabadi, Phys. Rev. E **69**, 026413, 2004.

[117] B. A. M. Hansson H. M. Hertz, J. Phys. D: Appl. Phys. **37**, 3233, 2004.

[118] B. A. M. Hansson, L. Rymell, M. Berglund, O. Hemberg, E. Janin, J. Thoresen*a*, H. M. Hertz*, Soft X-Ray and EUV Imaging Systems II, Daniel A. Tichenor, James A. Folta, Editors, Proc. of SPIE Vol. **4506**, pg. 1, 2001.

[119] P. A. C. Jansson, B. A. M. Hansson, O. Hemberg, M. Otendal, A. Holmberg, J. de Groot, H. M. Hertz, Appl. Phys. Lett. **84**, 2256, 2004.

[120] H. Fiedorowicz, A. Bartnik, P. Parys, Z. Patron, Proc. X-Ray Optics and Microanalysis, pg. 515. Philadephia: IOP Publishing, 1992.

[121] H. Fiedorowicz, A. Bartnik, Z. Patron, P. Parys, Appl.Phys. Lett. **62**, 2778, 1993.

[122] H. K. Fiedorowicz, Laser and Particle Beams, **23**, 365, 2005.

[123] M. Kanouff, H. Shields, L. Bernardez, D. Chenoweth, G. Kubiak, J. Appl. Phys. **90**, 3726, 2001.

[124] R. Bruijn, K. Koshelev, G. Kooijman, E. S. Toma, F. Bijkerk, J. of Quan. Spec. & Rad. Trans. **81**, 97, 2003.

[125] A. Cummings, G. O'Sullivan, P. Dunne, E. Sokell, N. Murphy, J. White, J. Phys. D: Appl. Phys. **38**, 604, 2005.

[126] P. Hayden, A. Cummings, L. Gaynor, N. Murphy, G. O'Sullivan, P. Sheridan, E. Sokell, J. White, P. Dunne, Proc. SPIE **5751**, pg. 919, 2005.

[127] S. Namba, S. Fujioka, H. Nishimura, Y. Yasuda, K. Nagai, N. Miyanaga, Y. Izawa, K. Mima, K. Takiyama, App. Phys. Lett. **88**, 171503, 2006.

[128] E. R. Kieft, K. Garloff, J. J. A. M. van der Mullen, V. Banine, Phys. Rev. E **71**, 036402, 2005.

[129] A. A. Andreev, T. Ueda, J. Limpouch, Emerging Lithographic Technologies V, Elisabeth A. Dobish, Editor, Proc. of SPIE Vol. **4343**, pg. 789, 2001.

[130] C. Rajyaguru, T. Higashiguchi, M. Koga, K. Kawasaki, M. Hamada, N. Dojyo, W. Sasaki, S. Kubodera, Appl. Phys. B **80**, 409, 2005.

[131] S. Düsterer, H. Schwoerer, W. Ziegler, C. Ziener, R. Sauerbrey, Appl. Phys. B **73**, 693, 2001.

[132] K. Fahy, P. Dunne, L. McKinney, G. O'Sullivan, E. Sokell, J. White, A. Aguilar, J. M. Pomeroy, J. N. Tan, B. Blagojevi, E. O. LeBigot, J. D. Gillaspy, J. Phys. D: Appl. Phys. **37**, 3225, 2004.

[133] W. Svendsen, G. O'Sullivan, Phys. Rev. A **50**, 3710, 1994.

[134] S. Churilov, Y. N. Joshi, J. Reader, Opt. Lett. **28**, 1478, 2003.

[135] N. Böwering, M. Martins, W. N. Partlo, I. V. Fomenkov, J. Appl. Phys. **95**, 16, 2004.

[136] H. Tanuma, H. Ohashi, S. Fujioka, H. Nishimura, A. Sasaki, K. Nishihara, J.l of Phys.: Conference Series **58**, 231, 2007.

[137] R. Karazija, S. Kucas, A. Momkauskait, J. Phys. D: Appl. Phys. **39**, 2973, 2006.

[138] J. White, A. P. Hayden, P. Dunne, A. Cummings, N. Murphy, P. Sheridan, G. O'Sullivan, J. Appl.Phys. **98**, 113301, 2005.

[139] S. S. Harilal, B. O'Shay, M. S. Tillack, Y. Tao, R. Paguio, A. Nikroo, C. A. Back, J. Phys. D: Appl. Phys. **39,** 484, 2006.

[140] S. S. Churilov, A. N. Ryabtsev, Optics and Spectroscopy **101,** 169, 2006.

[141] S. S. Churilov, A. N. Ryabtsev, Phys. Scr. **73**, 614, 2006.

[142] A. Sasaki, K. Nishihara, F. Koike, T. Kagawa, T. Nishikawa, K. Fujima, T. Kawamura, H. Furukawa, IEEE J. Sel. Top. Quantum Electron. **10**, 1307, 2004.

[143] G. O'Sullivan, P. K. Carroll, J. Opt. Soc. Am. **71**, 227, 1981.

[144] P. K. Carroll, G. O'Sullivan, Phys. Rev. A **25**, 275, 1982.

[145] J. Bauche, C. Bauche-Arnoult, M. Klapisch, Physica Scripta. **31***, 659, 1988.

[146] J. Bauche, C. Bauche-Arnoult, Phys. Scr. **T40**, 58, 1992.

[147] G. O'Sullivan, R. Faulkner, Opt. Eng. **33**, 3978, 1994.

[148] E. Kacar, A. Demir, G. J. Tallents, J. Plas. Phys. **72**, 6, 1263, 2006.

[149] R. W. P McWhirter, A. G. Hearn, Proc. Phys. Soc. Jpn. **82**, pg. 641, 1963.

[150] P. Demir, E. Kacar, E. Akman, S. K. Bilikmen, A. Demir, Ultrafast X-Ray Sources and Detectors, edited by Zenghu Chang, George A. Kyrala, Jean-Claude Kieffer,   Proc.   of   SPIE   Vol.   **6703**,   67030B,   2007.

CURRICULUM VITAE

Name, Surname: Pınar Demir
Nationality: T. C.
e-mail: pdemir@gmail.com

Education

Middle East Technical University, Ankara. Ph. D. Program in the Faculty of Arts and Science, Physics Department (2008).

Middle East Technical University, Ankara. "Informatics Online" M. S. Program in Informatics Institute (2007).

Middle East Technical University, Ankara. M. S. Program in the Faculty of Arts and Science, Physics Department.

Middle East Technical University, Ankara. B. S. Program in the Faculty of Arts and Science, Physics Department (1997).

Work Experience

January 2007 – July 2007. Worked as a TÜBITAK project personel in the Ministry of Defense (MSB) project with code 106A002 and name "Development of a Laser System", at the Middle East Technical University, Physics Department.

April 2006 – January 2007. Worked as a project personel in the State Planning Organization (DPT) project with code 2004K120710 and name "Development of X-ray Lasers for Industrial Applications", at the Middle East Technical University, Physics Department.

October 2003 – March 2006. Worked as a Research Assistant with Scholarship at the Başkent University, Faculty of Engineering.

Publications

"Theoretical and Experimental Investigation of Soft-X Rays Emitted from Tin Plasmas for Lithographic Application", **P. Demir**, E. Kaçar, E. Akman, S. Bilikmen, A. Demir, "Ultrafast X_Ray Sources and Detectors", Edited by Z. Chang, G. A. Kyrala, J. C. Kieffer, Proc. Of SPIE Vol. **6703**, 67030B1, 2007.

"Longitudinally Pumped Ne-like Titanium X-Ray Laser Simulation with a Post-Processor Code Coupled to EHYBRID", A. Demir, E. Akman, S. Bilikmen, **P. Demir**, S. İnce, E. Kaçar, E. Yurdanur, S. Yaltkaya, Springer , Proceedings of the 10th International Conference on X-Ray Lasers, Vol. **115**, pg. 341, 2006.

"Simulation of Longitudially Pumped Ni-like Molybdenium X-Ray Laser Medium Using Post-Processor Code Coupled to EHYBRID", E. Kaçar, P. Demir, **P. Demir**, A. Demir, S. Yaltkaya, , Proceedings of the 10th International Conference on X-Ray Lasers, Vol. **115**, pg. 347, 2006.